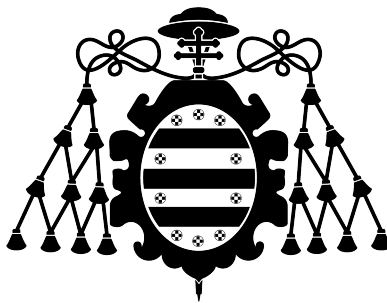# NANO-OPTICS WITH PHONON POLARITONS IN VAN DER WAALS MATERIALS

NANO ÓPTICA CON FONÓN-POLARITONES EN MATERIALES DE VAN DER WAALS

Universidad de Oviedo

Departamento de Física

Programa de Doctorado en Física de la Materia Condensada, Nanociencia y Biofísica

Javier Taboada Gutiérrez

Supervisores Doctorales:
Thesis Advisors:
Pablo Alonso González
Javier Martín Sánchez

Universidad de Oviedo

RESUMEN DEL CONTENIDO DE TESIS DOCTORAL

1.- Título de la Tesis	
Español/Otro Idioma: Nano Óptica con Fonón-Polaritones en materiales de van der Waals	Inglés: Nano-Optics with Phonon Polaritons in van der Waals Materials

2.- Autor	
Nombre: Javier Taboada Gutiérrez	DNI/Pasaporte/NII
Programa de Doctorado: Programa de Doctorado en Física de la Materia Condensada, Nanociencia y Biofísica	
Órgano responsable: Universidad de Oviedo	

RESUMEN (en español)

Debido al límite de difracción de la luz, el potencial de l nanociencia y nanotecnología no puede ser explotado con luz ordinaria. Sin embargo, la excitación de polaritones (nanoluz) en la intercara entre un metal y un aislante provee una forma de concentrar la luz (reducir su longitud de onda) sin aumentar su frecuencia (su energía). Recientemente, se ha descubierto que los materiales laminares (materiales de van der Waals, vdW) poseen la mayor capacidad, de entre todos los materiales conocidos, de confinar la luz en la nanoescala. Sin embargo, la dispersión de polaritones en el plano de estos materiales es isótropa, lo que conlleva dificultades a la hora de controlar su propagación. Además, los polaritones excitados en materiales polares presentan la desventaja de poder ser únicamente excitados en bandas estrechas de frecuencias (conocidas como *Reststrahlen Bands*, RB) en el espectro infrarrojo.

En esta tesis, se introduce por primera vez la propagación anisótropa en el plano de nanoluz en materiales polares en la fase alfa del trióxido de molibdeno. El caso más extremo se conoce como propagación hiperbólica, donde los polaritones puedes propagar solo a lo largo de unas determinadas direcciones del plano, lo que nos brinda unas oportunidades sin precedentes para la focalización de la luz en la nanoescala. Además, se desarrolla un modelo teórico para explicar su comportamiento, así como unos dispositivos 'prueba de concepto' para explotar dichas capacidades. Por otro lado, el problema de la excitación de nanoluz en las RB es abordado mediante la intercalación de átomos alcalinos en la estructura cristalina del pentaóxido de vanadio, consiguiendo desplazamientos de las RB de más de 100cm^{-1}. Asimismo, se encuentra que los tiempos de vida de los polaritones en estos materiales marcan récords, alcanzando los 8ps. Finalmente, se estudia desde un punto de vista fundamental el origen físico de los mecanismos de pérdidas que limitan la propagación de polaritones en trióxido de molibdeno y que, por tanto, nos impiden explotar el máximo rendimiento polaritónico que se podría dar a dispositivos basados en esta tecnología.

RESUMEN (en Inglés)

Due to the diffraction limit of light, the potential of nanoscience and nanotechnology cannot be exploited with ordinary light. However, the excitation of polaritons (nanolight) at the interface between a metal and an insulator provides a way to concentrate light (reduce its wavelength) without increasing its frequency (its energy). Recently, lamellar materials (known as van der Waals materials, vdW) have been found to possess the greatest ability, among all known materials, to confine light at the nanoscale. However, the in-plane dispersion of polaritons in these materials is isotropic, which leads to difficulties in controlling their propagation. In addition, polaritons excited in polar materials have the disadvantage of being able to be excited only in narrow frequency bands (known as *Reststrahlen Bands*, RB) in the infrared spectrum.

In this thesis, in-plane anisotropic propagation of nanolight in polar materials is

introduced for the first time in the alpha phase of molybdenum trioxide. The most extreme case is known as hyperbolic propagation, where polaritons can propagate only along certain directions of the plane, which gives us unprecedented opportunities for nanoscale light focusing. In addition, a theoretical model is developed to explain their behavior, as well as 'proof-of-concept' devices to exploit these capabilities. On the other hand, the problem of excitation of nanolight in RBs is addressed by intercalating alkali atoms in the crystal structure of vanadium pentaoxide, achieving RB shifts of more than $100 cm^{-1}$. Likewise, it is found that the polariton lifetimes in these materials set records, reaching 8ps. Finally, we study from a fundamental point of view the physical origin of the loss mechanisms that limit the propagation of polaritons in molybdenum trioxide and, therefore, prevent us from exploiting the maximum polariton performance that could be given to devices based on this technology.

SR. PRESIDENTE DE LA COMISIÓN ACADÉMICA DEL PROGRAMA DE DOCTORADO
EN Física de la Materia Condensada, Nanociencia y Biofísica

Resumen

Debido al límite de difracción de la luz, el potencial de la nanociencia y la nanotecnología no puede ser explotado con luz ordinaria. Sin embargo, la excitación de polaritones en la intercara entre un metal y un aislante provee una forma de concentrar la luz (reducir su longitud de onda) sin aumentar su frecuencia (su energía). Recientemente, se ha descubierto que los materiales laminares (materiales de van der Waals, vdW) poseen la mayor capacidad, de entre todos los materiales conocidos, de confinar la luz en la nanoescala. Sin embargo, la dispersión de polaritones en el plano de estos materiales es isótropa, lo que conlleva dificultades a la hora de controlar su propagación y desarrollar aplicaciones. Además, los polaritones excitados en materiales polares (conocidos como fonón-polaritones) presentan la desventaja de poder ser excitados únicamente en bandas estrechas de frecuencias (conocidas como *Reststrahlen Bands*, RB) en el espectro infrarrojo.

En esta tesis, se introduce por primera vez la propagación anisótropa en el plano de polaritones en materiales polares en la fase alfa del trióxido de molibdeno. El caso más extremo se conoce como propagación hiperbólica, donde los polaritones pueden propagar solo a lo largo de unas determinadas direcciones del plano, lo que nos brinda unas oportunidades sin precedentes para la focalización de la luz en la nanoescala. Además, se desarrolla un modelo teórico para explicar su comportamiento, así como unos dispositivos 'prueba de concepto' para explotar dichas capacidades. Por otro lado, el problema de la excitación de los fonón-polaritones en las RB es abordado mediante la intercalación de átomos alcalinos en la estructura cristalina del pentaóxido de vanadio, consiguiendo desplazamientos de las RB de más de $100 cm^{-1}$. Asimismo, se encuentra que los tiempos de vida de los polaritones en estos materiales marcan récords, alcanzando los $8\,ps$ y que el intercalado no afecta a los mismos. Finalmente, se estudia desde un punto de vista fundamental el origen físico de los mecanismos de pérdidas que limitan la propagación de polaritones en trióxido de molibdeno y que, por tanto, nos impiden explotar el máximo rendimiento polaritónico que se podría dar a dispositivos basados en esta tecnología.

Summary

Due to the diffraction limit of light, the potential of nanoscience and nanotechnology cannot be exploited with ordinary light. However, the excitation of polaritons at the interface between a metal and an insulator provides a way to concentrate light (reduce its wavelength) without increasing its frequency (its energy). Recently, it has been found that lamellar materials (van der Waals materials, vdW) possess the greatest ability, among all known materials, to confine light at the nanoscale. However, the in-plane dispersion of polaritons in these materials is isotropic, which leads to difficulties in controlling their propagation and developing applications. Furthermore, polaritons excited in polar materials (known as phonon-polaritons) have the disadvantage of being able to be excited only in narrow frequency bands (known as *Reststrahlen Bands*, RB) in the infrared spectrum.

In this thesis, in-plane anisotropic propagation of polaritons in polar materials is introduced for the first time in the alpha phase of molybdenum trioxide. The most extreme case is known as hyperbolic propagation, where polaritons can propagate only along certain in-plane directions, giving us unprecedented opportunities for nanoscale light focusing. In addition, a theoretical model is developed to explain their behavior, as well as 'proof-of-concept' devices to exploit these capabilities. On the other hand, the problem of phonon-polariton excitation in RBs is addressed by intercalating alkali atoms in the crystal structure of vanadium pentaoxide, achieving RB shifts of more than $100\,cm^{-1}$. It is also found that the lifetimes of polaritons in these materials set records, reaching $8\,ps$ and that the intercalation does not affect them. Finally, we study from a fundamental point of view the physical origin of the loss mechanisms that limit the propagation of polaritons in molybdenum trioxide and, therefore, prevent us from exploiting the maximum polariton performance that could be given to devices based on this technology.

Agradecimientos

Afortunadamente, a lo largo de mi vida he conocido a mucha gente maravillosa con la que he vivido muy buenos momentos y me ha ayudado a llegar hasta aquí.

Para empezar, me gustaría mencionar especialmente a mis directores de tesis, el Dr. Pablo Alonso González y el Dr. Javier Martín Sánchez, por dar todo de sí para ayudarme a llegar aquí y por la emoción e ilusión que transmitían cuando se discutía sobre la física de nuestros experimentos en aquellas reuniones que duraban toda una tarde antes de que llegase el Covid. Gracias.

A los postdoc del grupo de Nanoóptica. Al Dr. Duan Jiahua por su incansable capacidad de trabajo y por las absurdas e hilarantes aventuras que vive y a la Dra. Aitana Tarazaga Martín-Luengo por su disposición a solucionarle la vida a Duan.

A todos mis compañeros doctorandos del grupo de Nanoóptica: Gonzalo, Ana, Abel, Christian y Adam, por esos maravillosos momentos, apoyo y ánimos. PIMBA!

A los alumnos de TFG que fueron pasando por el laboratorio, en especial a Jorge y a Patricia, que siempre estaban dispuestos a trabajar pasándolo bien.

A la gente de nanoGUNE que tan bien acogió todas las veces que fui de estancia, en especial, a Irene, Marta, Javi y Andrei. Por las aventuras en Benasque.

A la gente que vino de estancia durante este tiempo, en concreto, al Dr. Pablo Díaz Núñez que aprendimos juntos a manejar el sistema experimental cuando comenzaba mi tesis.

Al Prof. Alexey Kuzmenko, a la Dr. Yixi Zhou y a Adrien Bercher por el buen recibimiento, el apoyo y la ilusión que transmitían cuando los equipos científicos querían funcionar durante mi estancia en Ginebra.

Al Prof. José Ignacio Martín Carbajo y a la Prof. María Vélez Fraga por su lucidez y por esas capacidades inhumanas de sacar las cosas adelante y avanzar.

A la gente de los Servicios Científico-Técnicos de la Universidad de Oviedo, en concreto, a Bea y a Jorge por ayudarme en el laboratorio en cualquier momento y su total disponibilidad para colaborar.

Al resto de miembros del Área de Física de la Materia Condensada de la Universidad de Oviedo, en especial, al Prof. Luis Manuel Álvarez Prado, el Prof. Víctor Manuel García Suárez y el Dr. Aurelio Hierro Rodríguez.

A todos mis amigos con los que comparto tantos buenos momentos por Luanco y San Jorge.

A toda mi familia, a los que están y a los que ya se fueron. A mis padres y mi hermana, a mis tíos, a mis abuelos, a mi madrina y demás, por apoyarme incondicionalmente en todo momento.

List of Publications

The following list summarizes all the scientific publications that have been made during the completion of this thesis (2017-2022) in chronological order regardless of whether they have been incorporated into the text or not.

1. 'In-plane anisotropic and ultra-low-loss polaritons in a natural van der Waals crystal'
   Ma *et al.*, Nature 562, 557–562 (2018)
   DOI: 10.1038/s41586-018-0618-9

2. 'Strain-Tunable Single Photon Sources in WSe_2 Monolayers'
   Iff *et al.*, Nano Letters 19, 10, 6931–6936 (2019)
   DOI: 10.1021/acs.nanolett.9b02221

3. 'On the Large Near-Field Enhancement on Nanocolumnar Gold Substrates'
   Díaz-Núñez *et al.* Scientific Reports 9, 13933 (2019)
   DOI: 10.1038/s41598-019-50392-w

4. 'Infrared Permittivity of the Biaxial van der Waals Semiconductor α-MoO_3 from Near- and Far-Field Correlative Studies'
   Álvarez-Pérez *et al.*, Advanced Materials 32, 29, 1908176 (2020)
   DOI: 10.1002/adma.201908176

5. 'Broad spectral tuning of ultra-low-loss polaritons in a van der Waals crystal by intercalation'
   Taboada-Gutiérrez *et al.*, Nature Materials 19, 964–968 (2020)
   DOI: 10.1038/s41563-020-0665-0

6. 'Twisted Nano-Optics: Manipulating Light at the Nanoscale with Twisted Phonon Polaritonic Slabs'
   Duan *et al.*, Nano Letters 20, 7, 5323–5329 (2020)
   DOI: 10.1021/acs.nanolett.0c01673

7. 'Nanoscale-Confined Terahertz Polaritons in a van der Waals Crystal'
   de Oliveira *et al.*, Advanced Materials 33, 2, 2005777 (2021)
   DOI: 10.1002/adma.202005777

8. 'Extracting the Infrared Permittivity of SiO_2 Substrates Locally by Near-Field Imaging of Phonon Polaritons in a van der Waals Crystal'
   Aguilar-Merino *et al.*, Nanomaterials 11(1), 120 (2021)
   DOI: 10.3390/nano11010120

9. 'Real-space observation of vibrational strong coupling between propagating phonon polaritons and organic molecules'
   Bylinkin *et al.*, Nature Photonics 15, 197–202 (2021)
   DOI: 10.1038/s41566-020-00725-3

10. 'Enabling propagation of anisotropic polaritons along forbidden directions via a topological transition'
    Duan *et at.*, Science Advances 7, 14 (2021)
    DOI: 10.1126/sciadv.abf2690

11. 'Planar refraction and lensing of highly confined polaritons in anisotropic media'
    Duan *et al.*, Nature Communications 12, 4325 (2021)
    DOI: 10.1038/s41467-021-24599-3

12. 'Focusing of in-plane hyperbolic polaritons in van der Waals crystals with tailored infrared nanoantennas'
    Martín-Sánchez *et al.*, Science Advances 7, 41 (2021)
    DOI: 10.1126/sciadv.abj0127

13. 'Active and Passive Tuning of Ultranarrow Resonances in Polaritonic Nanoantennas'
    Duan *et al.*, Advanced Materials 34, 10, 2104954 (2022)
    DOI: 10.1002/adma.202104954

Contents

List of Figures

IX

List of Tables

Introduction and State of the Art

In this thesis, the study of the propagation of light at nanoscale will be studied in Van der Waals nanomaterials presenting high in-plane structural anisotropy, i.e., anisotropic propagation of 'nanlight' or polaritons. Particularly, in this chapter, we will give an introduction to the field of polaritonics, as well as a definition of polaritons as a way to beat the diffraction limit and confine light at the nanoscale. A brief preface to the physics of polaritons is provided for two different kinds of polaritons: plasmon polaritons and phonon polaritons. Van der Waals materials are introduced as one of the best platforms to support ultra-confined light at the nanoscale. The fundamental differences between polaritons in van der Waals materials and polaritons in bulk materials are highlighted. Hyperbolicity is introduced as an extreme type of anisotropic propagation of polaritons and the opportunities of hyperbolic polaritons are summarized. The scattering-type scanning near-field optical microscopy technique is shortly introduced as a nanophotonic tool for visualizing the flow of light at the nanoscale. Finally, the scope and organization of the thesis is given in the last section.

1.1 | Nanooptics

Understanding light-matter interactions has brought society to develop more in the last 100 years than in the rest of its existence. Quantum mechanics was born thanks to the study of atomic line spectra in selected materials when illuminated with light of a certain frequency [1]. We can either use matter to control light, for example, laser emission can be controlled through modifications of the gain medium and the pump source [2, 3], or we can use light to control matter, for example, manipulating molecules and cells by means of a laser beam in optical tweezers [4]. However, coupling light and matter at particular frequencies faces a fundamental problem: the diffraction limit of light, which states that the smallest resolvable distance between two objects cannot be smaller than half of the wavelength of the imaging light [5]. As such, the diffraction limit establishes a restriction over how much an electromagnetic wave can be shrinked to control and explore new optical phenomena. This has important consequences for instance in the mid infrared spectral region, where technologically important organic materials or biological substances have unique absorption spectra [6] but their sizes are much smaller (less than $1\,\mu m$) than the wavelength of light (MIR, from $\lambda_0 = 2.5\,\mu m$ to $\lambda_0 = 25\,\mu m$ with λ_0 representing the wavelength of light). Additionally, near-field thermal emission of warm micro- and nano-objects

(temperatures higher than $300K$) correspond to wavelengths within the MIR and their control and management is critical for industrial purposes. Therefore, the potential of nanoscience and nanotechnology cannot be fully exploited with ordinary light.

Polaritons provide a way to overcome this problem and bring light to much smaller volumes [7]. They are hybrid light-matter electromagnetic waves that arise from the coupling of photons with dipolar excitations in matter (i.e., the electron cloud in metals, optical phonons in polar materials, or electron-hole pairs in semiconductors, see **Figure 1.1**) with the same frequency (energy) than light with which they are excited [8, 9]. Due to their confinement capability, polaritons hold promises for applications at the nanoscale such as biosensing [6, 10], nanochemistry [11], photocatalysis [12], near-field thermal management [13, 14] or nanolight trafficking [15], among others. Nevertheless, due to the reduced polaritonic wavelength, λ_p, with respect to the wavelength of excitation light, λ_0, a momentum mismatch $\Delta k = k_p - k_0$ must be overcome in order to excite them, with $k_p = 2\pi/\lambda_p$ the polariton momentum and $k_0 = 2\pi/\lambda_0$ the momentum of the excitation light.
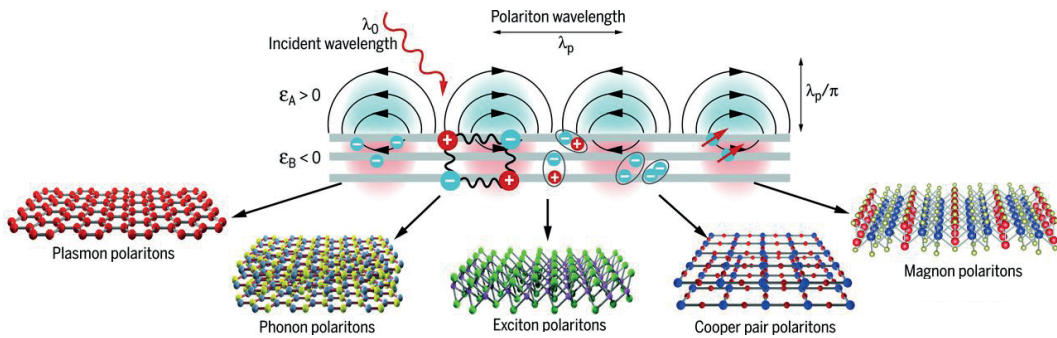
Figure 1.1: Polaritons Polaritons are hybrid light-matter excitations involving different dipolar phenomena: conduction electrons in metals (plasmon polaritons), optical phonons in polar materials (phonon polaritons), excitons in semiconductors (exciton polaritons), cooper pairs in superconductors (cooper pair polaritons) and magnetic resonances in magnetic materials (magnon polaritons). Illustration adapted from [8].

Surface Plasmon Polaritons

Among all types of polaritons [8, 16], surface plasmon polaritons (SPPs, **Figure 1.2A**) are by far the most studied [9, 17, 18]. They arise from the interaction between light and the collective oscillations of the electron cloud in metals or highly doped semiconductors and can be described in terms of their complex permittivity or dielectric constant, ε. In particular, noble metals (Au, Ag, Pt, etc.) possess two main contributions to the permittivity at visible and infrared frequencies: one related to the free conduction electron cloud (or Drude contribution) and the other to the interband excitations, which take place at approximately $2.5\,eV$ and higher energies. For the sake of simplicity, we will only consider here the contribution of the free electrons. Consequently, the permittivity of noble metals can be modelled as (See **Figure 1.2B**) [19]:

$$\varepsilon_m(\omega_0) = 1 - \frac{\omega_p^2}{\omega_0^2 + i\gamma\omega} \tag{1.1}$$

where γ denotes the damping term (which takes into consideration phenomena such as electron-electron scattering, or electron-phonon scattering, among others) and ω_p is the plasma frequency, that is, the frequency below which electrons are moving in the opposite direction to the electric field preventing the field to penetrate into the metal, what corresponds to a negative permittivity. Above the plasma frequency, electrons in metals cannot vibrate at the same rate as the incident electromagnetic field and the wave penetrates the metal, what corresponds to a positive permittivity. Solving the Maxwell's equations at the interface between a metal and a dielectric material (supposing the interface placed at the plane $z = 0$), we found that SPPs are transversal magnetic (TM) polarized waves propagating along the interface of the dielectric and the metal with the following dispersion relation, $k_{SPP}^x(\omega_0)$, (See **Figure 1.2C**) [20]:

$$k_{SPP}^x(\omega_0) = k_0(\omega_0)\sqrt{\frac{\varepsilon_d \varepsilon_m}{\varepsilon_d + \varepsilon_m}} = \frac{\omega_0}{c}\sqrt{\frac{\varepsilon_d \varepsilon_m}{\varepsilon_d + \varepsilon_m}} \tag{1.2}$$

where ε_d and ε_m represent the permittivities of the dielectric and metal media, respectively. Also, an expression for the normal component of the wavevector can be obtained in the metal (m) and dielectric (d):

$$k_{SPP}^{j,z}(\omega_0) = k_0(\omega_0)\frac{\varepsilon_j}{\sqrt{\varepsilon_m + \varepsilon_d}}; j = m, d \tag{1.3}$$

Propagating solutions along the metal-dielectric interface require a real k_{SPP}^x. This could be fulfilled if the terms $\varepsilon_d \varepsilon_m$ and $\varepsilon_d + \varepsilon_m$ are both positive or both negative. Besides, to obtain a solution bounded to the interface, purely imaginary 'z' components of the wavevector are required in both media. Consequently, the term $\varepsilon_m + \varepsilon_d$ must be negative and, therefore, to guarantee the excitation of SPPs, the metal and dielectric materials must fulfill the conditions [19]:

$$\varepsilon_d(\omega_0) \cdot \varepsilon_m(\omega_0) < 0$$
$$\varepsilon_d(\omega_0) + \varepsilon_m(\omega_0) < 0 \tag{1.4}$$

Hence, SPPs can only be excited at the interface between two materials as long as: i) they present different sign in their dielectric function (i.e., a metal and a dielectric) and ii) the absolute value of the metal's permittivity exceeds that of the dielectric, which is the case for a metal/air interface in the visible (VIS) and MIR regimes. Note that, since the factor $\sqrt{(\varepsilon_d \varepsilon_m)/(\varepsilon_d + \varepsilon_m)}$ is larger than 1, SPPs are confined waves, $k_{SPP}(\omega_0) > k_0(\omega_0)$, as mentioned above.

The real part of the SPPs wavevector accounts for the SPP wavelength, whereas the imaginary part represents its damping. Accordingly, the SPP wavelength is given by:

$$\lambda_{SPP}^x = \frac{2\pi}{\mathfrak{Re}(k_{SPP}^x)} = \frac{2\pi}{k_0(\omega_0)}\mathfrak{Re}\left(\sqrt{\frac{\varepsilon_d + \varepsilon_m}{\varepsilon_d \cdot \varepsilon_m}}\right) = \lambda_0 \mathfrak{Re}\left(\sqrt{\frac{\varepsilon_d + \varepsilon_m}{\varepsilon_d \cdot \varepsilon_m}}\right) \tag{1.5}$$

The SPP propagation length along the interface, L_p, is defined as the distance at which the SPP electric field decreases by a factor $1/e$. Since the SPP electric field is supposed to be given by a plane wave [19]:

$$|\vec{E}| \propto \exp(ik_{SPP}^x x) = \exp(i\mathfrak{Re}(k_{SPP}^x)x)\exp(-\mathfrak{Im}(k_{SPP}^x)x), \tag{1.6}$$
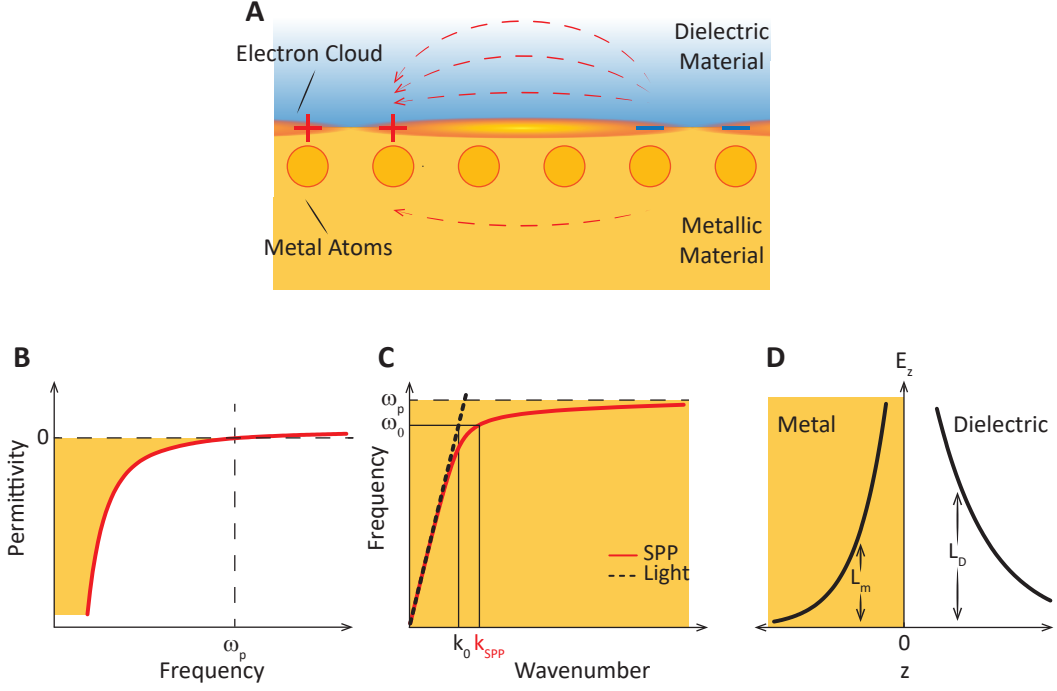
Figure 1.2: Properties of Surface Plasmon Polaritons **A** Oscillating electron clouds in metals. Yellow spheres denote the atoms in the metal lattice while the blurred yellow area denote the electron cloud. '+' and '−' symbols are added together with red dashed arrows to illustrate the electric field. The dielectric material is represented by the blue region whereas the metallic material is represented by the yellow region **B** Permittivity function of a metal. ω_p represents the plasma frequency, where the metal permittivity changes from negative to positive values and ceasing the reflection of the impinging electromagnetic field. **C** The dispersion of SPPs (red curve) is shown together with the light's dispersion (black dashed curve) for comparison. At a given frequency, ω_0, the polaritons wavevector has an absolute value, k_{SPP}^x, larger than the light wavevector, k_0. **D** SPP confinement at the interface between a metal and a dielectric. The SPP electric field decreases faster in the metal (smaller normal decay length L_m) than in the dielectric (higher normal decay length L_d). The yellow shadowed regions in **B**, **C** and **D** represent the frequency range where the metal's permittivity presents negative values.

the SPP propagation length along the interface will be given by $L_p^x = 1/\mathfrak{Im}(k_{SPP}^x)$. In the same way, the SPP decay length into the dielectric and the metal is defined as the distance at which the SPP electric field decreases by a factor $1/e$ along the direction perpendicular to the interface. Consequently, $L_p^{j,z} = 1/\mathfrak{Im}(k_{SPP}^{j,z})$ with j either the metal or the dielectric (**Figure 1.2D**). It can also be shown [21], that the SPP is associated with an enhancement of the electric field intensity, which has been widely investigated as a means for increasing the Raman scattering signal of inorganic and organic materials, leading to the development of the so-called surface-enhanced Raman scattering (SERS) [22, 23]. Exploiting the field enhancement of SPP materials, enhancement factors higher than 10^7 for the Raman signal have been reported [19].

Surface Phonon Polaritons

Apart from SPPs, another interesting type of polaritons are surface phonon polaritons (SPhPs) [24, 25]. These confined waves are hybrid electromagnetic waves resulting from the coupling of photons with optical phonons in polar materials, that is, bound charges oscillating coherently in the crystal lattice [26]. The spectral range where SPhPs can be excited is directly related to the spectral range where the polar material presents a negative permittivity. This happens in the so-called *Reststrahlen Band* (RB), which is a narrow frequency band defined between the transverse optical phonon (TO) and the longitudinal optical phonon (LO) where the bound changes oscillate in such a way that they reflect the incident radiation (**Figure 1.3A**) [24]. RBs are typically found at MIR and terahertz (THz) frequencies. Remarkably, as SPhPs arise from the coupling to phonons, they do not suffer from the common electron-electron scattering processes (typically known as ohmic losses) present in metals (and consequently in SPPs), resulting in long SPhPs lifetimes of the order of picoseconds (note that SPPs lifetimes are on the order of femtoseconds [27]). The physics behind the excitation of SPhPs is mainly the same as for SPPs, so all the equations and results presented in Section 1.1.1 apply also for SPhPs. However, the permittivity of a polar material, ε_p, is differently modelled theoretically by employing Lorentz oscillators (**Figure 1.3B**):

$$\varepsilon_p(\omega) = \varepsilon_\infty + \sum_j \frac{\omega_{LO,j}^2 - \omega^2 - i\omega\gamma_{LO,j}}{\omega_{TO,j}^2 - \omega^2 - i\omega\gamma_{TO,j}} \tag{1.7}$$

where ε_∞ is the high-frequency dielectric constant, ω_{TO} and ω_{LO} are the TO and LO frequency positions, respectively, γ_{TO} and γ_{LO} represent the TO and LO damping factors and j an index that describes the number of TO-LO pairs present in the polar material.
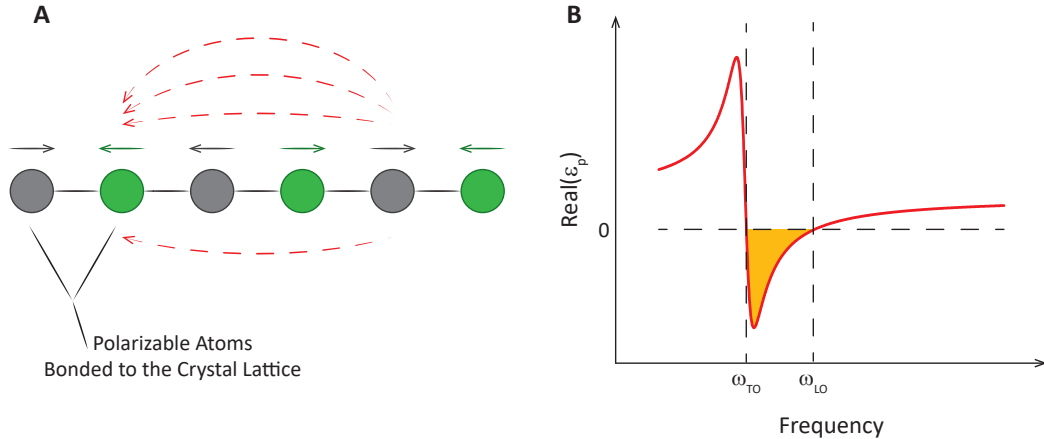
Figure 1.3: Properties of Surface Phonon Polaritons A Oscillating lattice-bounded charges in polar materials. Atoms are depicted as green and grey circles and their respective movements as green and grey arrows. Red dashed lines illustrate the electric field. **B** Permittivity of polar materials at infrared frequencies showing a *Reststrahlen Band* (yellow shadowed region) between the TO and LO phonon frequencies where the dielectric constant reaches negative values.

To better analyze the differences between SPhPs and SPPs it is useful to compare some of their properties. It can be shown [28] that for phononic and plasmonic

nanospheres of the same radius, the electric field enhancement associated with SPhPs can be up to 3 times higher than that of SPPs (both with respect to the excitation electric field). Moreover, the quality factor, Q, of the phonon-polaritonic resonance, defined as the ratio between the peak position of the resonance and its full-width at half-maximum (FWHM), can be also larger by a factor up to 7.5 compared to that of SPPs. A complete comparison between the field enhancement provided by a phonon-polaritonic material, for example silicon carbide, SiC, and a plasmon-polaritonic material, for example gold, Au, inside and outside the SiC RB can be found in [29].

1.2 | Van der Waals Crystals. Novel Polaritons with unprecedented properties in the Mid-Infrared spectral range

With the advent of 2D materials after the isolation of graphene (an atomically thick sheet of carbon atoms covalently bonded in a honeycomb lattice by hybrid sp^2 orbitals (Figure 1.4A) in 2004 [30], countless attention has been given to the van der Waals materials family, which covers all the known substances composed of either mono- or multi-atomic planes held together by van der Waals forces, regardless of their physical behaviour (metals, insulators, semiconductors, magnetic materials, etc.). Due to their unprecedented optoelectronic properties, new fundamental physics [31, 32, 33] and applications [34, 35] have been rapidly explored in vdW materials, including graphene, transition metal dichalcogenides (TMDs, i.e., WSe_2, WS_2, $MoSe_2$, MoS_2) [36] and hexagonal boron nitride (h-BN) [37]. Importantly, these properties also include the excitation of surface polaritons, as recently reported [38, 39, 40, 41, 42, 43, 44]. In particular, due to the inherent anisotropy of a layered system, in-plane and out-of-plane opposite-sign permittivities can be found in vdW materials at certain frequency ranges of the electromagnetic spectrum [8, 7]. This unique behavior makes them suitable material platforms in order to support polaritonic waveguides with the highest degree of confinement. In fact, polariton wavelengths deep below the excitation wavelength exhibiting confinement factors $\lambda_0/\lambda_p > 70$ have been reported [45, 46], demonstrating van der Waals materials as ideal hosts for trapping light at the nanoscale. Moreover, it has been reported that polaritons in van der Waals materials can be straightforwardly controlled via either external stimuli [38, 39, 44], passive tuning of the material thickness [40, 41, 42], or surface nanopatterning [47].

In addition, exfoliating and preparing van der Waals materials samples is an easy task that can be carried out in almost any laboratory. The only technical requirements are a suitable tape, a bulk crystal of the van der Waals material to be studied and an optical microscope [30]. Thinning down the material by folding and unfolding the bulk crystal on the tape allows to exfoliate van der Waals flakes with a desired thickness. Indeed, due to the layered nature of the materials, fully flat samples are readily obtained. Artificial structures assembled from a variety of van der Waals materials known as 'van der Waals heterostructures' [48] can also be easily fabricated by means of the so-called dry transfer technique [49, 50], leading to systems with intertwined properties. This is a key aspect of van der Waals materials, as fabrication of dissimilar structures of common bulk materials usually rely on expensive and time-consuming epitaxial growth techniques. Hence, van der Waals crystals provide powerful building-blocks for polariton research. Further details of

the exfoliation procedure and the dry-transfer method will be given in Section 2.1.

Interestingly, new polaritonic effects have been visualized in stacks of vdW materials, such as hybrid plasmon-phonon polaritons [51, 52] with electrical gating and thickness control without detriment of their lifetime, plasmon polariton photonic crystals and superlattices [53, 54], or diffraction-less polaritonic canalization [55, 56, 57, 58, 59]. For the sake of clarity, the following subsections introduce the main features of plasmon and phonon polaritons in van der Waals materials, highlighting the main differences with respect to the previously introduced SPPs and SPhPs in bulk materials such as Au and SiC, respectively.

Surface Plasmon Polaritons in Graphene

Due to the exotic linear electronic band structure with zero band gap of graphene at the **K** and **K'** points of the Brillouin zone (**Figure 1.4B**) [60], plasmonic modes in graphene were widely studied theoretically [61, 62, 63] before their first visualizations (**Figure 1.4C**) [38, 39, 64]. Modelling of the graphene optical conductivity typically includes two main electronic contributions: one describing electronic intraband transitions (transitions occurring inside the conduction band) and another describing electronic interband transitions (transitions from the valence band to the conduction band). In the spectral region where we are interested, i.e., MIR and THz frequencies, the intraband transition contribution vanishes, and the optical conductivity is dominated by the interband transitions:

$$\sigma_G(\omega_0) \approx \frac{\sigma_0}{\pi\hbar} \frac{4E_F}{\gamma - i\omega_0} \tag{1.8}$$

where $\sigma_0 = \pi e^2/2h$, with e the electron elementary charge and h the Planck's constant, $\hbar$ is the reduced Planck's constant, and E_F is the Fermi energy. By solving the Maxwell equations in a system considering a 2D graphene sheet with conductivity σ embedded between two different dielectrics, ε_1 and ε_2, one can easily derive the isotropic dispersion relation for graphene plasmons (**Figure 1.4D**) (supposing the nonretarded regime, i.e, the momentum of graphene plasmon polariton, k_G, is much higher than the momentum of light, $k_G \gg \omega_0/c$, which is indeed the case)[62, 65]:

$$k_G(\omega_0) = \frac{\pi\hbar\varepsilon_0}{e^2 E_F}(\varepsilon_1 + \varepsilon_2)\left(1 + \frac{i}{\gamma\omega_0}\right)\omega_0^2 \tag{1.9}$$

with ε_0 the permittivity of free space. As a difference to SPPs in noble metals, there is a square root dependence of the SPP frequency with the wavevector, $\omega_0 \propto \sqrt{k_G}$ (note that propagating solutions are related to $\mathfrak{Re}(k_G)$). The relation between the excitation wavelength and the polariton wavelength, i.e., the polaritonic compression factor [60] can be found as:

$$\frac{\lambda_G}{\lambda_0} = \frac{4\alpha}{\varepsilon_1 + \varepsilon_2}\frac{E_F}{\hbar\omega} \tag{1.10}$$

where $\alpha = e^2/(4\pi\varepsilon_0\hbar c) \approx 1/137$ is the fine-structure constant. Since $E_F \propto \sqrt{n}$, being n the carrier density [32], the graphene confinement factor can be tuned through both varying the excitation wavelength and/or the electronic carrier concentration, i.e., applying a voltage to the graphene flake [60]. As an example, at $\lambda_0 = 8\,\mu m$ and $E_F = 0.64\,eV$ (corresponding to reasonable real values), we obtain a graphene SPP wavelength of $190\,nm$, that is 42 times shorter than the incident

wavelength [62].
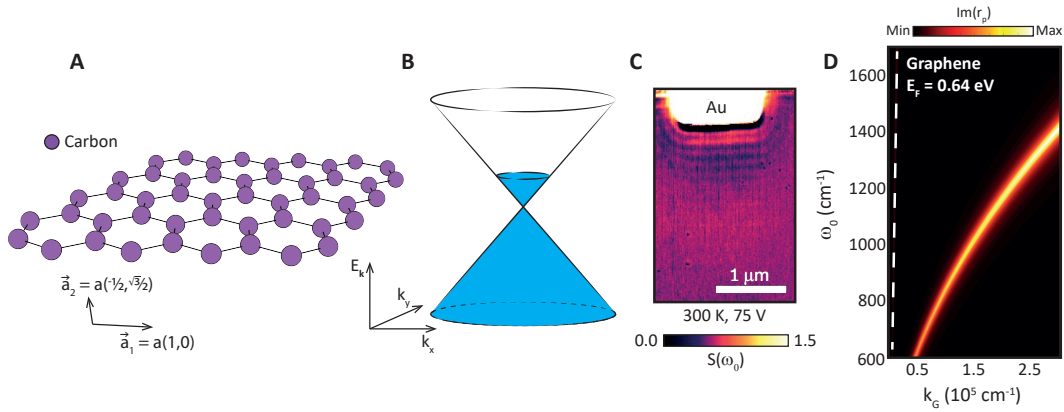
Figure 1.4: Plasmon Polaritons in Graphene A Graphene crystalline structure showing the characteristic honeycomb lattice and cell parameter $a = 1.42\sqrt{3}$Å. Violet circles denote carbon atoms. **B** Electronic band structure of graphene at the proximities of the high-symmetry points **K** and **K'**. The valence and the conduction band touch at one point known as Dirac point. **C** Propagating SPPs in graphene launched by a gold antenna taken at a temperature of 300K and a gating voltage of $75\,V$. Bright fringes represent the polaritonic oscillations. Image taken from [64]. **D** Graphene SPP dispersion calculated for a Fermi energy of $0.64\,eV$ (the graphene layer is supposed to be freestanding). The dispersion is visualized using a false color-plot of the imaginary part of the Fresnel reflection coefficient, r_p, for p-polarized waves. White dashed lines represent the dispersion of free-space light in order to highlight the momentum mismatch with SPPs in graphene.

These theoretical predictions for graphene SPPs were experimentally visualized in 2012 by two independent groups [38, 39] employing a scatterring-type near-field optical microscope (s-SNOM). Due to the ultra-high confinement of graphene SPPs, controlling them at the nanoscale become soon a scientific hot topic where the s-SNOM played a key role in both their excitation and visualization. Indeed, focusing and lensing capabilities were experimentally demonstrated through the use of Au nanoantennas [66], and photonic Moiré crystals composed of two rotated sheets of graphene were introduced to control their optical phenomena through local changes in the electronic band structure [54].

Phonon Polaritons in hexagonal Boron Nitride

Hexagonal boron nitride is a polar uniaxial vdW material with a crystalline structure similar to that of graphene (**Figure 1.5A**). Formerly, it was used as a substrate for improving some graphene properties such as the electron mobility [37, 67]. Due to its intrinsic anisotropy, h-BN possesses two optical phonons at MIR frequencies, which give rise to two not overlapping RB at MIR frequencies [40, 68] where PhPs exist. The first of these optical phonons represent an in-plane movement of the nitrogen and boron atoms in opposite directions, yielding the so-called upper RB ($\mathfrak{Re}(\varepsilon_x) = \mathfrak{Re}(\varepsilon_y) \equiv \mathfrak{Re}(\varepsilon_t) < 0$; $\mathfrak{Re}(\varepsilon_z) > 0$) between 1370 and $1610\,cm^{-1}$ (7.32 to 6.21 μm). The second optical phonon corresponds to an out-of-plane movement of the nitrogen and boron atoms in opposite directions, yielding the so-called lower RB ($\mathfrak{Re}(\varepsilon_z) < 0$; $\mathfrak{Re}(\varepsilon_t) > 0$) between 760 and $820\,cm^{-1}$ (12.77 and 12.08 μm) (see

Figure 1.5B).

h-BN is an insulator with an indirect bandgap of $5.9\,eV$ [69] in contrast to graphene, so, PhPs in h-BN cannot be controlled in situ by simply applying a voltage to the layers. However, the dispersion of the polaritonic modes propagating along an h-BN slab depend on its thickness, d, as demonstrated by Dai et al. [40]:

$$k_p(\omega_0) = q(\omega_0) + i\kappa(\omega_0) = -\frac{\Psi}{d}\left[\arctan\left(\frac{\varepsilon_1}{\varepsilon_t\Psi}\right) + \arctan\left(\frac{\varepsilon_2}{\varepsilon_t\Psi}\right) + \pi l\right], \quad (1.11)$$

where $\Psi = -i\sqrt{\varepsilon_z/\varepsilon_t}$, ε_t and ε_z are the in-plane and out-of-plane permittivities, ε_1 and ε_2 the superstrate and substrate permittivities, and $q(\omega_0)$ and $\kappa(\omega_0)$ are the real and imaginary parts of the complex phonon-polaritonic wavevector, $k_p(\omega_0)$, respectively. As such, PhPs in h-BN can be passively tuned during the sample fabrication by simply controlling the thickness of the crystal, allowing to demonstrate highly-confined SPhPs modes [40]. Moreover, as opposed to all polaritonic cases presented above, these two last equations show that PhPs propagating in h-BN are not surface waves such as graphene SPPs but volume modes [68] (Figures 1.5C, D), which can exhibit high order excitations propagating inside the flake. Note that in this subsection the acronym PhP has been used instead of SPhP to account for the polaritonic volume nature. Additionally, due to the highly-confined nature of PhPs, which yields ultra-slow polaritonic group velocities, and the absence of ohmic losses, polaritonic lifetimes, $\tau = L_p/v_g$, can be up to $1\,ps$ [70]. Indeed, longer lifetimes were demonstrated by isotopically enriching the material, reaching experimental values of $2\,ps$ [71] (note that graphene SPPs and SPPs in noble metals exhibit at least one order of magnitude lower values). Interestingly, PhPs were also found in monolayers of h-BN [72].

Notably, PhPs propagating in both RBs present different trends. Whereas in the upper RB HPhPs propagate with both a positive group velocity ($\vec{v}_g = \nabla_{\vec{k}}\omega(\vec{k})$, parallel to $\vec{S}$) and phase velocity ($\vec{v}_{ph} = (\omega_0/k)\vec{u}_k$, parallel to $\vec{k}$), in the lower RB they propagate with a positive group velocity but a negative phase velocity [70]. This is an exotic polaritonic behavior, as it implies that the maximum propagation length of the upper RB occurs for frequencies close to the TO phonon, whereas in the lower RB it happens in the proximities of the LO phonon frequency.

As mentioned previously, heterostructures fabricated of graphene and h-BN allow merging the unique features of graphene SPPs and h-BN PhPs in a single device due to the excitation of hybrid plasmon-phonon-polaritons (Figure 1.5D, right panel). These heterostructures provide a versatile tool for controlling the flow of light at the nanoscale as its properties can be tuned both by adding free carriers to the system or by changing the h-BN thickness [52, 51, 73].

Several proof-of-concept devices for technological applications have been realized employing h-BN. For example, regarding surface-enhanced infrared absorption (SEIRA) spectroscopy, Autore et al. [6] reported that small amounts of organic molecules can be detected on h-BN nanoribbons thanks to the near-field enhancement provided by the PhP resonances. This device was further improved by the same group employing isotopically enriched h-BN, as it boosted the quality factors of the polaritonic resonances [74]. On the other hand, a photonic crystal made of h-BN was
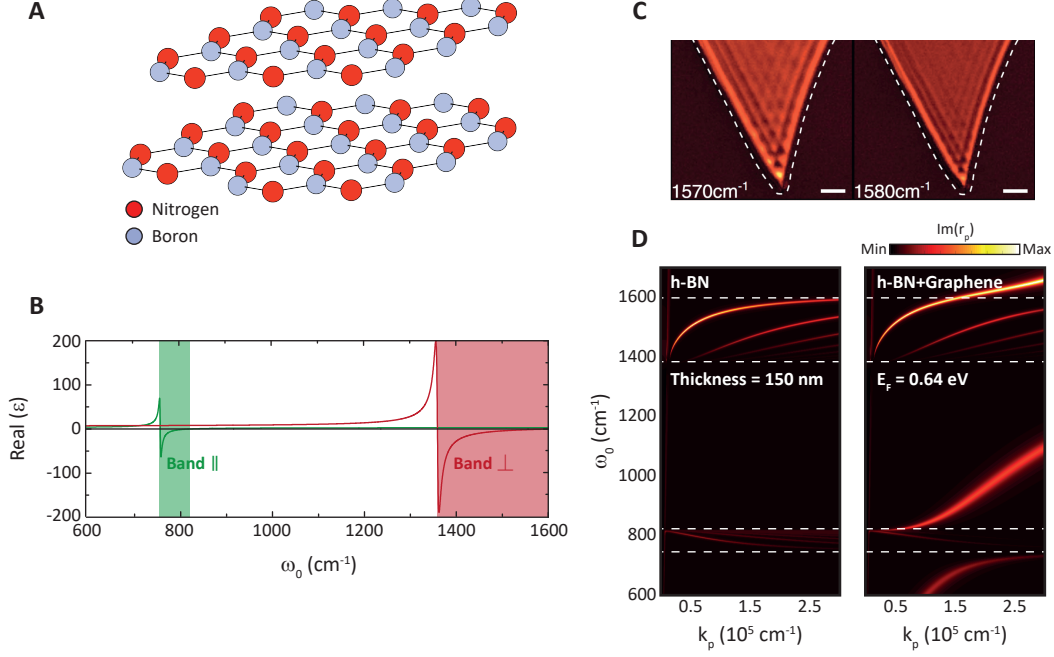
Figure 1.5: Phonon-Polaritons in h-BN A h-BN crystallographic structure. Nitrogen atoms are represented by red spheres and boron atoms are depicted with grey spheres. The h-BN cell parameters are $a = b = 2.51$Å and $c = 6.69$Å (interlayer distance). The space group is P-6 (number 174). **B** h-BN permittivity in the MIR spectral range showing two RBs. **C** IR near-field images of SPhPs propagating in a h-BN slab for two different frequencies. The thickness of the h-BN flake is $256\,nm$. Image taken from [**40**]. **D** Phonon polariton dispersions in h-BN (left pannel) and h-BN with a graphene layer on top (right panel, $E_F = 0.64\,eV$). The h-BN thickness is $150\,nm$ in both cases. High-order modes can be seen inside the h-BN RBs in both cases. The coupling between graphene SPPs and h-BN PhPs results in electromagnetic hybrid modes with dispersion away from the RB (they inherit plasmonic properties). The horizontal dashed lines represent the frequency limits of the h-BN RBs.

also demonstrated supporting highly confined angle- and polarization-independent resonances [**75**]. Also, light trafficking applications were demonstrated by employing phase-change materials [**76, 77**].

Hyperbolic Polaritons

Within the h-BN RBs, the permittivity tensor reaches negative values along either the in-plane crystallographic directions or the out-of-plane crystallographic direction, preserving positive values along the other (**Figure 1.5B**). This is in stark contrast with all isotropic cases presented above, as propagation of polaritons is forbidden along some directions (those presenting positive permittivity). Hence, the isofrequency curve (IFC, a slice of the polaritonic dispersion in the momentum space at a constant frequency) no longer describes a sphere ($|\vec{k}| = k_x^2 + k_y^2 + k_z^2 = \omega^2/c^2$), but a hyperboloid, $|\vec{k}| = h_t^2/\varepsilon_z + k_z^2/\varepsilon_t = \omega^2/c^2$ [**78**]. Notice that either ε_t or ε_z are negative within the RBs. Materials presenting hyperbolic IFC are called hyperbolic media. In isotropic materials, polaritons are able to propagate along all directions with parallel wavevectors and Poynting vectors, $\vec{S} = \mathfrak{Re}(\vec{E} \times \vec{H}^*)/2$, whereas in hy-

10

perbolic media polaritons are only able to propagate along certain directions with a varying angle between the wavevector and the Poynting vector. Parallel $\vec{S}$ and $\vec{k}$ are found along the crystalline directions and perpendicular $\vec{S}$ and $\vec{k}$ along the asymptotes. $\vec{S}$ is always defined by the normal to the IFC (**Figure 1.6A**) in $\vec{k}$ space [**79**, **80**, **81**].

Hyperbolic media hold promises for negative refraction of light [**82**] and subwavelength imaging [**81**]. Close to the asymptotes directions, arbitrary large polaritonic wavevectors yield extremely small polaritonic volumes (limited theoretically only by the cell parameters of the material), leading thus to potential applications were extremely deep subwavelength polaritonic propagation of polaritons are needed. Furthermore, since the emission pattern of polaritons excited by dipolar sources in hyperbolic media is described by the Green's function (which physically relates the electric field generated in $\vec{r}$ by any arbitrary polarization field in $\vec{r}\,'$ [**83**]), the number of available polaritonic wavevectors per solid angle along the directions close to the asymptotes augment greatly, yielding strongly directional polaritonic ray-like propagation. Since the hyperboloid asymptotes in h-BN are given by $\tan\theta(\omega) = i\sqrt{\varepsilon_t(\omega)/\varepsilon_z(\omega)}$ [**84**, **85**, **68**], hyperbolic polaritons in a h-BN slab propagate like reflecting rays at the top and bottom faces (**Figure 1.6B**).

Out-of-plane hyperlensing and hyperfocusing capabilities exhibiting long-distance super-resolution and waveguiding were implemented thanks to the hyperbolic nature of PhPs in h-BN (**Figure 1.6C**) [**84**, **85**, **86**].

However, the main limitation of PhPs in h-BN arise from their natural out-of-plane hyperbolicity. For nanophotonic applications it would be more interesting to develop compact platforms where in-plane propagation of hyperbolic polaritons could be realized [**87**]. Li et al. [**47**] proposed an h-BN nanostructured metasurface as a possible solution. By applying the effective medium theory they found the grating parameters needed to modify the out-of-plane hyperbolicity into an in-plane hyperbolicity. However, although this approximation was able to amplify the phonon-polaritonic confinement in the metasurface with respect to the unpatterned h-BN, the fabrication process prevents the system to be suitable for integrated flat polaritonic applications, as the polaritonic quality factor, $Q = \mathfrak{Re}(k_t)/\mathfrak{Im}(k_t)$, and lifetimes were reduced by a factor of 35%.

1.3 │ s‑SNOM as Nanophotonics Tool

Scattering-type scanning near-field optical microscopes (s-SNOM) have played a fundamental role in polaritonics [**88**, **89**, **90**, **91**, **92**, **93**]. Contrary to far-field microscopes, where transmitted or reflected light by a sample is collected while being illuminated, near-field microscopes rely on inspecting the optical properties of samples by approaching a nanoprobe to their near field. Upon illumination, objects produce both propagating and non-radiative fields (evanescent waves) at their surface, also known as near-fields. The material information encoded into the near-field is generally lost in typical far-field microscopy schemes as the field decays within ranges of tens of nanometers. Near-field microscopes allow radiating and collecting in the far-field the near-field information scattered by nanoscale probes in close contact to the specimen. As such, s-SNOM has been applied to extract locally and with nm resolution information about Raman spectra [**94**, **95**], IR spectra [**96**, **97**],
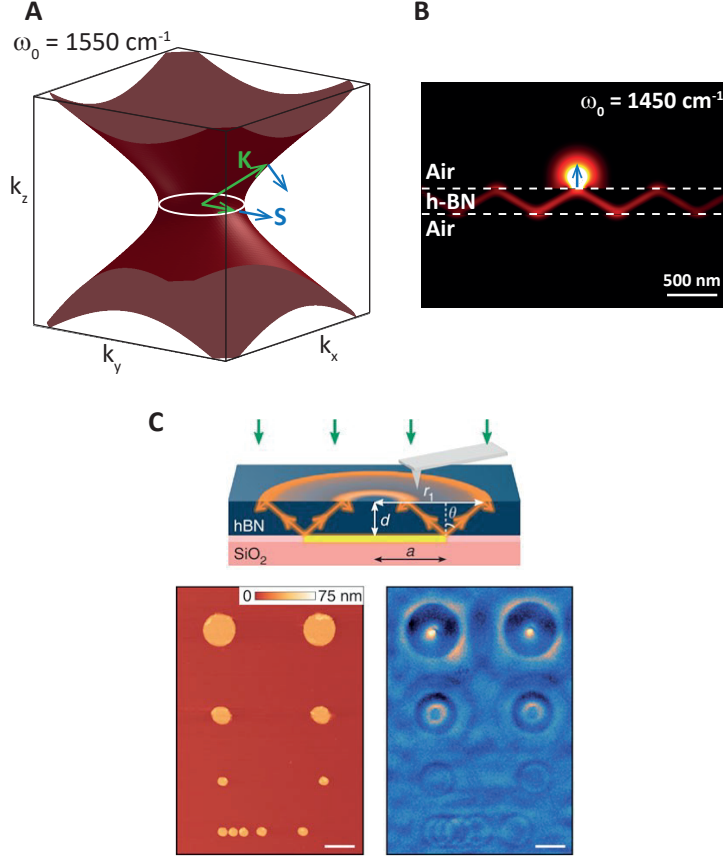
Figure 1.6: Hyperbolic Polaritons in h-BN **A** Phonon polaritonic isofrequency contour (IFC) in h-BN at $\omega_0 = 1550\,cm^{-1}$. Green arrows represent the PhP wavevector whereas the blue arrows represent the Poynting vector. $\vec{k}$ and $\vec{S}$ are parallel along the 'x' and 'y' axes and perpendicular along the asymptotes. **B** Out-of-plane hyperbolic rays propagating in a $150\,nm$-thick h-BN flake launched by a vertical dipole at $\omega_0 = 1450\,cm^{-1}$. The polariton rays are reflected at the interfaces. **C** Lensing with hyperbolic PhPs in h-BN. A sketch of the phenomenon is depicted in the upper panel. Polaritons launched by a buried Au circular antenna (depicted as a yellow rectangle between h-BN and SiO_2) can be seen in the top interface of the h-BN flake. Depending on the excitation frequency, two circumferences with different radii will be obtained. At a certain frequency, hyperbolic rays will be launched purely along the vertical direction, enabling thus a perfect circle to be observed in the image. At that frequency, the system turns out to be a perfect lens. The left bottom panel show the experimental AFM measurements of the Au disks before placing the h-BN slab on top. The right bottom panel shows a s-SNOM image taken at $\omega_0 = 1515\,cm^{-1}$ in a $395\,nm$-thick h-BN flake. The near-field rings are concentric with the Au disks. Image taken from [84]

fluorescence [98] or even the complex permittivity of materials [41, 99].

Specifically, s-SNOM systems are based on atomic force microscopes (AFM) in which an oscillating metal-coated AFM tip illuminated by a laser raster scans the sample (see **Figure 1.7**)*. The metal tip serves as both confiner and enhancer as well as scatterer of the light, working as a near-field nanoantenna and near-field

---

*For a more detailed explanation of the working principle of s-SNOM see Section 2.3

nanorecorder at the same time. The tip thus allows wavelength-independent resolution, limited only by the diameter of the tip. Furthermore, due to the reduced dimensionality of the tip apex, when metallized and illuminated it provides the necessary momentum to give rise to polaritonic excitation [**89**, **90**, **100**].

To understand the information extracted by s-SNOM, the near-field interaction between the tip and the sample can be calculated using a simple point-dipole model [**101**]. By representing the AFM tip as a small dipolar sphere, it enables reproducing qualitatively the s-SNOM images. This simple model was further extended by considering the tip as a prolate spheroid [**102**], allowing to reproduce the image contrast measured by the AFM tip in a more accurate fashion. Indeed, ultra-high phonon polariton field enhancements were predicted and experimentally verified thanks to this model [**29**].

To effectively remove the background signals that introduce artifacts into the near-field images, it has also been introduced a pseudoheterodyne detection technique in s-SNOM. The technique consists of a Michelson interferometer attached to the light path of the system, acting as a reference beam. By demodulating the near field signals at higher harmonics of the tip resonance frequency [**91**, **93**], it allows measuring the polaritonic near-field amplitude and phase with fully background suppression. The technique will be fully introduced in Section 2.3.
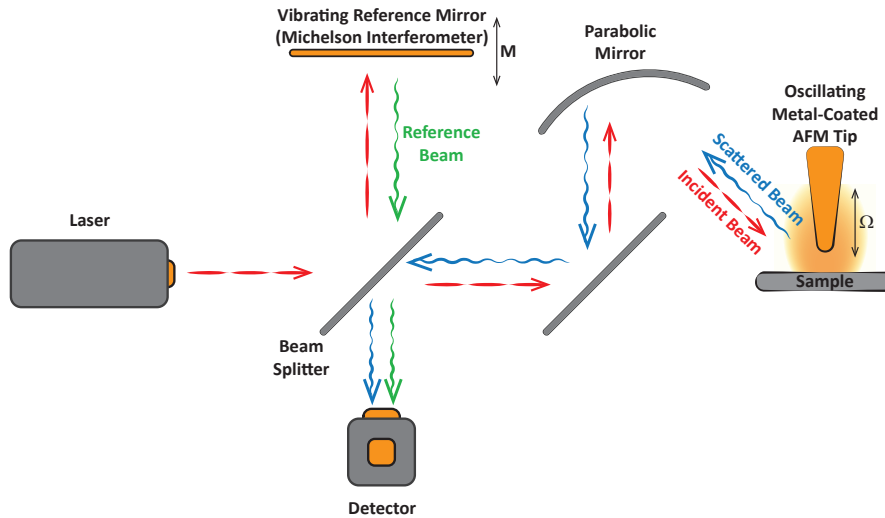
Figure 1.7: Sketch of a s-SNOM s-SNOM working principle. Light emitted by a laser is divided into two optical paths by a beam splitter. The first path is brought to a parabolic mirror focusing the light on the oscillating metal-coated AFM tip. The typical oscillation frequencies Ω are $300\,kHz$. The AFM tip both excites and scatters the polaritons back to the far-field, returning the scattered radiation from the same optical path. The other path is directed to a vibrating reference mirror (which acts as a Michelson interferometer) returning by the same path. The mirror vibrating frequency M is about $400\,Hz$. Both signals are merged again in the beam splitter and driven to the detector. Further details will be provided in Section 2.3.

Manipulating and steering deep-subwavelength polaritons can be performed by s-SNOM. Typically, polaritons launched by the illuminated s-SNOM tip travel through the material getting reflected by boundaries. While back-reflecting, they form and

standing-wave pattern due to the interference with the polariton travelling forth. Therefore, the periodicity of polaritonic waves measured by s-SNOM consists of half the polariton wavelength, $\lambda_p/2$. These waves are called 'tip-launched' polaritons. Furthermore, boundaries may also launch polaritons with a periodicity equal to the polariton wavelength, λ_p, the so-called 'edge-launched' polaritons. Altogether, s-SNOM images typically exhibit polaritonic doublets due to both contributions [103].

Some of the proof-of-concept devices, or research areas, realized recently thanks to s-SNOM systems include planar graphene plasmon polariton waveguides [38], polaritonic focusing of polaritons with tailored nanoantennas [15, 66, 104] planar polaritonic refractor and lenses [105], programmable polaritonic optical elements employing phase-change materials [77, 105, 106, 107], superlenses and hyperlenses [84, 85, 108], photocurrent nanoscopy [109] or fundamental polaritonic studies at terahertz regimes [46, 110].

1.4 | Scope and Organization of the Thesis

The present dissertation will be focused on the study of in-plane hyperbolic phonon-polaritons in van der Walls materials, namely, the alpha-phase molybdenum trioxide, α-MoO$_3$, and the alpha phase vanadium pentoxide, α-V$_2$O$_5$. This study is organized as follows: In Chapter 2 an introduction to the techniques employed in this thesis is presented. In particular, the exfoliation of van der Waals materials, Fourier transform infrared spectroscopy (FTIR), scattering type scanning near-field optical microscopy (s-SNOM), scattering type near-field nanospectroscopy (nano-FTIR) and full-wave numerical simulation techniques are described in detail. Chapter 3 describes the in-plane anisotropic and hyperbolic propagation of polaritons in the vdW material α-MoO$_3$. Excitingly, ultra-slow group velocities and ultra-high polaritonic lifetimes are found for these polaritons. Thus, taking advantage of the unique opportunities afforded by hyperbolic vdW crystals, we demonstrate the first proof-of-concept nanophotonic devices that enable ultra-focusing of light at the nanoscale. Chapter 4 presents a novel route to spectrally shift the RBs in layered materials, expanding the frequency ranges of polaritons. This is achieved by intercalating the vdW semiconductor α-V$_2$O$_5$ with alkaline and alkaline-earth atoms. A full understanding of propagating polaritons in this material is also provided. In Chapter 5 the fundamental limits of polaritons in terms of lifetimes are investigated. Using cryogenic FTIR and s-SNOM measurements, supported by *ab initio* DFT calculations, we provide an in-depth understanding of the inherent damping mechanisms of in-plane hyperbolic polaritons.

Experimental Techniques

In this chapter an introduction to the experimental techniques employed throughout the thesis is provided. These include the exfoliation of vdW materials and the use of the dry-transfer method, Fourier Transform Infrared Spectroscopy, and the most widely employed technique over the thesis, the s-SNOM. s-SNOM Nano-Spectroscopy (carried out at the Nanooptic group at CIC nanoGUNE) is also introduced based on the previous mentioned FTIR and s-SNOM techniques. Finally, a brief introduction to full-wave numerical simulations is provided.

2.1 | Exfoliation of vdW Materials and Dry-transfer Technique

Controlling the number layers in vdW materials is essential to predict their behavior and engineer their properties on demand [48, 111, 112]. For example, the wavelength of h-BN phonon polaritons varies as a function of the slab thickness [40], as shown in the previous chapter. Layered stacks of different van der Waals materials result in physical systems with richer physics and enhanced characteristics compared to isolated layers [52]. Strain fields lead to blue shifts of Raman peaks in a h-BN monolayer, while they lead to red shifts in bilayers [113]. The bandgap of some vdW materials, such as MoS_2, depend directly on the number of vdW layers, being direct in the monolayer case (with an enhancement of the luminescence quantum emission more than a factor 10^4 [36]) and indirect otherwise. Therefore, the exfoliation of van der Waals flakes and their deterministic placement on a desired substrate play a fundamental role in the study of the opportunities offered by these materials [50].

In this section, we will introduce the exfoliation and dry-transfer techniques used to obtain 2D crystals with different thicknesses on arbitrary substrates. Although a wide number of exfoliation methods have been developed in the last decade [114], we will focus in this thesis on the standard mechanical cleavage procedure that was used for the very first isolation of graphene in 2004 [30]. Specifically, it will be used a top-down method for thinning down the vdW bulk crystal using a commercially available tape. Afterwards, a dry-transfer setup will be used for the transfer of selected crystals on arbitrary substrates with a micrometer resolution in the positioning of the crystals [49].

The mechanical exfoliation method consists in several steps (**Figure 2.1A**):

- The vdW bulk crystals are placed on top of a commercial tape (Nitto SPV 224PRM LB, in the following, 'blue tape').

- Part of the tape is folded onto the bulk crystal and retraced gently. By proceeding this way, the bulk crystal is divided into two pieces.

- By repeating the last step several times, one can thin down the bulk crystal progressively until an arbitrary distribution of relatively thin crystals is observed over the tape.

- Once thinned down, the blue tape with the crystals is put into contact with a stamp of polydimethylsiloxane (PDMS, Gelpak WF-20/1.5-X4) that was treated with ozone during 1-2 minutes to enhance the adhesion of the crystals to the PDMS. This allows picking up a larger number with larger lateral dimensions. To facilitate its handling, the PDMS stamp is attached to a microscope slide by a doubled sided tape.

- Finally, the PDMS is examined in the optical microscope either in transmission or reflection mode to select those crystals with approximately the desired thicknesses (**Figure 2.1B**).

Typically, a variety of randomly distributed flakes with different color is observed on the PDMS stamp. The optical contrast between the different flakes, and between the flakes and the PDMS, is governed by the Fresnel coefficients [**115**] which, in turn, are dictated by the thickness dependence of each layer (supposing we are dealing with an air/vdW flake/PDMS system) [**5**]. Hence, the thickness of the flakes determines its color, and thus, a flake with a desired thickness can be easily identificated by just inspecting the PDMS substrate with the optical microscope [**116, 117**]. Note that the adhesion forces between the flakes and the PDMS material arise from the PDMS viscoelastic behavior, governed by vdW forces [**49**]. **Figure 2.1C** shows optical images for two crystals with different thicknesses, and therefore different colors.

The flakes attached to the PDMS stamps are released on the target substrate by using the dry-transfer technique. This setup consists of different parts, such as micrometer screws to manipulate the relative position of the flake and the target substrate, and an optical microscope to observe in-situ the transfer process (see **Figure 2.2**). In the following, we describe the steps typically followed with a dry-transfer technique:

- The PDMS containing the exfoliated flakes is attached with a double-sided tape at the border of a glass slide, which in turn is attached to a micrometer XYZ stage (with the PDMS facing down).

- The substrate on which the crystals will be transferred is attached on the substrate holder using a vacuum pump.

- In this configuration, since the PDMS is an optically transparent material, both the flake on the PDMS and the substrate surface can be seen simultaneously. With the help of the optical microscope and the XYZ micrometer screws, the relative position between the selected flake and the substrate can be easily modified. Once this is done, the PDMS stamp with the crystal is approached towards the substrate surface until they get into contact with each other.

- Then, the substrate is heated up to around $150°C$ at which the PDMS stamps lose their viscoelastic behavior and, therefore, an almost 100% releasing yield is obtained.

- Finally, to release the crystal on the substrate, the glass slide is lifted up slowly.

After this process, the sample is annealed at $180 - 200°C$ during $3 - 5$ minutes to ensure a better adherence between the substrate and the flake.
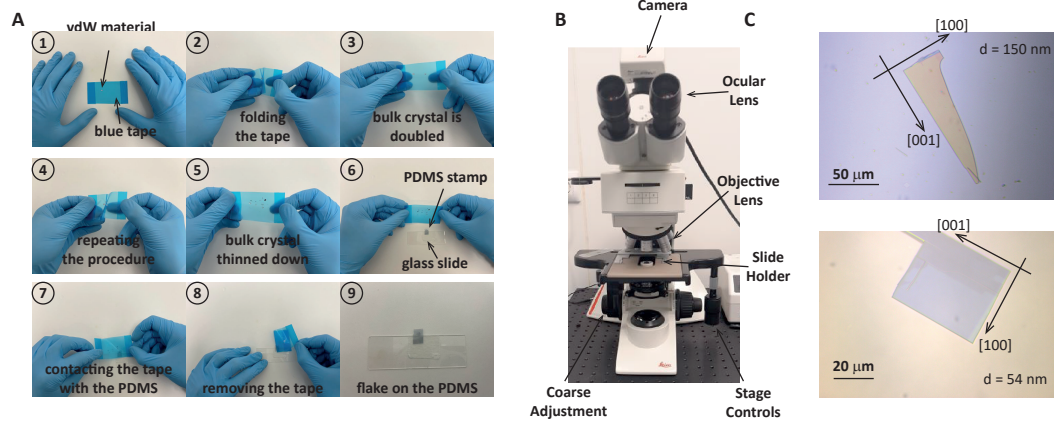
Figure 2.1: Exfoliation Procedure **A** Sketch of the exfoliation procedure. The images show the folding-unfolding process to thin-down and exfoliate the bulk vdW crystal on the PDMS stamp in 9 steps. The PDMS stamp is inspected through the microscope after this process. **B** Image of the Leica optical microscope (leica-microsystems.com) employed in this thesis to identify suitable flakes. **C** Optical image of two different MoO_3 flakes with thicknesses $d = 150\,nm$ and $d = 54\,nm$. The color of the flake depends on its thickness.
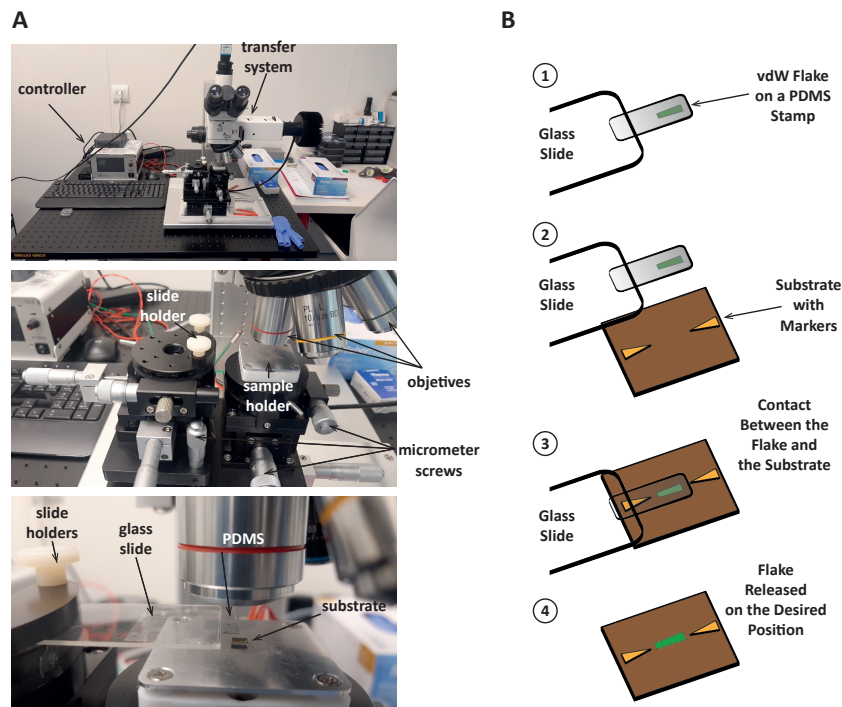
Figure 2.2: Dry-Transfer Process **A** Images of the HQGraphene dry-transfer system employed in this thesis. The substrate is firmly attached to the substrate holder thanks to a vacuum pump. The controller allows us to regulate the temperature of the substrate holder between 0 and $200°C$. **B** Sketch of the transfer procedure in 4 steps. By increasing the temperature above $150°C$ the PDMS viscoelasticity decreases strongly, allowing us to release the flake with almost a 100% yield.

2.2 | Far-Field Characterization: Fourier Transform Infrared Spectroscopy (FTIR)

Infrared spectroscopy is a powerful technique for characterizing the optical properties of materials. Particularly interesting is to characterize vibrational motions of molecules, lattice vibrations in solids or plasmonic excitations in metals that are present at certain resonant frequencies. The specific spectrum of such resonances for a given material can be used as a 'fingerprint' to unequivocally identify the material. In this regard, Fourier transform infrared spectroscopy (FTIR) is a widely employed technique that allows to obtain the full mid-infrared (MIR) spectra of a sample (either in transmission or reflection) with high spectral resolution. Basically, in this technique light from a broadband source (typically a filament or a small coil) is driven through a Michelson interferometer and then focused on the sample. The reflected/transmitted signal is afterwards detected and processed on a computer to display the resulting spectrum.

Figure 2.3 sketches a typical FTIR spectroscopy system in reflection mode. Moreover, **Figure 2.4** show some pictures of the FTIR system available at University of Oviedo. Light from an IR broadband source passes through a Michelson interferometer (dashed square) that consists of a beam splitter (green line) that divides the beam into two rays, one driven to a fixed mirror and another to a vibrating reference mirror, creating an optical path difference between them (i.e., a phase difference). Upon reflection, both beams interfere in the beam splitter and are brought thorough a polarizer and an objective to the sample. The reflected beam is collected at a detector using another beam splitter. Importantly, the detected signal $I_r(\omega)$ is normalized to the signal of a material with an optically flat-response in the MIR, $I_{Bakcground}(\omega)$ (all FTIR measurements in this thesis were taken in reflectance using gold as normalization substrate). As such, the ratio $R = I_r(\omega)/I_{Background}(\omega)$ is the resulting FTIR reflectivity spectrum of the sample (given by **Equation 2.4** and explained in the following pages).

Regardless of measuring reflection or transmission spectra, the spectra obtained will be governed by the refractive index, $\hat{n}(\omega) = n(\omega) + i\kappa(\omega)$, which is the square of the relative permittivity of a material, $\hat{\varepsilon}(\omega) = \varepsilon'(\omega) + i\varepsilon''(\omega)$. Commonly, the real part of the refractive index $n(\omega)$ is simply called as 'refractive index' and the imaginary part $\kappa(\omega)$ as the 'absorption index'. The reflectivity, R, is defined as the fraction of the incident energy that is reflected, such as [5]:

$$R = |r|^2 = \left|\frac{E_r}{E_0}\right|^2 \tag{2.1}$$

with E_0 being the incident electric field, E_r the reflected electric field, and r the Fresnel reflection coefficient. Typically, this last equation is splitted into two cases depending on the polarization of the incident light: p polarization (or transversal magnetic waves, TM) and s polarization (or transversal electric waves, TE).

Supposing that we are dealing with a system composed of three different media (each of them with a reflective index $\hat{n}_1$, $\hat{n}_2$ and $\hat{n}_3$, such as the one depicted in **Figure 2.5**), the reflectivity will be given by the following relation [5]:
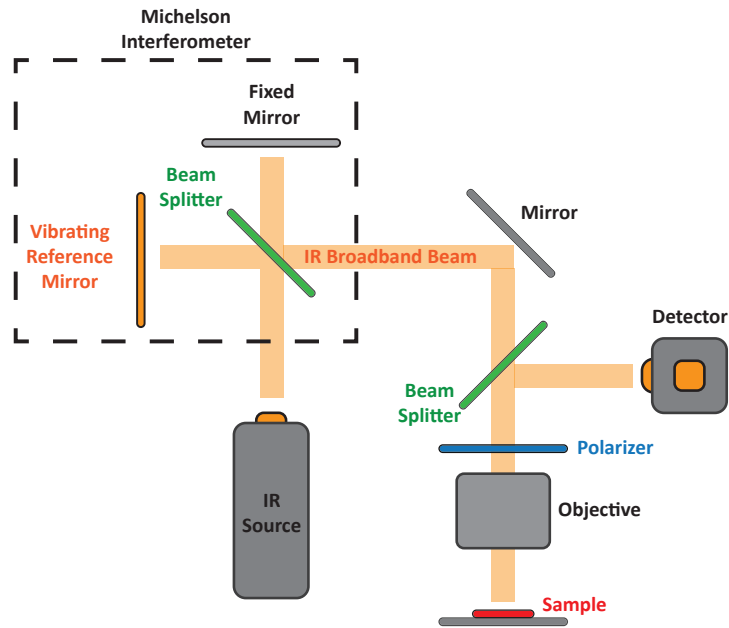
Figure 2.3: Sketch of a FTIR System in Reflectance Mode Light from an IR source is sent to a Michelson interferometer (black dashed line box). This consists of a beam splitter (green line) that divides the beam into two rays, one driven to a fixed mirror and another to a vibrating reference mirror, creating an optical path difference between them (i.e., a phase difference). Upon reflection, both beams interfere in the beam splitter and are brought thorough a polarizer and an objective to the sample. The reflected beam is collected at a detector using another beam splitter.
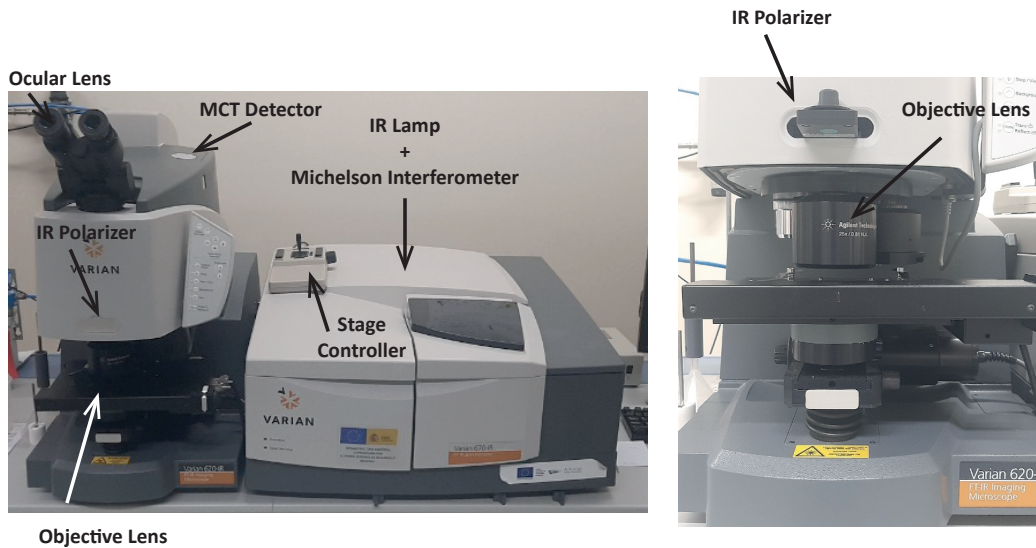
Figure 2.4: FTIR System Images of the FTIR system employed in this thesis at University of Oviedo. Left image represent the whole system which has one module for the IR lamp and the Michelson interferometer and other module with the objectives and detector. Right image shows a zoom-in of the objectives module with the IR polarizer.

$$R = \left| \frac{r_{12} + r_{23}e^{2i\beta}}{1 + r_{12}r_{23}e^{2i\beta}} \right|^2 \tag{2.2}$$

19
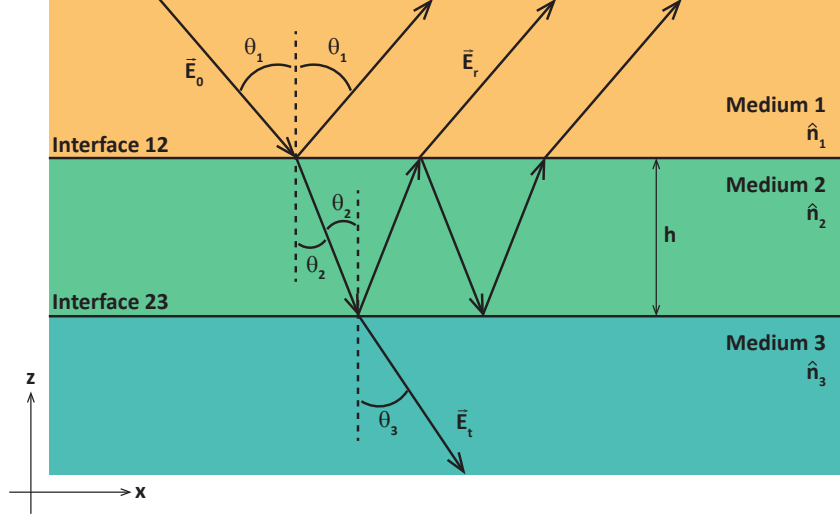
Figure 2.5: Transmitted and Reflected Light Passing Through a Dielectric Film Sketch of the propagation of electromagnetic waves through a thin film of thickness h (with refractive index $\hat{n}_2(\omega)$) embedded between two semi-infinite media (with refractive index $\hat{n}_1(\omega)$ and $\hat{n}_3(\omega)$). Light impinging from medium 1 into medium 2 can be partially reflected and transmitted. The same principle works for light impinging from medium 2 on medium 3. The interface between media 1 and 2 is labelled as 'Interface 12', and the interface between media 2 and 3 is labelled as 'Interface 23'. The reflection/transmission angles for each medium are labelled as θ_1, θ_2 and θ_3.

where r_{12} and r_{23} are the Fresnel reflection coefficients at the first (between media 1 and 2) and second (media 2 and 3) interfaces, $\beta = 2\pi n_2 h \cos(\theta_2)/\lambda_0$ with h the thickness of the second layer, and θ_2 is the angle between the electric field propagating in the medium 2 and the z direction. Typically, the first medium is air, the second medium the sample, and the third medium the substrate (SiO_2 and BaF_2 are among the most widely used). The last equation is general and valid for both s and p polarizations [118]. However, the expressions for r_{12} and r_{23} depend on the polarization of light [119]. The following relations account for the Fresnel reflection coefficient r depending on whether we have s or p polarization:

$$r_{s,ij} = \frac{n_i \cos\theta_i - n_j \cos\theta_j}{n_i \cos\theta_i + n_j \cos\theta_j}; \quad r_{p,ij} = \frac{n_i \cos\theta_j n_j \cos\theta_i}{n_i \cos\theta_j + n_j \cos\theta_i} \tag{2.3}$$

With ij denoting the interface between medium i and medium j (this is, 12 or 23). Therefore, depending on the illuminating conditions, the measured reflectivity spectra will have a contribution from both s-polarization and p-polarization signals:

$$R = \frac{1}{\sqrt{2}}(\alpha R_s + (1-\alpha)R_p) \tag{2.4}$$

with α a value ranging from 0 to 1. In the optical configuration of the FTIR system used in this thesis (see **Figure 2.4**), the average incident angle is $\theta_1 \approx 15°$, so normal incidence can be taken as a good approximation ($\theta_1 = \theta_2 = \theta_3 = 0°$) and the above equations can be notably simplified.

FTIR reflectivity spectra provide a useful tool to extract the sample permittivity for the measured frequency range. This information is very important to predict the

propagation properties of polaritons (as shown in the previous chapter, polaritons such as SPPs in graphene or PhPs in h-BN are strongly affected by the permittivities of the substrate and superstrate used) and makes FTIR a key technique in nanophotonics (typically also the permittivity of polaritonic materials has only been studied in the visible range, being its infrared properties widely unknown). A detailed description of the working principle of the FTIR technique is given in the reference [120]. In the following, we also provide a detailed description of a Michelson interferometer due to its special relevance in both FTIR and in s-SNOM, as we will see later.

As shown in the sketch of **Figure 2.3** (black dashed rectangle), a Michelson interferometer divides an incident beam into two through a beam-splitter. One of them impinges on a fixed mirror and is reflected back to the beam-splitter whereas the other is brought to a movable mirror and also back-reflected to the beam-splitter, causing an optical path difference (phase difference) between both beams. As such, an interference at the beam-splitter is obtained as a function of the path difference, δ. The electric fields from both arms A and B are:

$$E_A = |E_A|e^{i\omega_0 t}; \ E_B = |E_B|e^{i\omega_0 t + \phi} \tag{2.5}$$

with $\phi = 4\pi\omega_0\delta$ (ω_0 in spectroscopic units, i.e., $\omega_0 = \lambda_0^{-1}$ where λ_0 is the incident wavelength). The intensity measured at the detector will be thus given by:

$$I_D(\delta) = |E_A + E_B|^2 = |E_A|^2 + |E_B|^2 + 2|E_A||E_B|\cos(4\pi\omega_0\delta) \tag{2.6}$$

If both trajectories are identical then $\delta = 0$ and the interference will be constructive, being the measured intensity maximum. On the other hand, if the path difference is half of the incident wavelength, $\delta = \lambda_0/4$, the interference will be destructive and the measured intensity minimum. Assuming that the norm of the incident electric field is divided by 2 at the beam splitter then $|E_A| = |E_B| = |E_0|/2$, and the last equation can be simplified to:

$$I_D(\delta) = \frac{1}{2}I_0\left(1 + \cos(4\pi\omega_0\delta)\right) \tag{2.7}$$

where $I_0 = |E_0|^2$. However, this assumption is only valid for ideal cases, and the real signal detected may change due to different factors such as the quality of the beam-splitter or the response of the detector. Hence, a wavenumber-dependent factor R_0 is introduced to account for such instrumental deviations:

$$I_D(\delta) = \frac{1}{2}I_0 R_0\left(1 + \cos(4\pi\omega_0\delta)\right) \tag{2.8}$$

We can identify two different terms in the last equation: a constant one that does not depend on the optical path difference δ, and a modulated term that does depend (the cosine) which is called the *interferogram* and is the only important component in spectroscopic measurements:

$$S(\delta) = \frac{1}{2}I_0 R_0 \cos(4\pi\omega_0\delta) = B_0 \cos(4\pi\omega_0\delta) \tag{2.9}$$

With $B_0 = I_0 R_0/2$.

When dealing with broadband sources, the interferogram is represented by an integral [120]:
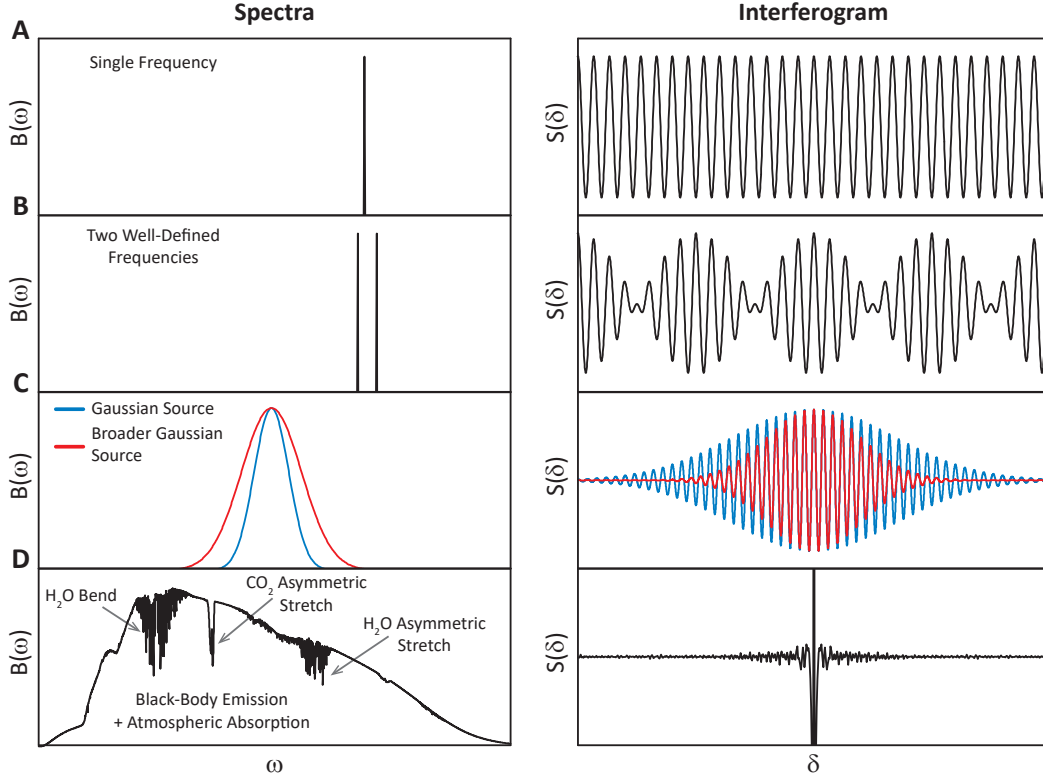
Figure 2.6: Spectra and Interferograms for Different Light Emission Sources Spectrum (left panel) and interferogram (right panel) for: **A** a single frequency, **B** two well-defined frequencies, **C** two gaussian sources, a broad one (red curve) and a narrow one (blue curve), and **D** a real lamp emission source (black-body source) showing also the CO_2, water and other atmospheric absorption bands.

$$S(\delta) = \int_{-\infty}^{\infty} B(\omega) \cos(2\pi\omega\delta)d\omega \tag{2.10}$$

According to the Fourier inversion theorem, the spectrum of the interferogram reads:

$$B(\omega) = \int_{-\infty}^{\infty} S(\delta) \cos(2\pi\omega\delta)d\delta \tag{2.11}$$

Since $S(\delta)$ is an even function it is only needed to calculate the integral from $\delta = 0$ to $\delta = \infty$. Let us consider the simplest case: a source that emits radiation at well-defined wavelengths. The resulting interferogram will be an infinitely periodic repetition of a modulated sinusoidal envelope (right panels in **Figure 2.6A, B**).

In case of broadband Gaussian sources (**Figure 2.6C**), the interferogram shows an exponentially decaying modulated envelope. The narrower the width of the spectral source, the wider the interferogram envelope. On the other hand, typical FTIR sources are based on the black-body emission of a filament or a coil, leading to interferograms such as the one shown in **Figure 2.6D**. The obtained infrared spectrum upon performing the Fourier transform shows the particular envelope of the black-body radiation plus characteristic dips due to the atmospheric absorption (mainly CO_2 and water). These atmospheric absorption mechanisms introduce undesired contributions that should be removed properly, as well as other factors
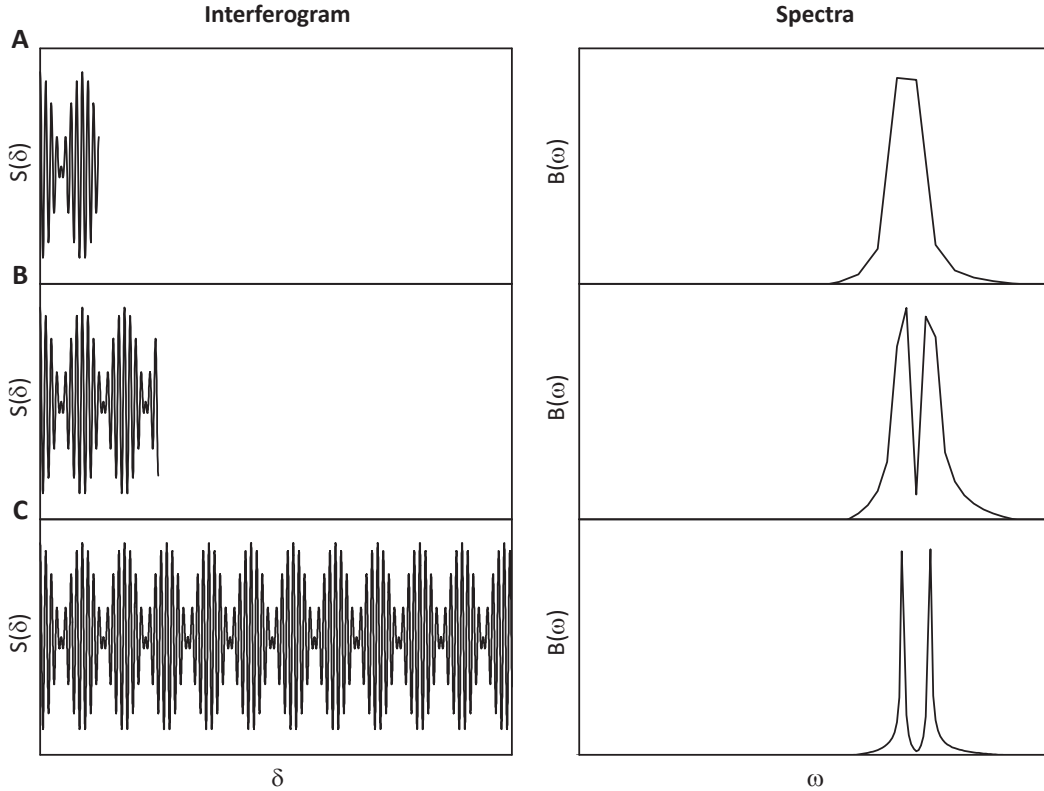
Figure 2.7: Spectral Resolution in a Michelson Interferometer Interferogram (left panel) and spectrum (right panel) obtained by performing the Fourier transform, for **A** a small moving reference mirror distance d_t, **B** $2d_t$, and **C** $8d_t$. As can be seen in the spectra panels, the higher the moving reference mirror distance, the larger the spectral resolution obtained.

such as the finite displacement of the mirror that cause a broadening of the emission lines. This is typically done by normalizing the FTIR spectra taken on the sample to the FTIR spectra taken out of it (background signal) using the relation $B_{sample}(\omega)/B_{Background}(\omega)$. In particular, since FTIR measurements can be done in both reflection and transmission mode, the normalization to the background signal is carried out differently. For transmission measurements, the background spectrum is taken by removing the sample, while for reflection mode it is taken on a MIR flat material, such as silicon or gold.

It is interesting to note that equation (**Equation 2.11**) states that theoretically we can obtain the spectrum with infinitely-high resolution. However, in the experiment, this is limited by the maximum range of the moving mirror, which eventually dictates the finite achievable resolution of the system $\Delta\omega$ (defined as the inverse of the maximum moving mirror distance d_t). As an example, let us assume that we have a source that emits radiation at two well-defined wavelengths (**Figure 2.6B**), due to the maximum distance attainable with the reference moving mirror, d_t, we will only be able to measure a part of the complete interferogram. Depending on the distance d_t, both emission lines of the source may not even be resolved (**Figure 2.7A**). However, if d_t is doubled, both emission lines can now be resolved (**Figure 2.7B**). As shown in **Figure 2.7C**, only by taking a sufficiently long distance d_t (for example 8 times compared to the case in **Figure 2.7A**), both emission lines will be

resolved with high-resolution.
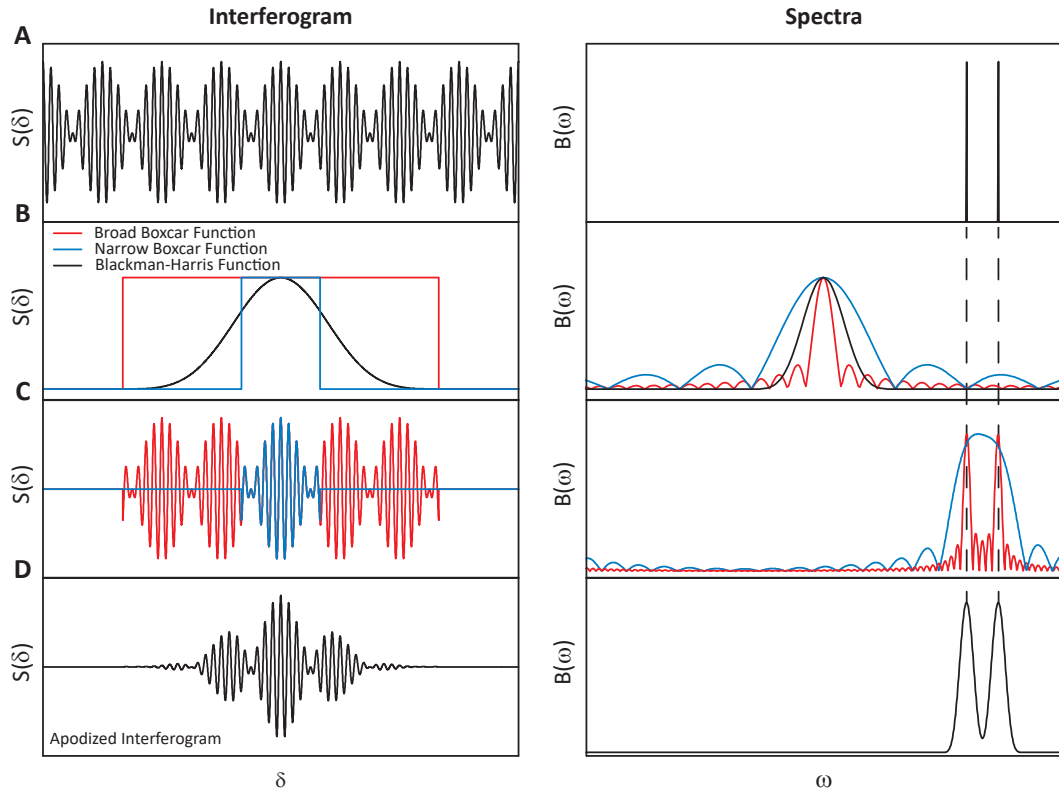
Figure 2.8: Apodization of an Interferogram Interferogram (left panel) and spectrum (right panel) for: **A** a well-defined double frequency source, **B** broad (red) and narrow (blue) boxcar truncation functions and Blackman-Harris function (black), **C** truncated interferograms resulting from the multiplication of the broad (red) and narrow (blue) boxcar truncation functions, which model the finite moving distance of the reference mirror. When the distance is large enough (red curve), both frequencies are resolved. However, clear oscillatory artifacts are observed. If the moving distance of the reference mirror is not large enough (blue curve), the frequencies cannot be resolved. **D** Interferogram resulting from the multiplication of the broad (red) boxcar truncation function of **C** by the Blackman-Harris function. In this case, both frequencies can be clearly identified (right panel) without the introduction of artifacts.

Furthermore, there is another effect related to the limited movement of the reference mirror that might result in non-desired oscillatory artifacts in the surroundings of the source emission frequencies. Mathematically, the effect of a limited displacement of the reference moving mirror corresponds to the convolution of the Fourier transform of the infinitely-long interferogram (arising from the two-line perfect emission source) and a boxcar truncation function (this is, a rectangular filter where wider boxcar truncation functions correspond to longer reference mirror distances) [120]. **Figure 2.8** shows how the truncation affects an infinitely long interferogram composed of two well-defined frequencies (ideally represented in **Figure 2.8A**). If the boxcar truncation is wide (red line in **Figure 2.8B**), meaning long moving mirror distances (red line in **Figure 2.8C**), the spectrum shows clearly both emission frequencies with oscillatory artifacts at its sides. On the other hand, if the trun-

cation function is narrow enough (blue line in **Figure 2.8B**), the frequencies are no longer resolved (blue line in **Figure 2.8C**). A way to minimize this problem is the so-called apodization. Apodization is carried out by multiplying the measured interferogram by a function which is maximum at the interferogram center and decays to zero at its border (black line in **Figure 2.8B**). Blackman-Harris functions are typically employed. The apodized spectra (**Figure 2.8D**) does not show the non-desired oscillations; however, there is a cost in terms of spectral resolution (note that the black peaks in the right panels of **Figure 2.8D** are broader than the red peaks in the right panels of **Figure 2.8C**).

Another limitation in FTIR is given by the fact that data cannot be acquired at an infinite sampling rate. Data acquisition cards possess a limited acquisition speed, giving rise to datasets with a finite number of points. The distance between points, i.e., the spectral resolution, is found to be exactly $1/d_t$. Thus, the maximum moving distance of the reference mirror moving distance establish the best spectral resolution we can achievable with our experimental system. This issue can be partially tackled by adding zeros artificially to both sides of the interferogram. This is known as zero-filling or padding and, although the spectrum gets smoother, no new information is obtained as since the spectral resolution is not improved (**Figure 2.9**).
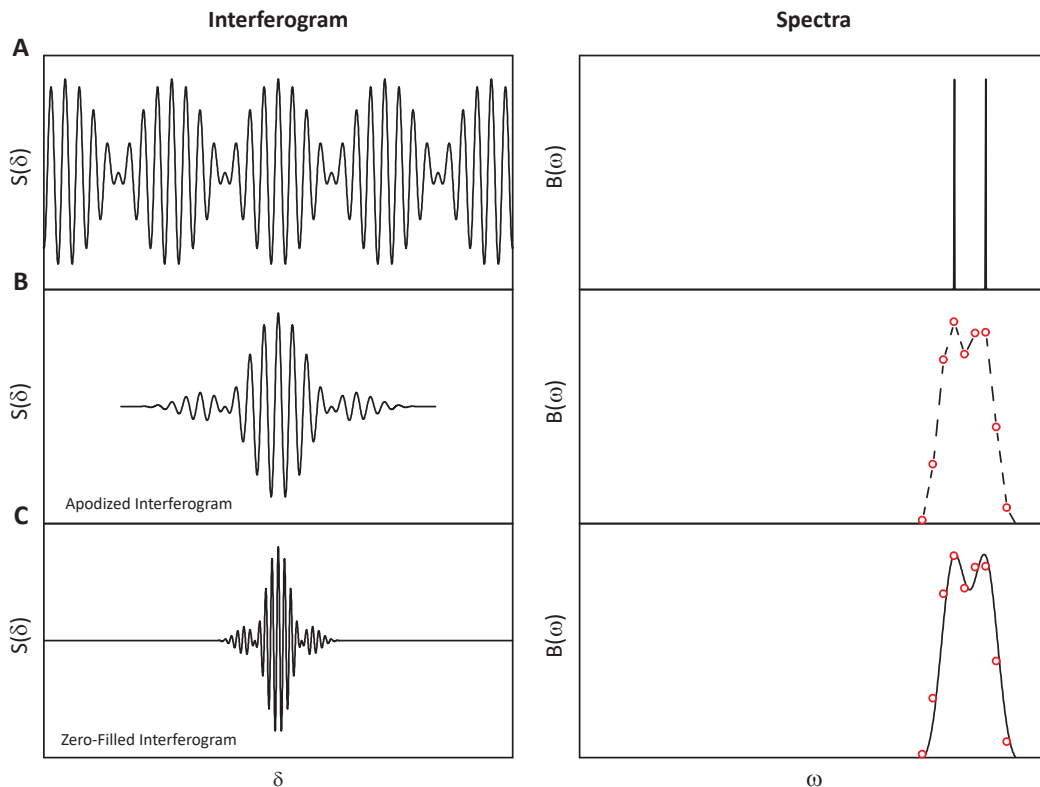
Figure 2.9: Zero Filling of an Interferogram Interferograms (left panel) and spectra (right panel) for: **A** two well-defined frequencies, **B** after apodization (the obtained points, red circles, are connected by dashed lines, and **C** after apodization and zero filling. Both frequencies can be resolved in this case. Original points (red circles) are also shown for a clear visualization.

Importantly, to improve the signal-to-noise ratio in FTIR measurements, the

interferograms obtained are averaged over several scans (**Figure 2.10**).
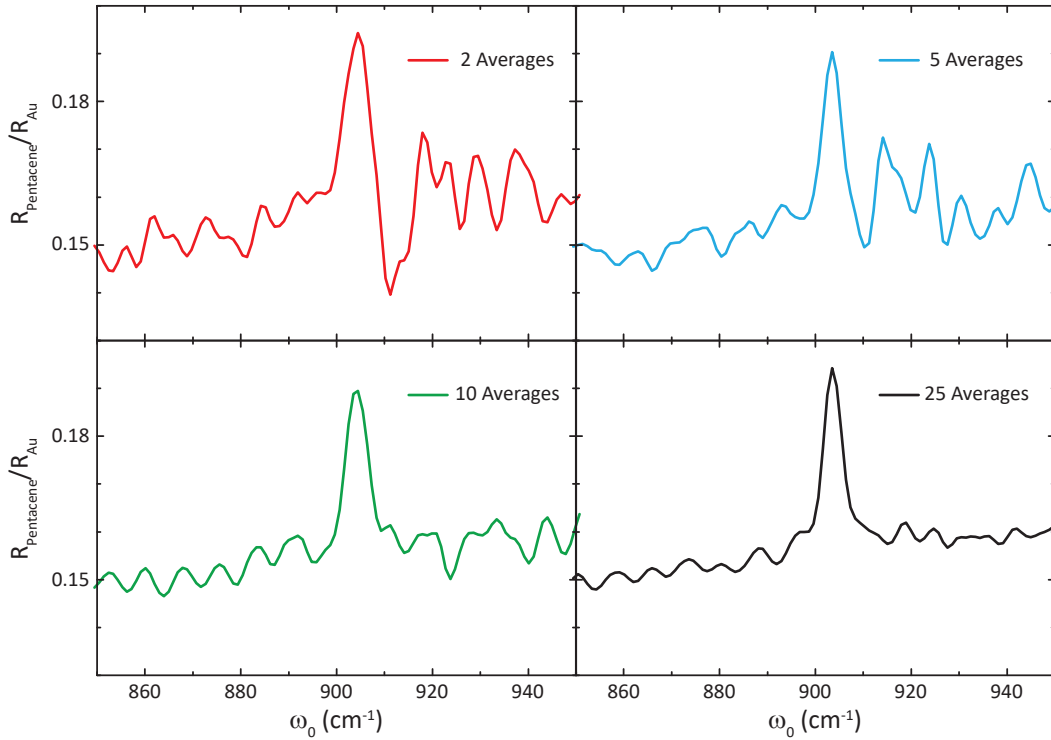
Figure 2.10: Averaging in FTIR Averaged spectra of pentance aftger 2 (red), 5 (blue), 10 (green) and 25 (black) scans. The higher the number of scans, the better the signal-to-noise ratio.

2.3 | Near-Field Characterization: Scattering-Type Scanning Near-Field Optical Microscopy (s-SNOM)

Scattering-type (or apertureless) scanning near-field optical microscopy (s-SNOM) allows to excite and collect highly confined polaritons, such as those studied in this thesis. In particular, the phonon-polaritonic optical signal can be simultaneously obtained in amplitude and phase with wavelength-independent resolution [**90**, **121**, **122**].

s-SNOM (**Figure 2.11**) is an optical technique that is based technically on an atomic force microscope (AFM), which allows to obtain high-resolution topographic images of any type of material. Basically, AFM consists of a nanometric sized cantilevered tip that is scanned across the sample surface while the tip-sample distance is maintained constant. A feedback control system is employed in order to ascertain the tip amplitude does not decrease below a preselected value. For this purpose, a laser beam is focused onto the tip's cantilever. The variations of the cantilever due to the roughness of the sample lead to a displacement of the reflected beam from its equilibrium position which are detected through a photodiode. Typically, a tapping mode is employed in which the cantilever tip oscillates vertically at its mechanical resonance frequency. A piezoelectric actuator attached to the sample holder is used to scan the sample with nanometer resolution. The sample surface

interacts once per oscillation period by the tip with a tapping amplitude typically less than $100\,nm$. As will be shown later in this chapter, the tip oscillation will help us to completely remove the background from the signal . Therefore, together with the optical image, the s-SNOM is able to record the topography of the sample surface.

What differentiates an s-SNOM system from an AFM system is that the tip is in this case also illuminated by high-power continuous wave laser sources (top image in **Figure 2.11**) employing a parabolic mirror. The incident electromagnetic field is concentrated at the very apex of the tip, providing sufficient momentum to the incident field to effectively excite PhPs in van der Waals materials. Simultaneously, the tip also backscatters in all directions towards the far-field (**Figure 2.12A**) the near fields excited at the surface of the material under investigation. These are collected by a detector, which can be a photomultiplier for visible light, a bolometer for terahertz radiation or a mercury calcium telluride (MCT) for infrared light (top image in **Figure 2.11**). Importantly, the radius of the tip apex determines the maximum resolution achievable in s-SNOM, since it establishes the volume in which the incident field is concentrated independently of the wavelength of the incident radiation (it can be seen as the available wavevector distribution in the reciprocal space). In general, the sharper the tip, the stronger the electric field and the higher the field confinement it produces [**93**]. All s-SNOM measurements at single frequencies presented in this thesis were performed using platinum- and iridium-coated silicon tips (ARROW-NCPt-50, NanoWorld AG) with tip radii of about $20\,nm$ exhibiting mechanical resonances of about $\Omega \approx 250 - 300\,kHz$. As a source we employed a mid-infrared tunable quantum cascade laser (QCL) from Daylight solutions (MIRcat-1400, DRS) emitting in the frequency range $850\,cm^{-1}$ to $1695\,cm^{-1}$ while an MCT detector from Kolmar Technologies (KLD-0.1-J1/11/DC) was used as a detector.

Figure 2.11 show the s-SNOM system, lasers and detectors employed to excite and probe polaritonic signals at University of Oviedo.

To describe the physical meaning behind the optical contrast recorded by s-SNOM, several theoretical models were developed during the 1990s (**Figure 2.12A**) [**89**, **101**]. The simplest, known as the point-dipole model (**Figure 2.12B**), presents the AFM tip as a small sphere of radius a with a vertically oriented electric dipole and the sample as an isotropic infinite half-space. Importantly, retardation effects are ignored and the electrostatic approximation is assumed. Thus, the polarizability of the dipole is represented by [**92**, **93**]:

$$\alpha = 4\pi a^3 \frac{\varepsilon_t - \varepsilon_i}{\varepsilon_t + 2\varepsilon_i} \tag{2.12}$$

With ε_t is the permittivity of the dipole (the AFM tip) and ε_i is the permittivity of the surrounding media, typically air ($\varepsilon_i = 1$). The dipole moment induced in the AFM tip is therefore $p_0 = \alpha E_0$, where E_0 represents the illuminating electric field. This dipole moment acts on the sample, creating a mirror dipole (according to the mirror image method) with a moment $p' = p\beta$, being β the so-called dielectric surface response function:

$$\beta = \frac{\varepsilon_s - 1}{\varepsilon_s + 1} \tag{2.13}$$

Where ε_s is the dielectric function of the sample. This mirror acts back on the AFM tip dipole, increasing the strength of its dipole moment. Again, this increase
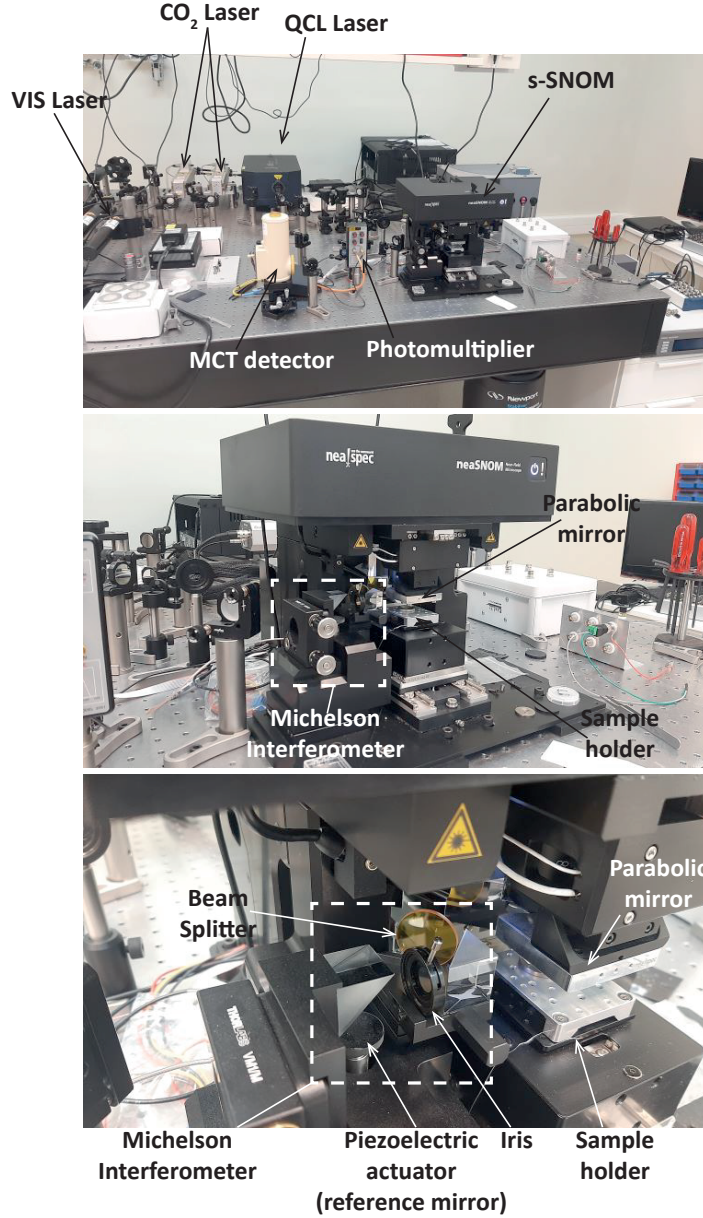
Figure 2.11: s-SNOM Images of the s-SNOM system employed in this thesis at the University of Oviedo.

in dipole moment acts back on the mirror dipole, and so on. As a result, the total dipole moment can be seen as an infinite geometric series:

$$p = p_0 \sum_{n=0}^{\infty} g^n = \frac{p_0}{1 - g} \tag{2.14}$$

where the factor g represents the enhancement in the relative probe-dipole moment after each reflection. It is therefore related to the dielectric surface response function $g \propto \beta$. After some algebra, it can be shown [93] that the total dipole moment takes the form:

$$p = E_0 \frac{\alpha(1 + \beta)}{1 - \frac{\alpha\beta}{16\pi(a+H)^3}} \tag{2.15}$$

where H is the distance between the sample surface and the tip at its lowest position in the oscillation.
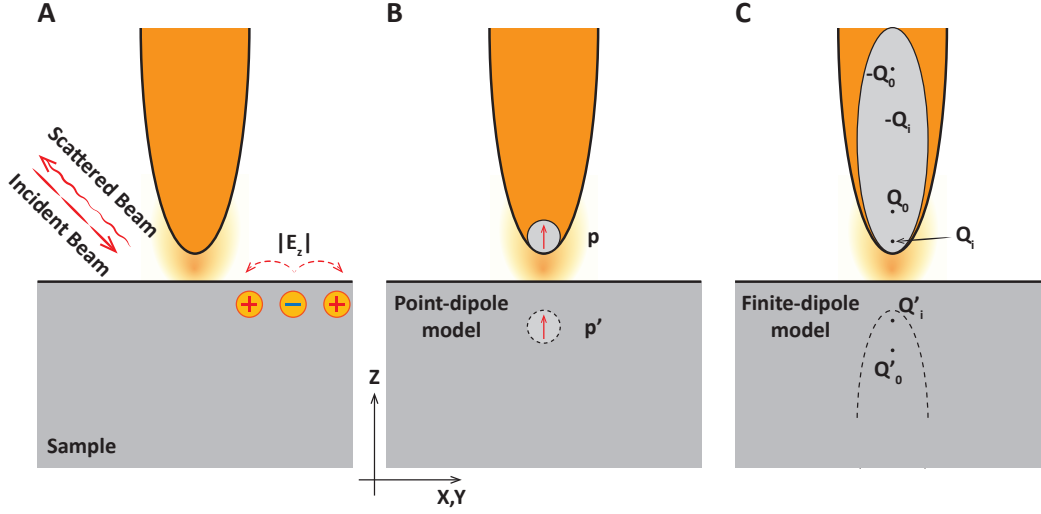
Figure 2.12: Tip-Sample Interaction Model A Sketch of a metal-coated AFM tip being illuminated. The impinging beam produces a hot spot in the tip apex enhancing the electric field E_z in the vicinity of the sample. The tip acts also as a detector scattering the near fields into the far field. The induced charges in the sample are depicted by yellow circles with '+' and '−' symbols. Red dashed lines represent the electric field induced. **B** Point dipole model. The tip is modelled as a small sphere at its apex with an electric dipole moment $\vec{p}$. A mirror dipole is induced in the sample, $\vec{p}'$ acting back in the tip dipole and so on. **C** Finite dipole model. The tip is modelled as a prolate spheroid with charges Q_0 and $-Q_0$ at the spheroid focii. As in **B**, the system induces mirror charges Q_i' which, in turn, acts back on the system.

Although this simple model was successfully used to explain the non-linear near-field optical contrast obtained between different materials, and the prediction of strong polaritonic resonances when the real part of the sample permittivity approaches -1 [**29**], it fails to reproduce the near-field obtained by performing a tip-surface approach curve (i.e., recording $|\vec{E}_z|$ as a function of tip-sample distance z), and the spectral position of the resonance, among others [**92, 102**]. The reason behind these discrepancies is attributed to an underestimation of the lightning rod effect at the tip apex. Therefore, another model was developed to depict the AFM tip more accurately. In particular, the finite-dipole model describes the AFM tip as an elongated spheroid instead of a point dipole (**Figure 2.12C**), where only charges located near the lower vertex of the spheroid (with a total length less than the incident illumination wavelength) are taken into account for the near-field interaction. Within this approximation, it is possible to find an analytical approach that quantitatively describes the non-linear near-fields produced by the tip-sample interaction.

Apart from the near-fields scattered by the tip, E^{NF}, there exist also background signals, E^b, which strongly affect the measurement and, in fact, their total contribution can be even higher. However, the background field varies in 'z' at incident wavelength λ_0 scales, therefore, variations in the detected signal due to vertical movement of the tip (typically less than $100\,nm$ and much smaller than λ_0) will come from

the pure near-field signal. Hence, demodulation of the signal at higher harmonics of the tip vibration frequency Ω seems to be a feasible option to enhance the near-field contribution over the scattered background:

$$E^{NF} = \sum_{n=0}^{\infty} E_n^{NF} e^{in\Omega t} \tag{2.16}$$

$$E^b = \sum_{n=0}^{\infty} E_n^b e^{in\Omega t} \tag{2.17}$$

However, the scattered signal is proportional to $|E^{Scattered}|^2 = |E^{NF} + E^b|^2$ and even at large n, products between the near-field signal and the background will be measured. Consequently, an additional approach is necessary to suppress the background contribution.

Interferometric detection was proposed and confirmed as a suitable technique to overcome this problem. First, a 'heterodyne' interferometric detection scheme was introduced [88] to successfully suppress the background contribution. Subsequently, it was upgraded to a 'pseudo-heterodyne' configuration due to its simplicity and better applicability to the system (**Figure 2.13A**). The 'pseudo-heterodyne' detection technique is based on a Michelson interferometer, in which the interference from a phase-modulated reference beam and the scattered wave are led to the detector and demodulated at the higher harmonics of the AFM tip resonance frequency, providing complete background-free information on the amplitude and phase of the near-field signal [91]. The piezoelectric actuator, which sinusoidally controls the motion of the reference beam, is set to a frequency, $M = 400\,Hz$, which is much smaller than the resonance frequency of the tip. Mathematically, the electric field of the reference beam, E^R, can be also Fourier expanded:

$$E^R = \sum_{n=0}^{\infty} \rho_m e^{imMt} \tag{2.18}$$

Where ρ_m is the Fourier series coefficient for the m-th component. Therefore, the total detected signal $E^{Total} = E^{Scattered} + E^R = E^R + E^b + E^{NF}$ will present sidebands $\nu_{n,m} = n\Omega + mM$ around the harmonics of the tip resonance frequency. At these sideband frequencies (**Figure 2.13B**), the background signal is fully removed [93].

By selecting a modulation amplitude of approximately $0.21\lambda_0$ with λ_0 the illumination wavelength, the n-th harmonic near-field electric field, E_n, can be fully recovered from the output voltage, u, produced at the detector. If we call $u_{n,j}$ the voltage measured at an n-th harmonic and j-th maximum of the sideband, then the near-field electric field turns out to be proportional to the output voltage $E_n \propto (u_{n,2} + iu_{n,1})$. [91]. Thus, the background-free near-field amplitude and phase of the n-th harmonic are obtained by taking the real and imaginary part of E_n, respectively.

Experimentally, harmonic resonant frequencies of the tip are easily detected using a lock-in system. For the infrared regime, the third harmonic is often used to completely suppress the background contribution and measure the pure near-field signal [93].
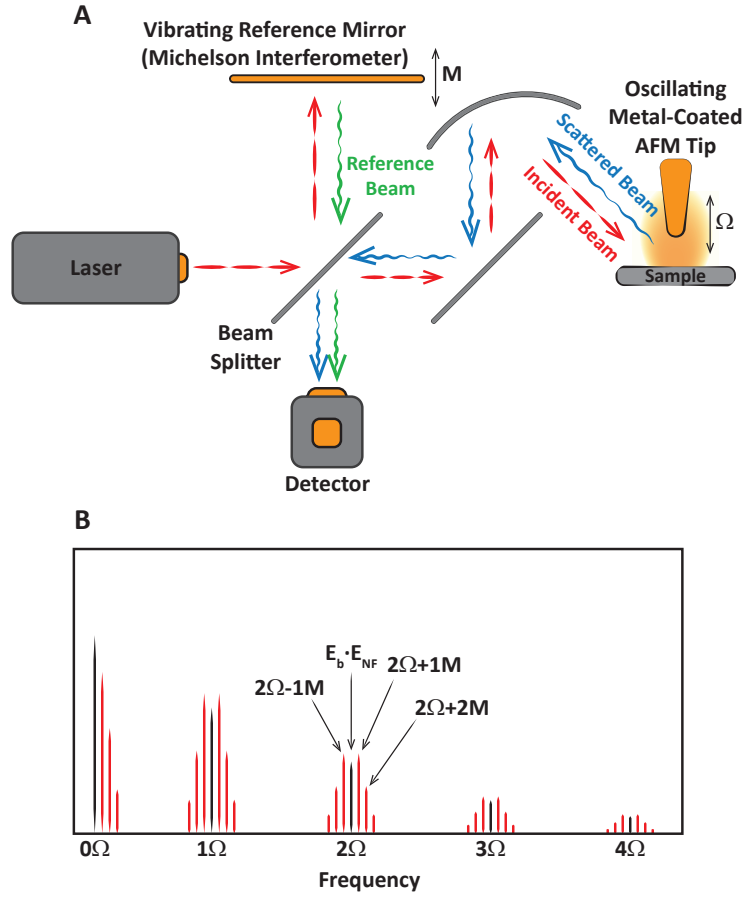
Figure 2.13: Interferometric Detection **A** Scheme of the pseudo-heterodyne configuration employed in our s-SNOM system. The incident light is splitted into two beams by a beam-splitter. The reflected beam by the reference mirror, E^R, and the beam scattered by the AFM tip, $E^b + E^{NF}$, are paired again at the beam splitter which, in turn, brings them to the MCT detector. **B** Schematic of the sideband maxima in the vicinity of the harmonic frequencies of the resonantly oscillating AFM tip. The black maxima $m = 0$ still present background contribution. Reproduced from [**93**].

Fourier Transform Infrared NanoSpectroscopy (nanoFTIR)

Fourier transform infrared nanospectroscopy (nanoFTIR) is a spectroscopic technique based on an s-SNOM system. It takes advantage of its wavelength-independent spatial resolution to obtain nanoscale resolved absorption spectra of samples. As a difference to the original s-SNOM configuration presented above, the nanoFTIR system employs an asymmetric Michelson interferometer and supercontinuum coherent infrared laser as the light source, i.e., a difference frequency generator (DFG) laser. In contrast to the single wavelength s-SNOM system presented above, the Michelson interferometer in nanoFTIR does not oscillate sinusoidally, but moves linearly up to $1500\,\mu m$ with high accuracy. In the commercial s-SNOM system used in this thesis for nanoFTIR measurements (carried out in the Nanooptics group led by Prof. Rainer Hillenbrand ata CIC nanoGUNE), the nanoFTIR module is placed on the right hand side of the apparatus (see **Figure 2.14**).

As in the normal s-SNOM configuration, the vertical oscillation of the tip allows
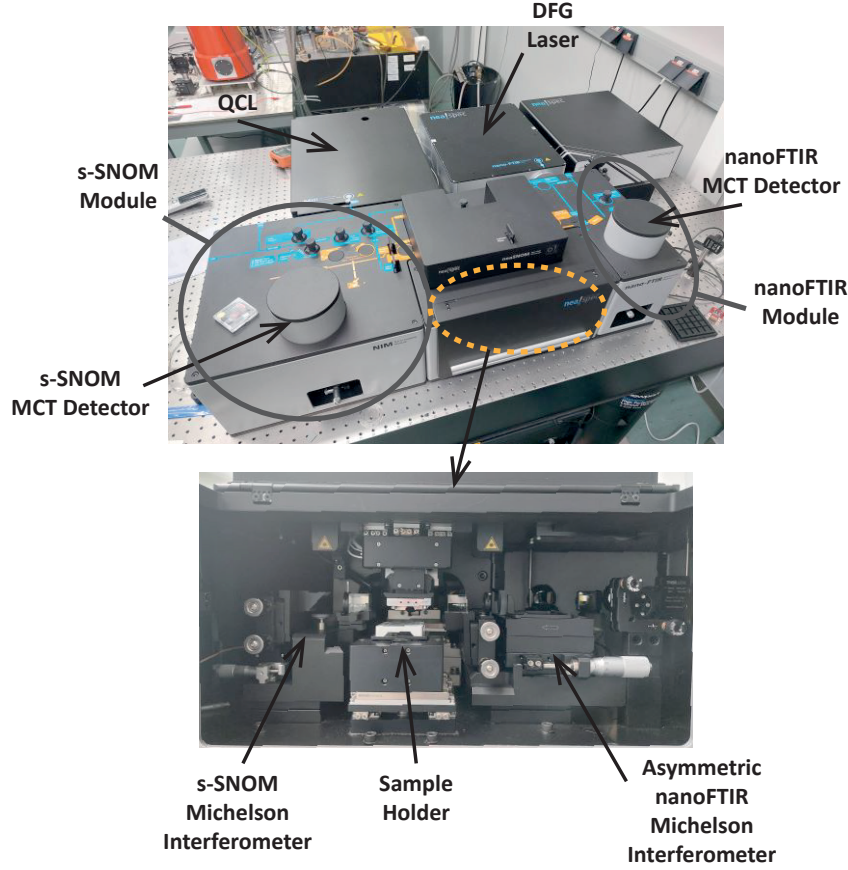
Figure 2.14: nanoFTIR System Images of the nanoFTIR system at CIC nanoGUNE (San Sebastián, Spain) employed during this thesis. Top image shows the current commercially available s-SNOM system (neaSNOM) with both s-SNOM module (left circle) and nanoFTIR module (right circle). Bottom image shows a zoom-in of the microscope, presenting both the Michelson interferometer (left part) for the s-SNOM configuration and the asymmetric Michelson interferometric (right part) for the nanoFTIR measurements.

us to demodulate the signal (in this case, the interferogram) into background-free higher harmonics [123]. The near-field spectrum is obtained by Fourier transforming the n-th interferogram. However, pure information about the near-field interferogram is not obtained directly, since the measurement is affected by instrumental characteristics: $E_n(\omega) = \sigma_n(\omega)F(\omega)E_i(\omega)$ with $E_n(\omega)$ the scattered near-field, $\sigma_n(\omega)$ the scattering near-field coefficient, $E_i(\omega)$ the incident field and $F(\omega)$ the set-up response function [124]. Therefore, to remove instrumental characteristics from the measured signal, normalization is needed. Silicon or gold are frequently used as normalization substrates, since their near-field response is flat in the MIR regime. Materials with absorption mechanism or other kind of resonances in the MIR regime are not suitable as normalization references. It should be noted that in order to perform effective normalization, the reference spectra and near-field spectra of the sample must be taken with the same system settings, i.e., same tip, tapping amplitude, optical alignment, etc. Therefore, the normalized spectra $\eta_n(\omega)$ will take the form:

$$\eta_n(\omega) = \frac{E_n^{sample}(\omega)}{E_n^{reference}(\omega)} = \frac{\sigma_n^{sample}(\omega)F(\omega)E_i(\omega)}{\sigma_n^{reference}(\omega)F(\omega)E_i(\omega)} \propto \sigma_n^{sample}(\omega) \qquad (2.19)$$

Where we have considered for the last step that the near-field scattering coefficient of the reference $\sigma_n^{reference}(\omega)$ is constant over the MIR regime. Hereafter, this normalized near-field spectra will be referred to simply as nanoFTIR spectra. Consequently, near-field nanoFTIR spectra will take the form $\eta_n(\omega) = s_n(\omega)e^{i\phi_n(\omega)}$ with $s_n(\omega) = s_n^{sample}(\omega)/s_n^{reference}(\omega)$ the amplitude and $\phi_n(\omega) = \phi_n^{sample}(\omega) - \phi_n^{reference}(\omega)$ the phase.

Analogous to FTIR, zero-filling, apodization and averaging techniques are used to improve the quality of nanoFTIR measurements in the same way as they are applied in far-field FTIR measurements.

2.4 | Finite Element Method (FEM) Simulations: COMSOL

As a means of validating the experimental data presented in this thesis, full-wave simulations of near-field phenomena were also performed. It is common in physics to deal with problems expressed in terms of partial differential equations (PDEs), even though they can only be solved in a few simple cases. PDEs are differential equations that describe the changes of a system in more than one independent variable. Nowadays, thanks to the rapid development of computational engineering, it is possible to model these non-trivial problems and find highly accurate numerical solutions by performing intelligent approximations. The set of approximations performed to estimate PDEs is called the finite element method (FEM).

In FEM simulations, the space is discretized into not necessarily uniform subregions representing the different components of the simulated system. Each subregion may have its own mesh and may be linked by boundary conditions at their interfaces. In general, the denser the mesh, the closer the numerical solution will be to the real problem and the longer the computation time.

In our particular case, we are dealing with electromagnetic waves, and therefore, our system is fundamentally described by Maxwell's equations:

$$\nabla \times \vec{B} = \mu_0 \vec{J} + \mu_o \varepsilon_0 \frac{\partial \vec{E}}{\partial t} \tag{2.20}$$

$$\nabla \times \vec{E} = -\frac{\partial \vec{B}}{\partial t} \tag{2.21}$$

$$\nabla \cdot \vec{E} = \frac{\rho}{\varepsilon_0} \tag{2.22}$$

$$\nabla \cdot \vec{B} = 0 \tag{2.23}$$

Where $\vec{E}$ and $\vec{B}$ are the electric and magnetic fields, $\vec{J}$ is the current density in the system, t is time and μ_0 and ε_0 are the vacuum permeability and permittivity.

All simulations presented in this thesis were implemented in COMSOL Multiphysics [125]. The metal-coated AFM tip is represented as a vertical-oriented dipole. The z component of the simulated electric field, E_z, plays the role of the background-free signal detected by the MCT module. The dipole is located at a height approximately equal to the tip oscillation amplitude and the simulated E_z field distribution is also recorded at these height values.

Propagating Phonon-Polaritons in α-MoO$_3$

In this chapter, α-MoO$_3$ is presented as a van der Waals material that supports phonon-polaritons with hyperbolic and elliptic in-plane propagation. Furthermore, it is shown that the dispersion of phonon-polaritons in α-MoO$_3$ is thickness-dependent, while their lifetime does not depend upon thickness. Record-high lifetimes and deeply subdiffractional polariton wavelengths are reported, as well as exotic ray-like polariton propagation, as visualized by s-SNOM measurements and corroborated by COMSOL simulations. Finally, proof-of-concept focusing devices are demonstrated that open the door to nanoscale light steering light with unprecedented capabilities. The results showed in this chapter have been published in Ma et at. 'In-plane anisotropic and ultra-low-loss polaritons in a natural van der Waals crystal', Nature 562, 557–562 (2018) and Martín-Sánchez et al. 'Focusing of in-plane hyperbolic polaritons in van der Waals crystals with tailored infrared nanoantennas', Science Advances 7, eabj0127 (2021).

3.1 | The van der Waals crystal α-MoO$_3$

α-MoO$_3$ is a lamellar material that offers wide opportunities for all kinds of applications [126, 127]. For example, due to their cytotoxicity, α-MoO$_3$ nanoplates were shown to be potential tools for the treatment of invasive breast cancer cells [128]. In addition, its potential as a gas sensor was also reported [127]. Gases or molecules embedded in α-MoO$_3$ can reduce or oxidize the material resulting in variations in the layers conductivity that can be measured [129].

Crystal Structure

The thermodynamically stable α-MoO$_3$ phase presents an orthorhombic crystal structure with space group *Pbnm* (or *Pnma*, number 62), lattice constants $a = 3.962$ Å, $b = 13.855$ Å and $c = 3.699$ Å and four formula units per unit cell ($Z = 4$) [127]. This lamellar structure consists of planar double layers of irregular MoO$_6$ octahedra held together by vdW forces along the vertical [010] crystal direction. Inside the octahedron the interactions between the atoms are dominated by covalent and ionic bonds. The thickness of each layer is $\approx 0.7\,nm$. Along the [100] crystal direction, MoO$_6$ octahedra share oxygen corners while forming edge-sharing zig-zag

chains along the [001] crystallographic direction. Depending on the coordination, three different types of oxygen atoms are identified [126]:

- The terminal O_t which bonds exclusively to one Mo atom with a bond distance of $1.67\,\text{Å}$.

- The asymmetric O_a which bonds to two different Mo atoms with average bond distances of $1.74\,\text{Å}$ and $2.25\,\text{Å}$.

- The bridging O_s which bonds to three different Mo atoms being two of them with an average distance of $1.95\,\text{Å}$ and the other one with a length of $2.33\,\text{Å}$.

Figure 3.1 shows the crystal structure of α-MoO$_3$, together with its lattice unit cell, the MoO$_6$ octahedra and an optical image of an α-MoO$_3$ flake. As a consequence of this structural anisotropy, the optical properties are expected to be anisotropic as well.
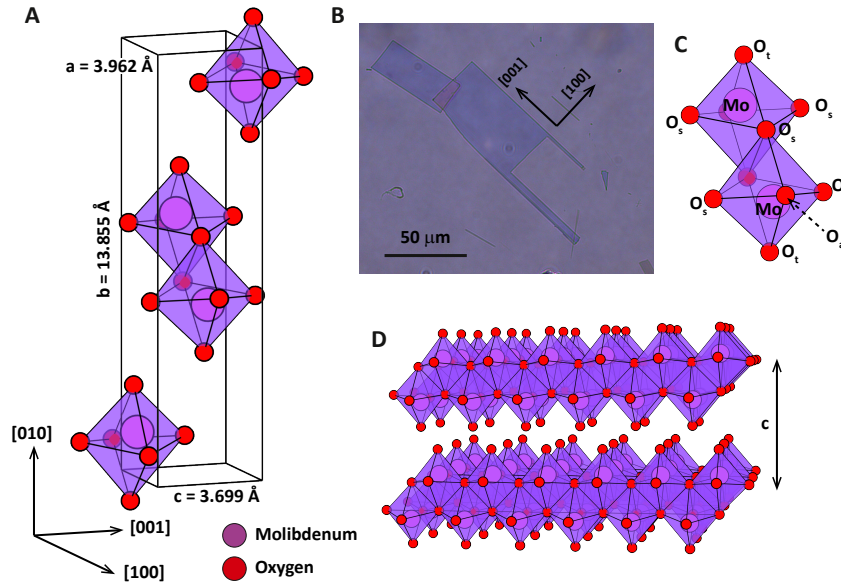
Figure 3.1: Crystal Structure of α-MoO$_3$ **A** Schematic of the unit cell of α-MoO$_3$. The unit cell consists of a periodic repetition of MoO$_6$ distorted pyramids pointing alternately up and down with the M atom (pink circles) in the center of the pyramid defined by the O atoms (red circles). **B** Optical image of α-MoO$_3$ flakes on a PDMS substrate measured in transmission mode. Due to the anisotropic crystal structure, α-MoO$_3$ exfoliates as rectangles with well-defined edges and easily recognizable crystallographic directions. **C** Schematic of the MoO$_6$ pyramids with the three non-identical oxygen atoms marked. **D** Schematic of the layered structure of α-MoO$_3$.

Far-Field Optical Characterization by FTIR

According to group theory, there are 45 optical modes at $k = 0$ for the α-MoO$_3$ *Pbnm* space group [130]:

- 17 IR active modes: $3B_{1u} + 7B_{2u} + 7\,B_{3u}$

- 24 Raman active modes: $8A_g + 8B_{1g} + 4B_{2g} + 4B_{3g}$

- 4 silent modes: $4A_u$

We are interested in the MIR active modes that present a TO-LO splitting and could give rise to the Reststrahlen Bands of α-MoO$_3$ in the MIR regime, i.e. the B_{2u} Mo-O$_t$ stretching mode defined between $\omega_{TO} = 962\,cm^{-1}$ and $\omega_{LO} = 1010\,cm^{-1}$ along the [010] crystal direction, the B_{3u} Mo-O$_a$-Mo stretching mode between $\omega_{TO} = 818\,cm^{-1}$ and $\omega_{LO} = 974\,cm^{-1}$ along the [100] crystal direction and the B_{1u} Mo$_{(3)}$-O$_s$ stretching mode defined between $\omega_{TO} = 545\,cm^{-1}$ and $\omega_{LO} = 851\,cm^{-1}$ along the [001] crystal direction [127]. It must be mentioned that, although the phonon modes of the material were studied from a fundamental point of view [131], the α-MoO$_3$ IR dielectric constant was not reported at the beginning of this thesis.

To characterize the far-field optical response of the material, we perform polarization-resolved FTIR spectroscopy on a α-MoO$_3$ flake on a BaF$_2$ substrate (BaF$_2$ is an inorganic material that does not exhibit phonon resonances or other excitations in the MIR regime, making it an ideal substrate for spectroscopic purposes in that frequency range). **Figure 3.2** shows the resulting spectra for a thick α-MoO$_3$ flake using polarized illumination along both in-plane directions ([100] and [001]). They support our previous assumption about the anisotropy of the optical properties as the optical response of the material strongly depends on light's polarization.
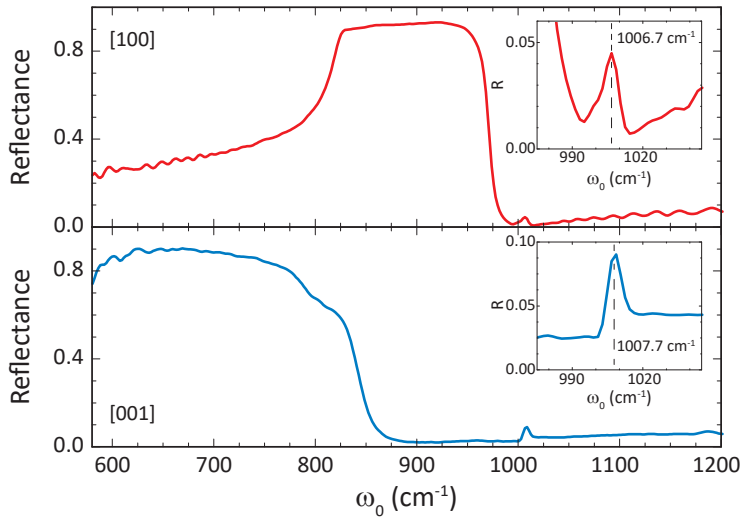
Figure 3.2: FTIR Reflectivity Measurements of α-MoO$_3$ α-MoO$_3$ reflectivity measurements taken along the [100] (upper panel, red line) and [001] (lower panel, blue line) directions. Two bands of high-reflectivity are found, one along each crystallographic direction, ranging together from $\omega_0 = 600\,cm^{-1}$ to $\omega_0 = 975\,cm^{-1}$, approximately. A peak is found along both polarizations at approximately $\omega_0 = 1007\,cm^{-1}$, which is explained by the non-normal incidence of light on the sample due to the technical configuration of the FTIR system. The position of the peak coincides with the position of ω_{LO} along the [010] crystal direction.

A broad high-reflectance band can be observed along each polarization. This band is observed approximately between $\omega_{TO} = 820\,cm^{-1}$ and $\omega_{LO} = 960\,cm^{-1}$ along the [100] direction and approximately between $\omega_{TO} = 582\,cm^{-1}$ and $\omega_{LO} = 820\,cm^{-1}$ along the [001] direction. Therefore, we can assign these high-reflectivity bands to the presence of a RB along each direction. In addition, we can observe a small peak

along both in-plane polarizations at approximately $1007\,cm^{-1}$. This is due to the presence of the B_{2u} mode that gives rise to the RB along the [010] direction. In principle, as light is polarized along the [100] or [001] directions, we should not be able to detect this resonance. However, due to the characteristics of the FTIR system, the light is not incident perpendicularly on the sample, and the wavevector k_0 of the illumination light forms a small angle of $\approx 10°$ with the vertical direction, allowing us to observe faint features from the sample vertical direction ([010] crystallographic direction).

Hence, based on these FTIR findings, i.e. the existence of RBs dependent on the incident polarization, we can expect the excitation of anisotropic phonon-polaritons in the α-MoO$_3$ MIR regime.

3.2 | Visualization of In-Plane Hyperbolic Phonon-Polaritons in α-MoO$_3$

To visualize the propagation of polaritons in α-MoO$_3$ in the different RBs, we performed polariton interferometry employing a s-SNOM system, as explained in Section 2.3. A Pt-Ir coated silicon tip is illuminated with p-polarized light. **Figure 3.3A** shows s-SNOM near-field images of a $250\,nm$-thick α-MoO$_3$ flake taken at $\omega_0 = 990\,cm^{-1}$ (within the RB arisen from the B_{2u} phonon along the [010] crystal direction) and $\omega_0 = 900\,cm^{-1}$ (within the RB arisen from the B_{3u} phonon along the [100] crystal direction) on a SiO$_2$-on-Si substrate. Unfortunately, due to technical limitations of the available lasers, we cannot perform measurements within the RB arising from the B1u phonon mode along the [001] crystal direction.

In the s-SNOM images, in-plane polaritons excited by the tip propagate along the surface of the material, get back-reflected at the flake edges, and are scattered away by the tip to the far-field. Therefore, due to interference between the incident and reflected polaritons, a standing wave is formed with a periodicity equal to half the wavelength of the polariton. In addition, polaritons can also be launched from the edges of the flake with a periodicity equal to the polariton wavelength. Both effects occur simultaneously, leading to the formation of fringe doublets, as observed in **Figure 3.3A** (characterized by a fringe of higher intensity due to edge launched polaritons and fringes of lower intensity due to tip launched polaritons) [**40, 103**].

Interestingly, at $\omega_0 = 990\,cm^{-1}$ we observe bright and dark fringes parallel to both edges of the flake with slightly different periodicity, being $\lambda_x = 950\,nm$ and $\lambda_y = 1200\,nm$ for the [100] and [001] directions, respectively. It should be noted that these values are one order the magnitude smaller than the incident wavelength ($\lambda_0 = 10.1\,\mu m$), which accounts for the highly-confined nature of PhPs in α-MoO$_3$. The anisotropy becomes even stronger at $\omega_0 = 900\,cm^{-1}$, as only fringes along the [100] direction are distinguishable.

To better understand these observations, we performed nanoFTIR line scans along the [100] and [001] crystal directions (**Figure 3.3B**). Two different spectral regions are observed along the [100] direction, which exhibit contrasting behavior. The lower region, from about $\omega_{TO} = 820\,cm^{-1}$ to $\omega_{LO} = 960\,cm^{-1}$ clearly shows a reduction of the polariton wavelength with increasing frequency. On the other hand,
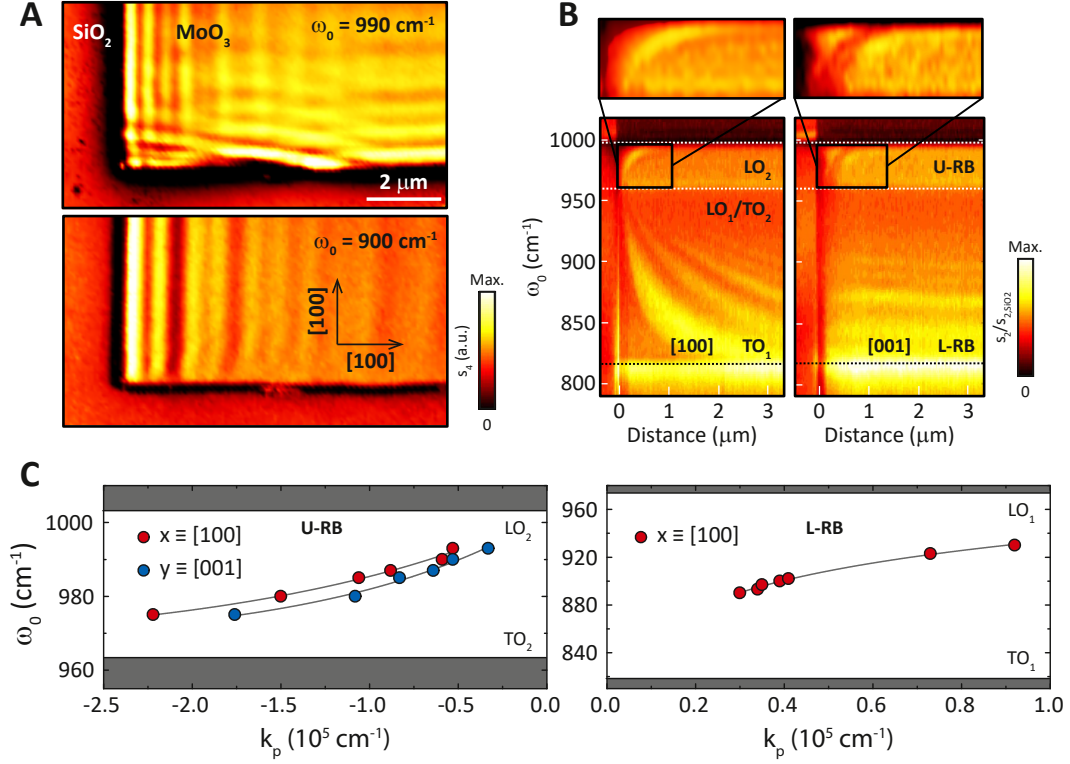
Figure 3.3: Real-Space Imaging and Nano-Spectroscopy of an α-MoO$_3$ Flake A Near-field amplitude images s_4 (fourth-harmonic) of an α-MoO$_3$ flake with thickness $d = 250\,nm$ at illuminating frequencies $\omega_0 = 990\,cm^{-1}$ (top panel) and $\omega_0 = 900\,cm^{-1}$ (bottom panel). **B** Bottom row, nano-FTIR spectral line scans along the [100] and [001] crystal directions (indicated by arrows in the bottom panel of **A**, showing the near-field amplitude s_2 (normalized to the near-field amplitude on the SiO$_2$ substrate, s_{2,SiO_2}) as a function of the distance between the tip and flake edge. Dotted lines mark the approximate longitudinal and transversal phonon modes in α-MoO$_3$ (TO$_1$, $820\,cm^{-1}$; LO$_1$/TO$_2$, $963\,cm^{-1}$; LO$_2$, $1003\,cm^{-1}$). The top row show zooms of the boxed areas in the bottom row. **C** Dispersion of PhPs along the [100] and [001] directions in the U-RB (top panel) and L-RB (bottom panel, see text). Grey lines in both panels are guides to the eye. Grey shaded areas indicate the spectral regions outside the RBs.

in the upper spectral region, from about $\omega_{TO} = 960\,cm^{-1}$ to $\omega_{LO} = 1010\,cm^{-1}$, i.e. much narrower than the lower region, the polaritons do not present as many fringes and show an increase of the polariton wavelength with increasing frequency.

These spectral regions are indeed the RBs previously shown in Section 3.1.2. Hereafter, the RB comprised between $\omega_{TO} = 962\,cm^{-1}$ and $\omega_{LO} = 1010\,cm^{-1}$ will be referred as 'upper' Reststrahlen Band (U-RB), and the region between $\omega_{TO} = 818\,cm^{-1}$ and $\omega_{LO} = 974\,cm^{-1}$ will be referred as 'lower' Reststrahlen Band (L-RB). On the other hand, the measurement along the [001] crystal direction exhibits dispersive fringes only within the upper band (with the same increase of the polariton wavelength with increasing frequency than along the [100] direction). Interestingly, the absence of fringes along the [001] crystal direction within the L-RB is a clear indication of a non polaritonic activity and, therefore, of a strongly anisotropic polaritonic nature within this spectral region.

The dispersion curves of phonon-polaritons extracted from experimental monochromatic s-SNOM images along both [100] and [001] crystal directions are shown in **Figure 3.3C**. For the U-RB, the polaritonic dispersions along both directions are slightly separated according to the aforementioned difference in the PhPs periodicity. This result corroborates that PhPs in this RB also propagate anisotropically. For the L-RB, only data along the [100] direction is displayed as there is no propagating polaritons along the [001] direction. Note that in the U-RB a large wavevector value, i.e. a short wavelength, is revealed with respect to the L-RB. Remarkably, and following previous observations from nanoFTIR measurements, PhPs in the U-RB propagate with a different slope than in the L-RB. This effect derives from the concept of phase velocity, which is explained below. The phase velocity is defined as the ratio of the angular frequency of a wave to its wavenumber at that frequency, $v_{ph,i} = \omega_0/k_i$ along the direction $i = x, y, z$, and represents the velocity at which any component of the wave travels (e.g. a maximum). On the other hand, group velocity is defined as the velocity at which the envelope of a wave travels, $\vec{v}_g = \nabla_{\vec{k}}\omega_0(\vec{k})$, and represents the velocity at which the energy stored in the wave travels. Indeed, the phase velocity points along the direction of the wavevector $\vec{k}$ while the group velocity points along the direction of the Poynting vector $\vec{S}$. A positive group velocity must be expected in both regimes, i.e. polaritonic propagation collinear to the flow of light (parallel to the Poynting vector), otherwise it would imply backward propagation of polaritons, or in other words, a violation of the causality principle. Therefore, a positive slope of the polaritonic dispersion has to be present in both regimes and, consequently, negative values for the polaritonic wavenumber $|\vec{k}_p|$ are expected. By plotting the complex-valued s-SNOM signal we can discern the nature of this effect [70]. **Figure 3.4** shows the imaginary part of the s-SNOM signal as a function of its real part at $\omega_0 = 990\, cm^{-1}$ (upper band) and $\omega_0 = 900\, cm^{-1}$ (lower band). As demonstrated in [70] for this type of graphs, a clockwise rotating spiral is considered a negative phase velocity propagation, while counterclockwise spirals are related to a positive phase velocity propagation. Indeed, we observe a clockwise behavior in the U-RB, while in the L-RB the spiral displays a counter-clockwise rotation. This further verifies that in the U-RB the polaritonic wavevector takes negative values (antiphase) along both in-plane directions, while in the L-RB the polaritonic wavevector takes positive values. Negative phase velocity of phonon-polaritons was also found in the so-called type-I Reststrahlen Band of h-BN [70].

All-Angle Polariton Interferometry

To better visualize the in-plane anisotropic propagation of PhPs in α-MoO$_3$, we fabricated a disk on a $144\, nm$-thick α-MoO$_3$ flake on a SiO$_2$/Si substrate and performed s-SNOM polaritonic interferometry measurements on it. As the disk has any curvature in the plane, we can probe the propagation of the PhPs reflected from it along any direction in the plane. **Figure 3.5A, B** show the s-SNOM near-field images measured in the U-RB (at $\omega_0 = 983\, cm^{-1}$) and L-RB (at $\omega_0 = 893\, cm^{-1}$), respectively. In the U-RB, the interference pattern shows an elliptical shape with its longest PhP wavelength along the [001] crystal direction, which continuously reduces to its smallest value along the [100] crystal direction. Interestingly, in the L-RB, the interference pattern presents convex wavefronts with the longest wavelength along the [100] crystal direction, which continuously reduces to zero along the [001] crystal direction, as there is no appreciable propagation of polaritons.
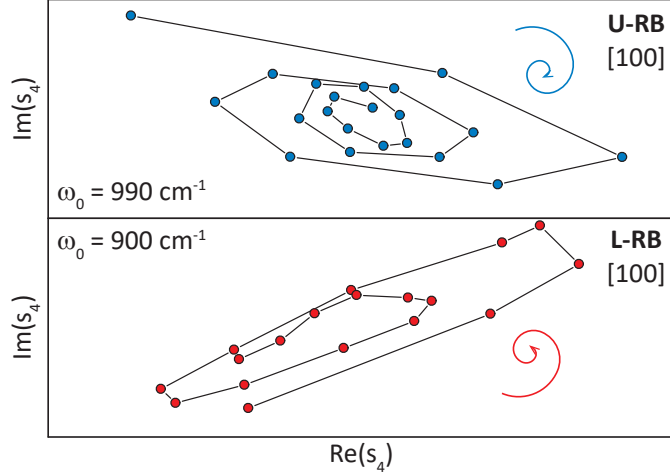
Figure 3.4: Phase Velocity of PhPs in α-MoO$_3$ Plots of the imaginary part of the complex-valued s-SNOM signal as a function of the real part of the signal in both U-RB (upper panel, blue dots, $\omega_0 = 990\,cm^{-1}$) and L-RB (lower panel, red circles, $\omega_0 = 900\,cm^{-1}$). The clockwise spiral is an indicator of the negative sign of the phase velocity in the upper band, whereas counter-clockwise spirals are an indication of positive phase velocity.

To obtain the in-plane isofrequency curves (IFC, a slice of the polariton dispersion in the momentum-frequency space defined by a plane of constant frequency, ω_0), we perform the Fourier transform of the experimental s-SNOM images (**Figure 3.5C, D**). In the U-RB, an ellipsoid is found with the largest wavevector along the [100] direction. Therefore, the upper RB is also termed as 'elliptic' band. On the other hand, a hyperbola is revealed in the L-RB with well-defined polariton wavevector along the [100] direction but forbidden propagation along the [001] crystalline direction. In the following, the term 'hyperbolic' band will be also used to refer the L-RB. Thus, the U-RB exhibit in-plane propagation of elliptic PhPs, while the L-RB presents in-plane hyperbolic propagation of PhPs. Note that for the U-RB the IFC presents two different ellipses, with the wavevector values of the larger ellipse being doubled with respect to the smaller ellipse. This result is attributed to the contribution of both tip and edge polariton excitation in the α-MoO$_3$ disk.

Our experimental results are eventually dictated by the anisotropy of the dielectric permittivity. Hence, a complete understanding of the in-plane propagation of PhPs in α-MoO$_3$ relies on the estimation of the (unknown) permittivity of this vdW crystal. To extract the anisotropic permittivity of α-MoO$_3$ in the MIR regime, we model the α-MoO$_3$ flake as a 2D conductive layer of zero thickness placed on the plane $z = 0$ [**41**]:

$$\hat{\sigma} = \begin{pmatrix} \sigma_{xx} & 0 \\ 0 & \sigma_{yy} \end{pmatrix} \tag{3.1}$$

Where σ_x and σ_y denote the α-MoO$_3$ conductivity along the 'x' ([100]) and y' ([001]) directions. Expressing the fields above ($z > 0$) and below ($z < 0$) the layer and applying the boundary conditions for the electric and magnetic fields (namely, the tangential, or in-plane, component of the electric field is continuous across the interface, $\vec{E}_{1,t} = \vec{E}_{2,t}$, and the tangential component of the magnetic field strength
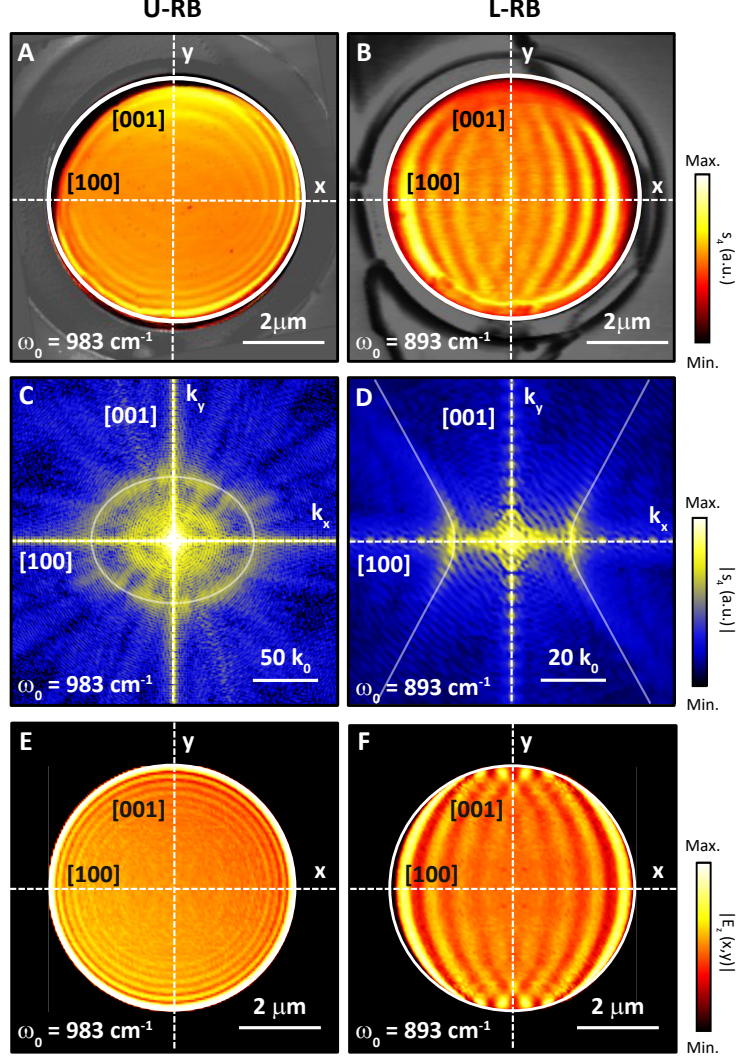
Figure 3.5: In-Plane Elliptical and Hyperbolic PhPs in an α-MoO$_3$ Disk
A, **B** Near-field amplitude images s_4 of an α-MoO$_3$ disk with a thickness $d = 144\,nm$. The imaging frequencies are $\omega_0 = 983\,cm^{-1}$ (U-RB; **A**), and $893\,cm^{-1}$ (L-RB; **B**). Dashed white lines indicate the [100] and [001] crystal directions. **C**, **D** Absolute value of the Fourier transform $|s_4(k_x, k_y)|$ of the near-field images in **A** and **B**, respectively, revealing the iso-frequency curves (IFCs) for each RB. Solid white lines show the IFCs of the PhPs obtained by fitting **Equation 3.2** for each case. Scale bars are $50k_0$ and $20k_0$, for the U-RB and L-RB respectively, with k_0 being the momentum of light in free space. **E**, **F** Calculated near-field amplitude images $|E_z(x, y)|$ for an α-MoO$_3$ disk at $\sigma_0 = 983\,cm^{-1}$ (U-RB; **E**) and $893\,cm^{-1}$ (L-RB; **F**).

obeys the relation $\vec{e}_z \times (\vec{H}_1 - \vec{H}_2) = 2\hat{\alpha}\vec{E}_{1,t}$, with $\vec{e}_z$ a unitary vector along the z direction and $\hat{\alpha} = 2\pi\hat{\sigma}/c$ a normalized conductivity tensor), we find the following expression for the dispersion relation of polaritons in a 2D anisotropic layer placed at $z = 0$ and embedded between two isotropic media with permittivities ε_1 (for $z > 0$) and ε_2 (for $z < 0$):

$$\left[k_x^2 \alpha_{xx} + k_y^2 \alpha_{yy} + \frac{k_0 k_t^2}{2}\left(\frac{\varepsilon_1}{k_{z1}} + \frac{\varepsilon_2}{k_{z2}}\right)\right]\left[k_y^2 \alpha_{xx} + k_x^2 \alpha_{yy} + \frac{k_t^2}{2k_0}(k_{z1} + k_{z2})\right] - $$
$$- k_x^2 k_y^2 (\alpha_{xx} - \alpha_{yy})^2 = 0 \tag{3.2}$$

Where $k_0 = \omega_0/c = 2\pi/\lambda_0$ is the wavevector of light in free space, $k_t^2 = k_x^2 + k_y^2$ is the in-plane polaritonic wavevector, $k_{z1,2} = \sqrt{\varepsilon_{1,2} k_0^2 - k_x^2 - k_y^2}$ is the out-of-plane polaritonic wavevector, and $\varepsilon_{1,2}$ is the permittivity of the substrate/superstrate (in this case, air and silicon oxide). Employing the last equation with α_x and α_y as fitting parameters and neglecting absorption, we find for the U-RB ($\omega_0 = 983\,cm^{-1}$) $\alpha_x = -0.12i$ ($\varepsilon_x = 2.6$) and $\alpha_y = -0.16i$ ($\varepsilon_y = 3.7$) , while for the U-RB ($\omega_0 = 893\,cm^{-1}$) we find $\alpha_x = 0.26i$ ($\varepsilon_x = -6.4$) and $\alpha_y = -0.07i$ ($\varepsilon_y = 1.7$). To extract the material permittivity from these values, we need to recover the thickness dependence of the conductivity tensor. Conductivity and permittivity are related through $\hat{\sigma} = (cd/2i\lambda_0)\hat{\varepsilon}$ [41]. Hence, for polariton propagation to occur, we must have positive values of α in the U-RB along both directions, since negative ε is a requirement for polariton excitation. Note that although with our model we cannot extract the permittivity value for the out-of-plane [010] crystalline direction, we can infer its sign as follows. A negative in-plane permittivity component and a positive out-of-plane permittivity component would lead to a positive polaritonic phase velocity, which would contradict the experimental negative phase velocity found previously in this regime. Consequently, for the upper RB to have a negative phase velocity, the in-plane components of the permittivity must be positive and the out-of-plane component negative, i.e. negative α values in the plane and positive α values out of the plane. Besides, in the lower RB the α values extracted are fully consistent with a positive phase velocity of polaritons along the [100] crystal direction (we found a negative permittivity along the [100] crystal direction and a positive permittivity along the [001] crystal direction) considering a positive permittivity along the [010] crystal direction. The images simulated by FEM are shown in Figure **Figure 3.5E, F**. Both the shape of the polaritonic pattern and the simulated wavelength match the experimental results. Consequently, our simple model for an anisotropic polariton dispersion allows us to extract the permittivity values of the in-plane components and the sign of the out-of-plane component for highly anisotropic materials by means of PhPs interferometry measurements and fittings of the IFC. In fact, these extracted permittivity values are consistent with the correlative near- and far-field studies performed to extract the MIR permittivity of α-MoO$_3$ along the three crystallographic axes performed subsequently [132].

Although we have modelled the α-MoO$_3$ flake as a 2D conducting layer embedded between two media, the dispersion depends on the thickness of the flake as mentioned above. Let us find the thickness dependence of the dispersion relation (**Eq. 3.2**) in the case of polariton propagation along the [100] axis. Assuming $k_y = 0$, **Equation 3.2** transforms into the product of two factors. If we further assume that the polariton momentum is much larger than the momentum of light, $k_x \gg k_0$, we can approximate $k_{zi} = \sqrt{\varepsilon_i k_0 - k_x^2 - k_y^2} \approx \pm i k_x$, becoming:

$$k_x \approx -\frac{\varepsilon_1 + \varepsilon_2}{2i\alpha_{xx}} k_0 = -\frac{\varepsilon_1 + \varepsilon_2}{d\varepsilon_{xx}} \tag{3.3}$$

Therefore, the polariton wavevector depends approximately only on the permittivity of the substrate, superstrate and material along the studied crystal direction,

as well as on its thickness. **Figure 3.6A** shows the in-plane hyperbolic PhPs thickness tuning in α-MoO$_3$. Monochromatic s-SNOM images were taken to extract the dispersion of PhPs from four different flakes with thicknesses of about $250\,nm$, $130\,nm$, $80\,nm$ and $55\,nm$. It is clearly observed that the wavevector of the polaritons increases with decreasing thickness and, therefore, the lower the thickness, the higher the polariton confinement. For example, at an illuminating wavelength of $\lambda_0 = 10.8\,\mu m$ ($\omega_0 = 926\,cm^{-1}$), we find for a $55\,nm$ thick flake a polariton wavelength of $\lambda_x = 180\,nm$, which is about 60 times smaller. In addition, we have plotted the experimentally extracted wavevector values for these four thicknesses at $\omega_0 = 902\,cm^{-1}$ to represent the inverse dependence of k_x on thickness (**Figure 3.6B**). The experimental points fit well with our theoretical equation, where a value of $\varepsilon_x = -5.1$ was employed (extracted from the $144\,nm$-thick α-MoO$_3$ disk using **Equation 3.2**), thus supporting the validity of our model.
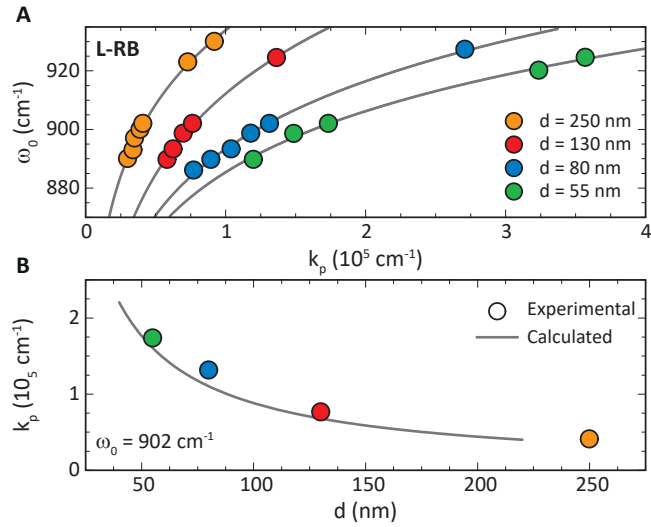
Figure 3.6: Thickness Tunability of In-Plane Hyperbolic and Elliptic PhPs in α-MoO$_3$ A Experimental (dots) PhPs dispersions along the [100] direction in α-MoO$_3$ for a varying flake thickness d (lines are guides to the eyes). **B** Experimental (dots) and calculated (line) dependence of k_p upon d.

Direct Visualization of Propagating Hyperbolic Phonon-Polaritons in α-MoO$_3$

Another solution to confine light into nanometer volumes and excite polaritons by overcoming the momentum mismatch is to employ metallic optical nanoantennas [15], which, when illuminated, produce near-field plasmonic modes that enhance the electric field [133, 134, 135]. These plasmonic modes can be tuned either by changing the illuminating frequency or the nanoantenna length [136], which is typically designed to excite the fundamental mode due to its superior field enhancement. In the case of using rod-shaped metallic nanoantennas, in-plane dipolar moments exhibiting near-fields with opposite polarities at the rod extremities are formed [66].

Following this technological strategy to launch polaritons, we fabricated a gold rod-shaped nanoantenna (with a length of $3.5\,\mu m$, a width of $0.22\,\mu m$, and a height of $0.032\,\mu m$) on top of a $225\,nm$-thick α-MoO$_3$ flake with its long axis aligned along the
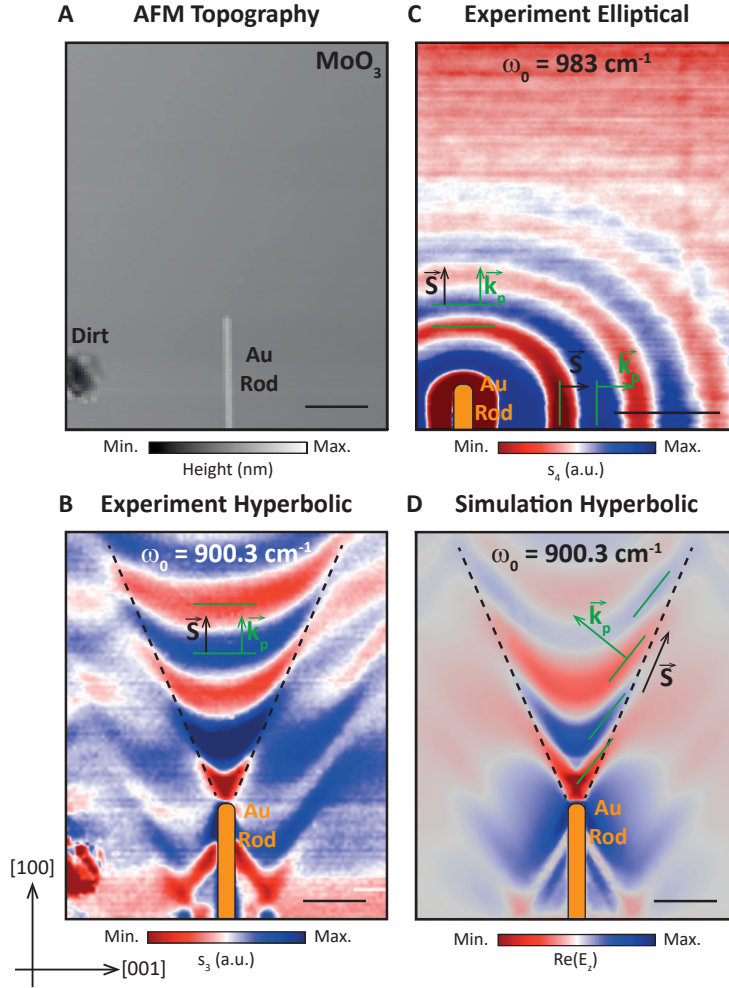
Figure 3.7: Visualization of In-Plane Hyperbolic Polaritons in α-MoO$_3$
A AFM topographic image of the Au nanoantenna (light grey vertical line at the bottom) fabricated on a $225\,nm$-thick α-MoO$_3$ by standard lithographic processes. **B** Amplitude s-SNOM s_3 image taken at $\omega_0 = 900.3\,cm^{-1}$ (hyperbolic L-RB) in the same region as shown in **A**. For a better visualization of PhPs, the color scale has been saturated. Black dashed lines indicate the asymptotes of the hyperbola and the angular section where there is polaritonic propagation. The PhPs wavefronts along the [100] crystal direction are indicated by green horizontal lines. The PhP wavevector $\vec{k}_p$ and Poynting vector $\vec{S}$ are collinear and perpendicular to these lines along this direction. **C** Amplitude s-SNOM s_4 image taken at $\omega_0 = 983\,cm^{-1}$ (elliptic U-RB) in the same region as shown in **A**. PhPs propagate along all directions. **D** COMSOL simulation showing the real part of the electric field vertical component $\mathfrak{Re}(E_z)$ obtained by mimicking the experiment in **B**. The α-MoO$_3$ flake was modelled as a 2D conductivity layer in accordance with **Equation 3.2**. Black dashed lines indicate the directions of the asymptotes of the hyperbola. Green lines are depicted to show the polaritonic wavefronts along propagation directions close to the asymptotes. The PhP wavevector $\vec{k}_p$ and the PhP Poynting vector $\vec{S}$ are almost perpendicular.

[100] crystal direction. Details about the antenna fabrication can be found in references [66, 104]. **Figure 3.7A** shows an AFM topography image of the sample with the nanoantenna. Upon illumination (**Figure 3.7B, C**), near-field amplitude fringes revealing the propagation of PhPs are observed in the surroundings of the antenna at

both $\omega_0 = 900.3\,cm^{-1}$ (hyperbolic L-RB, **Figure 3.7B**) and $\omega_0 = 983\,cm^{-1}$ (elliptic U-RB, **Figure 3.7C**). However, there are striking differences between both images. In the hyperbolic band, PhPs are observed only within a conical section (delimited by black dashed lines in the figure) exhibiting a convex contour with its origin at the nanoantenna extremity. On the other hand, in the elliptic band, PhPs are observed along all directions exhibiting a concave contour. To corroborate theoretically this exotic PhP behavior, a COMSOL simulation was performed in the L-RB considering α-MoO$_3$ as a 2D conductive layer in accordance with **Equation 3.2**. The calculated near-field image obtained (**Figure 3.7D**) is in excellent agreement with the experiment, reproducing all the characteristics of hyperbolic PhPs. These include a direct dependence of the wavelength as a function of the angle of propagation within the hyperbolic cone. As such, PhPs propagating along the [100] crystal direction present the longest wavelength λ_p, while PhPs propagating along the hyperbolic asymptotes present the shortest wavelength. Furthermore, PhPs propagate along the [100] crystal direction with their wavevector $\vec{k}_p$ (green arrow in **Figure 3.7B**) and the Poynting vector $\vec{S}$ (black arrow), which determines the direction at which the energy flows, pointing along the same direction, as typically observed in isotropic media. However, when approaching the asymptotes (black dashed lines in **Figure 3.7D**), the wavefronts are tilted (green lines perpendicular to $\vec{k}_p$) with respect to the Poynting vector, exhibiting a clear signature of the propagation of light in strongly anisotropic media [5]. Further details about launching of in-plane hyperbolic PhPs with Au nanoantennas will be provided in Section 3.4.

3.3 | Lifetimes of In-plane Hyperbolic Phonon Polaritons in α-MoO$_3$

To further evaluate the optical properties of in-plane PhPs in α-MoO$_3$, we extracted the lifetimes, τ. Lifetime is defined as $\tau = L_p/v_g$, where L_p is the decay or propagation length defined in Chapter 1 (the length at which the polariton electric field decays by a factor $1/e$) and v_g the group velocity, representing how long the polaritons exist. As will be shown in the following subsections, the low group velocities of in-plane PhPs in α-MoO$_3$ together with their extremely long lifetimes, make them ideal candidates for light-matter applications such as ultrasensitive biosensors.

Extracting the Decay Length of PhPs in α-MoO$_3$

The decay length of PhPs is extracted by fitting s-SNOM line profiles of the PhPs amplitude to an exponentially decay sinusoidal function. Assuming both tip- and edge-launched PhPs, the fitting equation takes the form [103]:

$$\xi(x) = \xi_0 + Ae^{-x/L_p}\sin\left(\frac{2\pi(x-x_{c0})}{\lambda}\right)\frac{1}{x} + Be^{-2x/L_p}\sin\left(\frac{4\pi(x-x_{c1})}{\lambda}\right)\frac{1}{\sqrt{x}} \quad (3.4)$$

where ξ is the s-SNOM amplitude signal, ξ_0 is an offset parameter, L_p is the polariton decay length, λ is the polariton wavelength, x_{c0} and x_{c1} are offsets for the sine functions, and A and B are the edge- and tip-launched polariton amplitudes, respectively. The factors $1/x$ and $1/\sqrt{x}$ are incorporated to account for the geometrical spreading factor of edge- and tip-launched polaritons, respectively (edge launched PhPs are considered as plane waves while tip launched PhPs are considered as circular waves). Furthermore, the equation also incorporates a factor of two in both the

decay length and wavelength of tip-launched PhPs to consider their standing wave nature (note that they travel back and forth with respect to the tip). **Figure 3.8** shows a typical fitting for PhPs in α-MoO$_3$ in the U- and L-RBs along the [100] crystallographic direction.
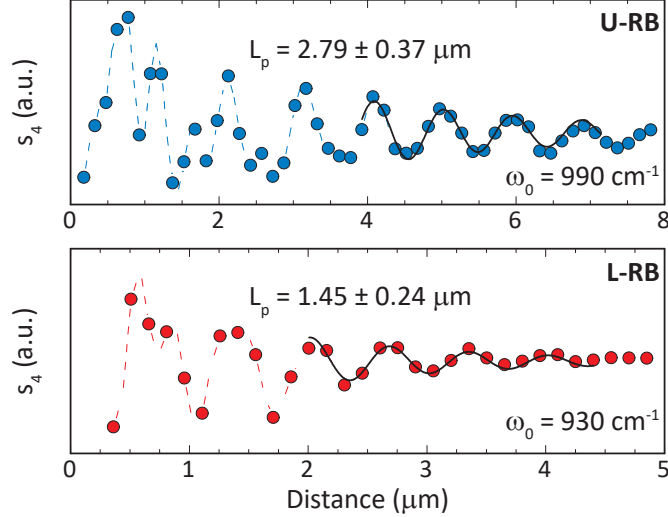
Figure 3.8: Fitting of Decay Lengths Near-field s-SNOM profiles taken along the [100] crystal direction of the flake shown in **Figure 3.3A** at $\omega_0 = 990 \, cm^{-1}$ in the U-RB (blue dots, upper panel) and $\omega_0 = 930 \, cm^{-1}$ L-RB (red dots, lower panel)

Extracting the Group Velocity of PhPs in α-MoO$_3$

The group velocity is defined by $v_{g,i} = \partial\omega_0/\partial k_i$; $i = x, y, z$. To extract the group velocity of PhPs in α-MoO$_3$, we thus perform derivatives of the experimentally extracted PhPs dispersions. In particular, we first fit the experimental dispersion curves by a generic potential function $y(x) = ax^b$, and then we perform a numerical derivative of the resulting curve. **Figure 3.9** shows the obtained group velocity (in c units, with c the spped of light) in the L-RB for flakes with different thicknesses whose dispersion is shown in **Figure 3.6**. As PhPs are more confined (lower PhP wavelengths, λ_p) for the thinner flakes, the group velocities are lower with respect to the thicker flakes. This is a direct consequence of the thickness-dependent PhPs dispersion: a 'flatter' PhP dispersion is extracted for the thinner samples (see **Figure 3.6A**), leading to lower group velocities when taking the derivative, as the slope of the curve is lower.

For the $250 \, nm$-thick flake show in **Figure 3.3**, the extracted group velocity presents a value of $v_g = 769828 \, m/s$, i.e. $2.5 \cdot 10^{-3} \, c$ (c is the speed of light), in the L-RB (at $\omega_0 = 930 cm^{-1}$). In the U-RB (at $\omega_0 = 990 \, cm^{-1}$) a value of $v_g = 347759 \, m/s$, i.e. $1.2 \cdot 10^{-3} \, c$ was obtained along the [100] crystalline direction. Note that propagating PhPs in h-BN exhibit values of the order of $10^{-2} \, c$, which is one order of magnitude higher than the values obtained in α-MoO$_3$, indicating the ultra-slow propagation of PhP in the latter.
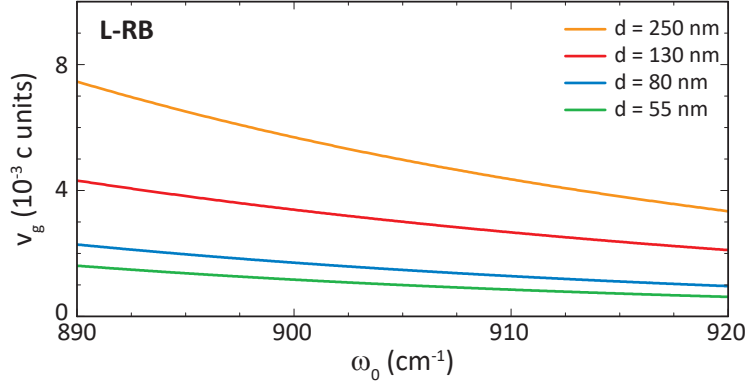
Figure 3.9: Group Velocities of PhPs in α-MoO$_3$ Group velocities, v_g, of PhPs in α-MoO$_3$ extracted by taking the numerical derivative of the fitting curves in **Figure 3.6A**.

Lifetimes of PhPs in α-MoO$_3$

As mentioned above, the PhP lifetime can be now calculated using the expression $\tau = L_p/v_g$ for both the L-RB and the U-RB. The calculated values are taken for the flake with a thickness $d = 250\,nm$ whose dispersion is shown in **Figure 3.3**. In the L-RB (hyperbolic regime), we obtain a lifetime of $\tau_{Hyper} = 1.9 \pm 0.3\,ps$ at $\omega_0 = 930\,cm^{-1}$, i.e. one order of magnitude longer that the longest plasmon-polariton lifetimes ever observed in graphene [**52**] and of the same order as the best values reported for PhPs in h-BN [**71**]. In the U-RB (elliptic regime), we obtain a lifetime of $\tau_{Ellip} = 8 \pm 1\,ps$ at $\omega_0 = 990\,cm^{-1}$, i.e. four times longer than the best values reported until now in isotopically enriched h-BN [**71**]. As such, these results clearly reveal the ultra-low-loss character of PhPs in α-MoO$_3$. Note that the RBs in α-MoO$_3$ are narrow compared to the type-II RB in h-BN, leading to much flatter dispersion relations, which in turn causes the PhPs in α-MoO$_3$ to propagate with extremely small group velocities, resulting in relatively short propagation lengths. Therefore, s-SNOM images of propagating PhPs in α-MoO$_3$ do not show as many oscillation fringes as e.g. PhPs in h-BN. Additionally, our studies reveal that the lifetimes of PhPs in α-MoO$_3$ are independent upon the flake thickness (**Figure 3.10**) [**41**, **137**].
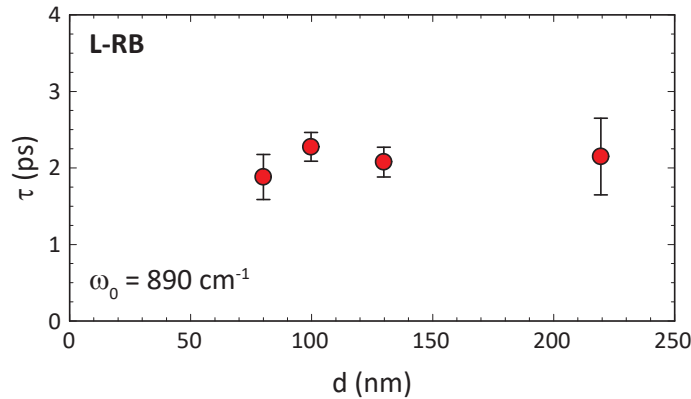
Figure 3.10: Lifetimes of PhPs in α-MoO$_3$ Lifetimes (symbols) extracted at $\omega_0 = 890\,cm^{-1}$ (hyperbolic L-RB) for four flakes with different thicknesses $d = 80$, 100, 130 and $220\,nm$. No thickness dependence is observed.

3.4 | Nano-Optics using In-Plane Hyperbolic PhPs in α-MoO$_3$

In-plane hyperbolic polaritons promise unprecedented control of light at the nanoscale in planar integrated devices, where focusing typically constitutes a basic building block for applications, such as nanoimaging, low-temperature nanophotocatalysis [138], nanobiosensing [6, 74, 139] or thermal management at the nanoscale [140]. As mentioned in Chapter 1, h-BN has proven to be a suitable platform for studying ray-like propagation of polaritons [141], hyperlensing effects [84] and focusing of polaritons [86]. However, the out-of-plane nature of PhPs in h-BN limits its practical implementation in planar integrated devices. In a recent technological attempt, h-BN slabs were patterned into stripes to form an artificial metasurface where PhPs propagate with a hyperbolic dispersion in the plane [47]. However, this technological has proven to be inefficient, as the propagation of PhPs is greatly damped due to damage induced during the fabrication process. In this sense, the ultra-low-loss nature of in-plane hyperbolic PhPs in α-MoO$_3$ offer unique opportunities as a natural platform for planar technologies in nanooptics. In this section, we will demonstrate metal nanoantennas in α-MoO$_3$ flakes as the first optical element to deeply focus PhPs at nanometer-sized focal spots with enhanced field confinement.

It is worth noting that, unlike the work on PhPs in α-MoO$_3$ shown in the previous sections, in the following sections we employ the precise dielectric function of α-MoO$_3$ over a wide frequency range covering both RBs. This is because the permittivity was extracted in parallel to this thesis work in our research group through correlative far- and near-field studies on multiple flakes of different thicknesses. Details can be found elsewhere [132]. The ε_i, $i = [100], [010], [001]$, components of the dielectric permittivity for α-MoO$_3$ along the [100], [010] and [001] crystallographic directions are plotted in **Figure 3.11** (real part) and its parameters summarized in **Table 3.1**.
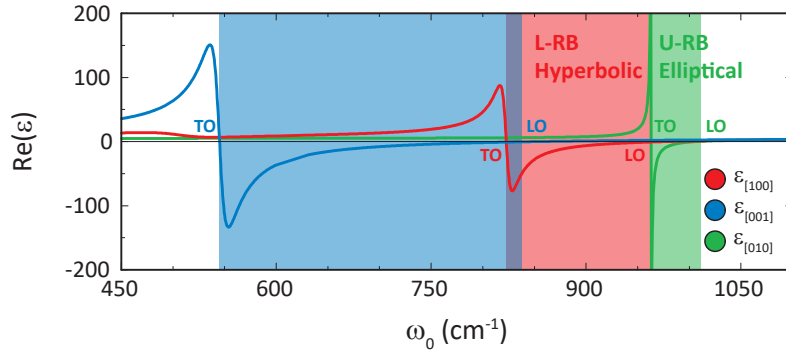
Figure 3.11: Permittivity of α-MoO$_3$ IR dielectric function of α-MoO$_3$ along the three crystallographic axes. The shaded regions indicate the three Reststrahlen bands, corresponding to phonons on each of the crystallographic axes: [001], [100], and [010]. Adapted from [132].

As clearly shown by the PhP IFC in the L-RB of α-MoO$_3$, the propagation of PhPs is allowed only along a set of directions, which defined a region given by [84, 104]:

$$|\tan(\theta(\omega_0))| < \sqrt{-\frac{\varepsilon_x(\omega_0)}{\varepsilon_y(\omega_0)}} \tag{3.5}$$

49

Crystallographic Axes	$\omega_{TO}\,(cm^{-1})$	$\omega_{LO}\,(cm^{-1})$	$\gamma\,(cm^{-1})$	ε_∞
[100]	506.7	534.3	49.1	
[100]	821.4	963.0	6.0	5.78
[100]	998.7	999.2	0.35	
[010]	956.7	1006.9	1.5	4.47
[001]	544.6	850.1	9.5	6.07

Table 3.1: Permittivity of α-MoO$_3$ Parameters for the IR dielectric function of α-MoO$_3$, extracted from correlative far- and near-field experiments. Adapted from [132].

With $\theta(\omega_0)$ the angle that forms the asymptotes of the hyperbola with the [001] axis. In the limit when $|\tan(\theta(\omega_0))| = \sqrt{-\varepsilon_x(\omega_0)/\varepsilon_y(\omega_0)}$, the relation represents the equation of the asymptotes. **Figure 3.12** shows the analytic IFC (calculated using the dispersion equation for electromagnetic modes in slabs of biaxial crystals [142]) for PhPs in a $165\,nm$-thick α-MoO$_3$ flake at an illumination wavelength of $\lambda_0 = 11.05\,\mu m$ (or $\omega_0 = 905\,cm^{-1}$). The wavevector and the Poynting vector of PhPs are also indicated in the figure for a random direction different from the [100] crystal axis showing that they are not collinear, i.e. the direction of propagation of the energy flux is not perpendicular to the wavefronts, as is the case for plane waves. This is a unique property of hyperbolic PhPs. Another was already mentioned in Chapter 1, as the asymptotes of the hyperbola are reached, the number of available PhP wavevectors increases, resulting in highly directional propagation of the PhPs.
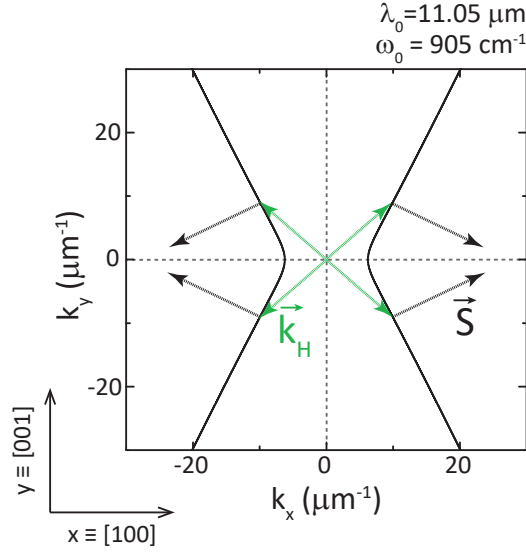
Figure 3.12: Isofrequency Curve of In-Plane Hyperbolic PhPs in α-MoO$_3$ IFC of in-plane hyperbolic PhPs in a $165\,nm$-thick α-MoO$_3$ slab at an illuminating wavelength $\lambda_0 = 11.05\,\mu m$ ($\omega_0 = 905cm^{-1}$). PhPs with high-$|\vec{k}|$ wave vectors are indicated by $\vec{k}_H$, together with their Poynting vector $\vec{S}$.

Focusing of Nanolight using in-plane hyperbolic PhPs in α-MoO$_3$

To understand the ray-like character of in-plane hyperbolic PhPs in α-MoO$_3$, we can study the near-field pattern created by a point dipole source placed above an α-MoO$_3$ flake. To do that, it is useful to use the Dyadic Green's function (DGF), $\hat{G}(\vec{r} - \vec{r}')$.

Physically, it relates the electric field created by a source (e.g. the polariton field created by a point dipole) at a point $\vec{r}$ with the initial electromagnetic field at the dipole position $\vec{r}'$, and it can be calculated according to:

$$\vec{E}(\vec{r}) = k_0^2 \int d^3\vec{r}' \hat{G}(\vec{r} - \vec{r}')\vec{E}_0(\vec{r}') \tag{3.6}$$

with $k_0 = \omega_0/c$. In addition, when Fourier transformed, $\hat{G}(\vec{k})$ describes the efficiency of excitation of an electromagnetic mode with a given wavevector/momentum $\vec{k}$ and it is also related to the density of optical states (DOS). Specifically, the dispersion relation of PhPs expressed in **Equation 3.2** can be obtained from the DGF calculating its poles. Interestingly, since the polaritonic electric fields are typically characterized by strong vertical components (z axis) , only the z component of the DGF, $\hat{G}_z$ needs to be considered. Moreover, s-polarized plane waves possess no projection on the z axis, so only the contribution due to p-polarized waves is required [104]. **Figure 3.13A** shows the calculated $\hat{G}_z(\vec{k}_x, \vec{k}_y)$ in momentum space at $\omega_0 = 905\,cm^{-1}$ for a $165\,nm$-thick flake (a vertically oriented dipole is used as PhPs excitation source), where the maxima are obtained close to the directions of the asymptotes of the hyperbolic IFC. In real space, the integrated near field along all in-plane directions yields a pattern that exhibits narrow lobes (yellow dashed lines in **Figure 3.13A, B**), which indicate the directions along which the density of propagating polaritonic modes is maximum. Hence, ray-like propagation of polaritons along the hyperbolic asymptotes is fully associated with a high density of polaritonic modes closely along the IFC asymptotes.
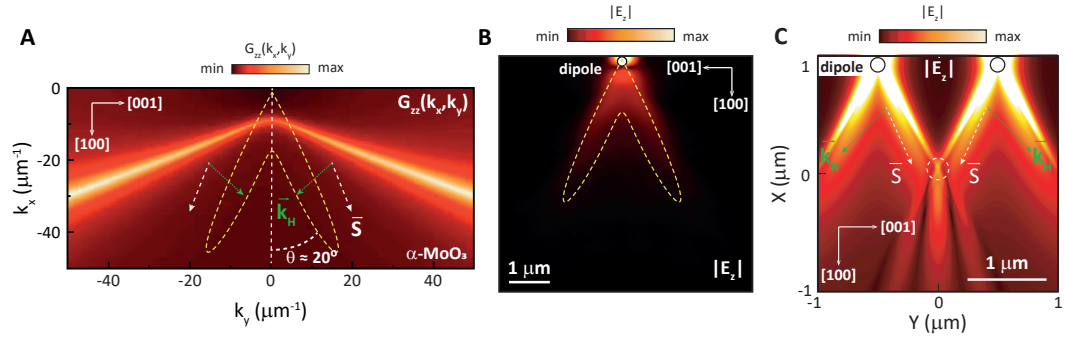
Figure 3.13: **Ray-Like In-Plane Propagation of PhPs in α-MoO$_3$** **A** Color plot: Analytical calculation of the Green's function $\hat{G}_z(\vec{k}_x, \vec{k}_y)$ in momentum $\vec{k}$-space, for a $165\,nm$-thick α-MoO$_3$ slab at $\lambda_0 = 11.05\,\mu m$. The polaritonic IFC contour is shown as maxima in the color plot. The yellow dashed line corresponds to the field intensity, absolute value of $\hat{G}(\vec{r} - \vec{r}')$ as a function of the polar angle at the distance r_0 from the dipole source. The white and green dashed arrows are the Poynting vector $\vec{S}$ and $\vec{k}_H$ wavevectors of PhPs propagating along in-plane directions closely aligned with the asymptote of the hyperbolic IFC. The near-field intensity shows a maximum DOS at an angle θ with respect to the [100] crystal direction. **B** Numerical simulation of the electric $|E_z|$ (color plot) excited by a point electric dipole placed above the α-MoO$_3$ slab together with the polar distribution of the electric field in real space (yellow dashed lines) shown in **A**. **C** Near field, $|E_z|$, calculated analytically for two vertical point dipoles on α-MoO$_3$. A focal spot is obtained upon interference of ray-like PhPs with $\vec{k}_H$ wave vectors (dashed circle).

To visualize the in-plane propagation of PhPs along the surface of α-MoO$_3$, we

have analytically calculated the near-field distribution, $E_z(x, y)$, in real space using two distant point dipoles as excitation sources (**Figure 3.13C**). In this figure, the strongly directional propagation of ray-like PhPs is clearly revealed leading to the formation of a focal spot upon their constructive interference, marked with a white dashed circle. Based on these calculations, we study the possibility of focusing in-plane PhPs by using metal nanoantennas that can be used for an efficient launching of PhPs in van der Waals materials. **Figure 3.14A** shows the real part of the z-component of the electric field, $\mathfrak{Re}(E_z(x,y))$, obtained by full-wave numerical simulations at an illumination wavelength of $\omega_0 = 905\, cm^{-1}$ for a metal disk nanoantenna placed on top of an α-MoO$_3$ slab. The PhPs launched by the Au disk present a series of convex wavefronts within a triangular region (marked by black dashed arrows) that shows a focal spot at its apex. Note that this convex antenna geometry is in stark contrast to the typical nanoantennas with a concave geometry used for focusing in-plane polaritons in isotropic media (See right inset in **Figure 3.14A**) [**15, 66**]. By taking a horizontal profile of the electric field intensity, $|E_z(x,y)|^2$, in the image (which corresponds to the [001] α-MoO$_3$ crystalline axis, marked with the red dashed line), a full width at half maximum (FWHM) of $\approx 390\, nm$ is obtained for the focal spot, which corresponds to a subwavelength size of $\approx \lambda_0/28$ (left inset of **Figure 3.14A**), being λ_0 the illuminating wavelength.

This exotic focusing effect obtained for a convex geometry of the nanoantenna can be understood by the Huygens principle in hyperbolic media. Specifically, by considering the Au disk nanoantenna as a system composed of an infinite number of point-like dipoles placed along the edge of the Au disk that emit polaritons whose wavefronts interfere. **Figure 3.14B** shows the full-wave numerical simulation where a discrete number of point dipoles are situated at the periphery of a circular contour mimicking the disk nanoantenna. Contrary to the case of isotropic media where the energy flows equally in all in-plane directions (**Figure 3.14C**), and, therefore, a parallel wavefront to the nanoantenna edge is obtained, in hyperbolic media, the interference of propagating ray-like polaritons with high-$\vec{k}$ ($\vec{k}_H$) leads to the formation of a focal spot. Interestingly, the result obtained closely reproduces the image obtained when a complete Au disk nanoantenna is used (**Figure 3.14A**), thus confirming that the formation of the peculiar convex fringes are due to the interference of polaritons with high k ($\vec{k}_H$) launched by the edge of the nanoantenna.

To experimentally demonstrate these theoretical results, we fabricated an Au disk nanoantenna on top of a $165\, nm$-thick α-MoO$_3$ flake and performed s-SNOM polariton nanoimaging at different incidence wavelengths λ_0. **Figure 3.15** shows the images obtained at $\lambda_0 = 10.70$, 10.85 and $11.05\, \mu m$ (corresponding to $\omega_0 = 934.6$, 921.6 and $905 cm^{-1}$, respectively). All experimental images (top row in the figure) display the convex wavefront effect emerging from the Au nanoantenna predicted by the simulations, with the eventual formation of a focal spot. Full-wave numerical simulations fully reproduce these experimental results (bottom row in the figure). Interestingly, we observe that by increasing λ_0 (decreasing ω_0) both the width of the focal spot and the focal distance (f, defined as the distance measured from the focal spot to the nanoantenna edge along a perpendicular line, white vertical line in top-right image) vary. In particular, f takes values that range from $\approx 0.6\, \mu m$ at $\lambda_0 = 10.70\, \mu m$ up to $\approx 1.7\, \mu m$ at $\lambda_0 = 11.05\, \mu m$. On the other hand, the spot sizes (extracted by taking profiles along the horizontal direction, corresponding to the α-MoO$_3$ [001] crystal direction, as indicated by arrows in the experimental images)
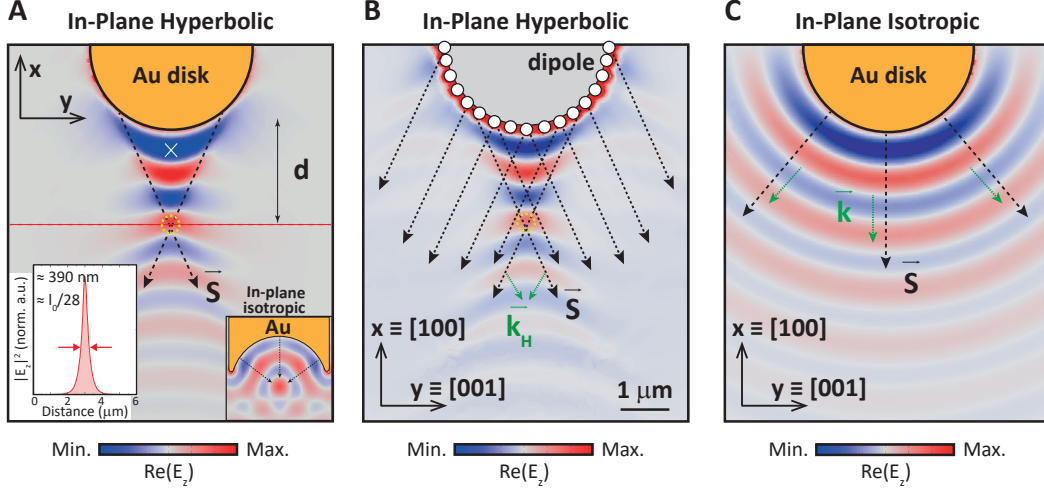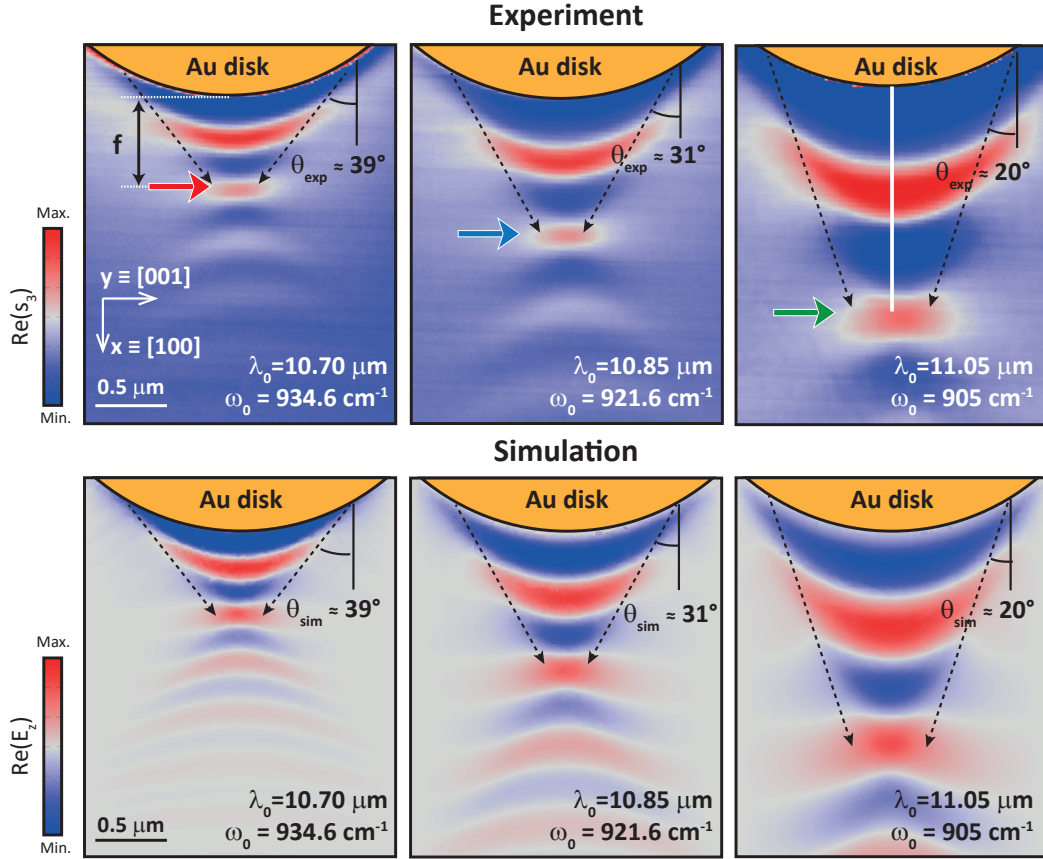
Figure 3.14: Focusing of In-Plane Hyperbolic Polaritons in α-MoO$_3$ **A**
Simulated near field, $\mathfrak{Re}(E_z)$, produced by a metal Au disk nanoantenna: The excitation and interference of PhPs with $\vec{k}_H$ wave vectors lead to a focal spot (yellow dashed circle). The right inset shows the analogous case for an in-plane isotropic medium using a rod-like metal nanoantenna with a concave extremity. The left inset shows the electric field amplitude, $|E_z|^2$, along the dashed red line (normalized to the intensity at the white cross). **B** Simulated near field, $\mathfrak{Re}(E_z)$, for a discrete distribution of point electric dipoles localized along the periphery of a virtual disk: A convex interference pattern and focal spot (yellow dashed circle) are revealed, resembling the results obtained in **A**. **C** Simulated near-field distribution, $\mathfrak{Re}(E_z)$, on a disk-like Au nanoantenna at $\lambda_0 = 11.05\,\mu m$ in an in-plane isotropic medium.

takes FWHM values (**Figure 3.16A**) that range from $\approx 310\,nm$ at $\lambda_0 = 10.70\,\mu m$ to $\approx 430\,nm$ at $\lambda_0 = 11.05\,\mu m$, i.e. in the order of $\lambda_0/34$, which indicate a deep subwavelength character.

The particular wavelength-dependent curvature of the hyperbolic IFC governs the propagation direction of PhPs with high-wavevector that leads to the formation of the foci (note that the propagation direction of hyperbolic PhPs in real space is given by the Poynting vector), as shown in the analytically calculated IFCs in **Figure 3.16B**. Therefore, while the angle of the Poynting vector dictates the wavelength-dependent focal distance, the wavevector (or wavelength of the polaritons) establishes the size of the focal spot. The foci size, FWHM, and the focal distance as a function of the illuminating wavelength is shown in **Figure 3.16C** for both experiment and simulation. An excellent agreement is found. It should be noted that although metal disks might be an interesting way to focus PhPs into deeply sub-wavelength confined focal spots, the contribution of polaritons with low-$\vec{k}$ (those propagating along directions within the IFC asymptotes) cannot be ruled out, which would indeed contribute to increase the size of the obtained focal spot. In this regard, metal nanoantennas with optimized geometries will be presented in the following section.

Optimization of the nanoantenna design for focusing of nanolight

The focusing effect described above arises from the interference of PhPs with high-$\vec{k}$ values, which could potentially take almost infinitely large values. However, it should also be noted that higher polaritonic wavevectors also imply lower polariton propaga-

Figure 3.15: Planar Focusing of In-Plane Hyperbolic PhPs with Au Disk Nanoantennas Experimental ($\mathfrak{Re}(s_3)$; top row) and simulated ($\mathfrak{Re}(E_z)$; bottom row) near-field images of PhPs launched by an Au disk nanoantenna fabricated on top of a $165\,nm$-thick α-MoO$_3$ crystal for illuminating wavelengths $\lambda_0 = 10.70\,\mu m$ (left), $\lambda_0 = 10.85\,\mu m$ (middle), and $\lambda_0 = 11.05\,\mu m$ (right). The interference of PhPs with $\vec{k}_H$ wave vectors launched from the edges of the nanoantenna results in a focal spot with a varying FWHM size and f as a function of λ_0. The dashed arrows mark the angle θ.

tion lengths, thus establishing a trade-off between the two quantities. Furthermore, apart from high-$\vec{k}$ PhPs, Au metal nanoantennas also launch polaritons with a relatively large wavelength along the α-MoO$_3$ [100] direction, which contributes to a broadening of the foci.

Therefore, to further reduce the size of the foci, rod-like trapezoidal Au nanoantennas with an optimized geometry are proposed to: 1) favour the excitation of high-$\vec{k}$ PhPs along a well-defined direction; 2) avoid the excitation of PhPs with relatively low $|\vec{k}|$ wavevectors (large wavelengths). Using these trapezoidal-shaped nanoantennas, the focal distance can be calculated by simple geometrical considerations, as shown schematically in **Figure 3.17B**. After performing some optimizations by numerical simulations to maximize the near-field intensity at the focus position, an optimal nanoantenna geometry was found in which the edges of the extremities of the trapezoidal nanoantennas form an angle of $\approx 44°$ with respect to the α-MoO$_3$ [100] crystalline direction at $\lambda_0 = 11.05\,\mu m$ ($\omega_0 = 905\,cm^{-1}$) (see **Figure 3.17A**) with a separation between the nanoantennas of $d = 320\,nm$. The metal nanoantenna
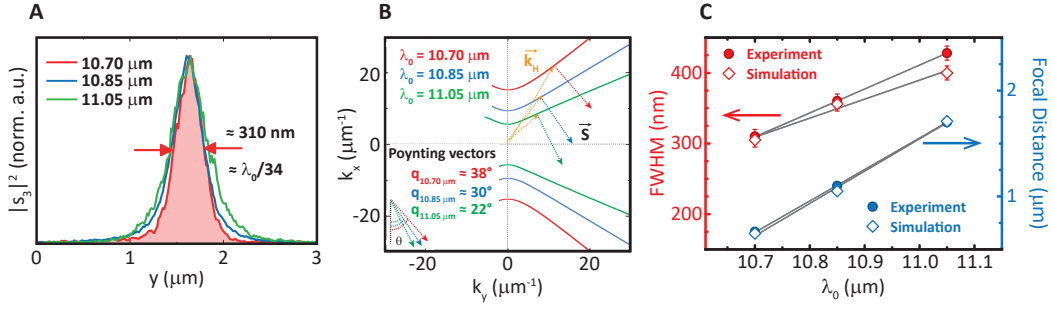
Figure 3.16: Foci Size and Focal Distance A Experimental near-field amplitude $|s_3|^2$ profiles along the 'y' axis at positions marked with an arrow in **Figure 3.14** for $\lambda_0 = 10.70\,\mu m$ (red), $\lambda_0 = 10.85\,\mu m$ (blue), and $\lambda_0 = 11.05\,\mu m$ (green). A deep subwavelength spot size of $\lambda_0/34$ ($\approx 310\,nm$) is measured for $\lambda_0 = 10.70\,\mu m$. **B** Analytical IFCs for a $165\,nm$-thick α-MoO$_3$ crystal at $\lambda_0 = 10.70\,\mu m$ (red), $\lambda_0 = 10.85\,\mu m$ (blue), and $\lambda_0 = 11.05\,\mu m$ (green). The Poynting vector $\vec{S}$ of PhPs with $\vec{k}_H$ wave vectors forms wavelength-dependent angles θ with respect to the x axis. **C** Dependence of the experimental, simulated, and analytically calculated values of the spot size (FWHM) and f with λ_0 (gray lines serve as a guide for the eye).

was fabricated on a $165\,nm$-thick α-MoO$_3$ flake. More details on the optimization can be found elsewhere [104].
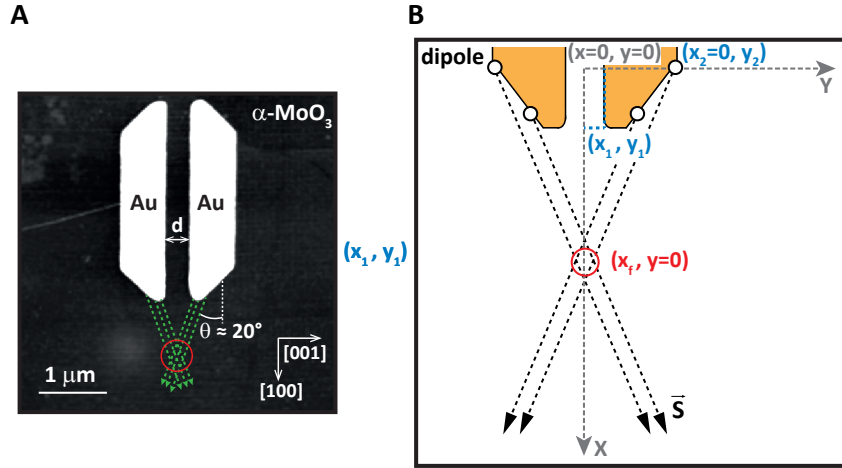
Figure 3.17: Understanding the Focusing of In-Plane PhPs in α-MoO$_3$ Employing Rod-Like Trapezoidal Nanoantennas A Topographic AFM image of a double rod-like trapezoidal Au nanoantenna separated by a distance $d = 320\,nm$ on an α-MoO$_3$ crystal. The slope of the nanoantennas edges at both extremities present an angle of $\approx 44°$ with respect to the [100] direction. The green dashed arrows illustrate the propagation of PhPs with $\vec{k}_H$ wave vectors excited from the edges of the nanoantennas ($\lambda_0 = 11.05\,\mu m$) that interfere at the focal spot marked with a red circle. **B** Focusing of PhPs excited by four electric point dipoles placed along the sidewall of rod-like trapezoidal nanoantennas on an α-MoO$_3$ slab. The black dashed arrows represent the Poynting vector of polaritons with wavevectors $\vec{k}_H$. The interference of polaritons gives rise to a focal spot marked by a red circle. The x-axis and y-axis correspond to the [100] and [001] crystalline directions in α-MoO$_3$, respectively.

55

Figure 3.18A shows the s-SNOM image, $\Re(s_3)$, obtained for a rod-like trape-zoidal Au nanoantenna fabricated on a $165\,nm$-thick at an illumination wavelength of $\lambda_0 = 11.05\,\mu m$. We observe the propagation of high-$\vec{k}$ PhPs (excited by the metal nanoantennas) that finally interfere producing a focused spot at a distance $f = 790\,nm$. By taking a profile along the α-MoO$_3$ [001] crystal direction passing through the focal spot (marked with a red arrow), we extract a FWHM of $\approx 225\,nm$, which corresponds to a deeply subwavelength size of $\approx \lambda_0/50$, or $\lambda_p/4.5$ ($\lambda_p \approx 1\,\mu m$ along the α-MoO$_3$ [100] crystalline axis). Note that in the previous section we showed a foci size of $\approx \lambda_0/34$ using an Au disk nanoantenna. To further verify our experimental results, we perform full-wave numerical simulations of the nanoantenna (**Figure 3.18B**). An excellent agreement with the experimental results for both the focal distance f and the focal spot size (FWHM, taken along the direction marked with the blue arrow) is obtained. Profiles along the foci extracted from both the experimental (red curve) and simulated (blue curve) images are displayed in **Figure 3.18C**.
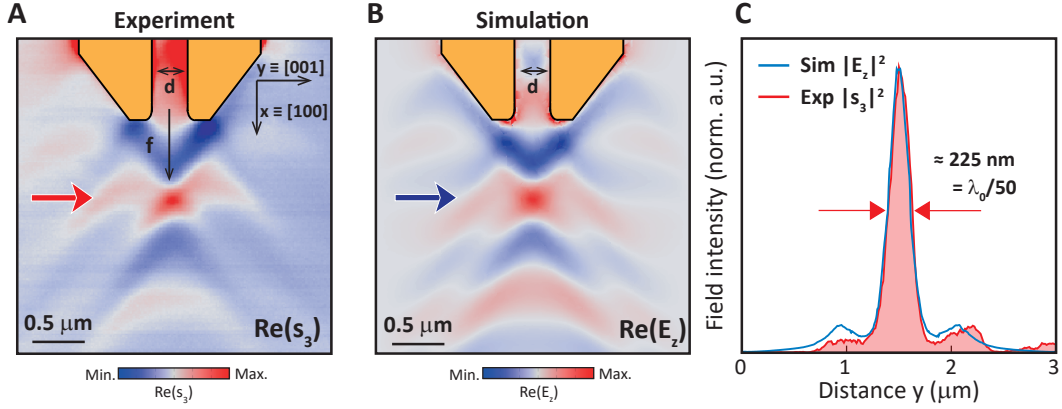
Figure 3.18: **Optical Nanoantennas for an Improved Planar Nanofocusing of In-Plane Hyperbolic PhPs in α-MoO$_3$** **A** Experimental near-field image, $\Re(s_3)$, of rod-like trapezoidal nanoantennas on an α-MoO$_3$ slab. **B** Simulated near-field images, $\Re(E_z)$, of rod-like trapezoidal nanoantennas on an α-MoO$_3$ slab. **C** Comparison between experimental/simulated near-field amplitude $|s_3|^2/|E_z|^2$ profiles taken along the y axis ([001] direction) at positions marked by a red/blue arrow in **A** and **B**, respectively. A deep subwavelength focusing of $\lambda_0/50$ ($\lambda_p/4.5$) is obtained.

It should be highlighted the possibility of varying the focal distance f by either changing the illumination frequency or increasing/decreasing the separation between the trapezoidal rods. Moreover, numerical simulations show that by reducing the distance between the trapezoidal rod-like nanoantennas, the focal distance can be lowered well below the diffraction limit when compared to the case of having PhPs in an isotropic medium. [104].

3.5 | Conclusions

To summarize, in this chapter we have explored the main physical characteristics of PhPs in α-MoO$_3$ within the MIR L- and U-RBs. PhPs propagate along all in-plane directions in the U-RB (from $\omega_{TO} \approx 960\,cm^{-1}$ to $\omega_{LO} \approx 1010\,cm^{-1}$) with the largest polaritonic wavelength along the [001] crystal direction and the shortest along the

[100] crystal direction. By Fourier transforming the s-SNOM images of propagating PhPs, the in-plane $\vec{k}$-space dispersion displays an ellipse in the U-RB, thus being coined as the 'elliptic band'. On the other hand, in the L-RB (from $\omega_{TO} \approx 820\,cm^{-1}$ to $\omega_{LO} \approx 970\,cm^{-1}$) PhPs propagate with the largest wavelength along the [100] crystal direction while no PhPs are observed along the [001] crystal direction. By Fourier transforming the s-SNOM images in the L-RB, the in-plane polaritonic dispersion in $\vec{k}$ space shows for the very first time in-plane hyperbolic propagation of phonon-polaritons, thus coining this RB as the 'hyperbolic' band. Moreover, PhPs in the elliptic band propagate with negative phase velocity while in the hyperbolic band the phase velocity takes positive values. Also, the polariton confinement is higher in the elliptic band than in the hyperbolic band. Using a simple 2D model, the in-plane permittivities in both bands can be extracted and the sign of the z-component can be deduced. The model also predicts an inverse dependence of the polaritonic wavevector on the thickness of the α-MoO$_3$ flake which exactly matches the experimental results. Furthermore, PhPs in both bands are found to propagate with extremely small group velocities resulting in thickness-independent lifetimes of the same order of magnitude that the best values reported so far for hyperbolic PhPs and four times longer than the best values reported so far for any sub-diffractional polariton.

For applications in the field of nanooptics, the in-plane propagation of PhPs in α-MoO$_3$ is very interesting for the development of a planar technology. Importantly, as the first optical element to manipulate light at the nanoscale, metallic nanoantennas with tailored geometries are demonstrated to provide foci with a FWHM that is 50 times smaller than the wavelength of the incident radiation. This achievement hold promises for the development of optical circuitry at the nanoscale with unprecedented capabilities.

Spectral Tuning of PhPs in a van der Waals material by ion intercalation

In this chapter we will present α-V_2O_5 as a van der Waals material that supports PhPs in the MIR spectral range. To study the properties of these PhPs, we will first extract an accurate dielectric function of α-V_2O_5 with the help of s-SNOM measurements, transfer matrix and DFT calculations. More Importantly, we will show that by intercalating the crystal structure with Na atoms (forming the α'-NaV_2O_5 crystal) it is possible to extend (up to $30\,cm^{-1}$) the RB in which the PhPs exist. Finally, we will show that such an intercalation process does not affect the long lifetimes (up to $6\,ps$) and large quality factors (up to 3.5) of PhPs. The results showed in this chapter have been published in Taboada-Gutiérrez et al. 'Broad spectral tuning of ultra-low-loss polaritons in a van der Waals crystal by intercalation', Nature Materials 19, 964–968 (2020).

4.1 │ Introduction to α-V_2O_5

In recent years, there has been intensive research on deeply confined polaritons, and in particular on PhPs. Although PhPs present unique properties, such as ultrahigh confinement and long lifetimes, they also present a major drawback: they can only be excited in narrow spectral bands (RBs) of a few van der Waals materials. Therefore, it would be very interesting, both from a fundamental and technological point of view, to find an efficient strategy to shift or modify the RBs, thus allowing PhPs to be controlled over wider frequency ranges. In this Chapter we will show that this problem can be addressed by intercalating alkali atoms at certain positions in the crystal structure of the van der Waals material α-V_2O_5. α-V_2O_5 is a low-cost and abundant material that has been studied via intercalation for its use in applications such as photocatalysis [143], as electrodes in lithium-ion batteries [144, 145] or as gas sensors [146]. In this case, α-V_2O_5 is presented as a material that supports ultra-low-loss PhPs whose dispersion is tunable by controlling the crystal thickness. Importantly, by intercalating the material with alkali atoms (sodium and calcium, without modifying the space group of the material), an unprecedented spectral shift of its RBs can be obtained, allowing PhPs to be excited in broadband frequency ranges.

Crystal Structure

The thermodynamically stable alpha phase of V_2O_5 (α-V_2O_5) crystallizes in a *Pmmn* (number 59) orthorhombic crystal structure with lattice parameters $a = 11.512\,\text{Å}$, $b = 4.368\,\text{Å}$ and $c = 3.564\,\text{Å}$ and two formula units per unit cell ($Z = 2$) [147]. It is a layered material where the individual layers with a thickness of $3.779\,\text{Å}$ are held together by van der Waals forces along the [010] crystalline direction ('z', in the following). Each layer is composed of a periodic repetition of VO_5 square pyramids that pointing alternatively up and down share edges or corners. As in α-MoO_3, three different kinds of oxygen atoms can be identified [148]:

- The vanadyl oxygen O_v which bonds exclusively to one V atom with a bond distance of $1.464\,\text{Å}$ and constitutes the apex of the pyramid.

- The bridge oxygen O_b which bonds to two different V atoms and connects the chains together with a bond distance of $1.896\,\text{Å}$.

- The chain oxygen O_c which bonds to three different V atoms, two inside a pyramid pointing down (or up) and the other one inside a pyramid pointing up (or down) with average distances of $1.910\,\text{Å}$ and $1.997\,\text{Å}$, respectively.

Figure 4.1 shows the α-V_2O_5 crystal structure along with the material unit cell together with its basic constituent VO_5 pyramid and an optical image with a few α-V_2O_5 flakes on a SiO_2/Si substrate.
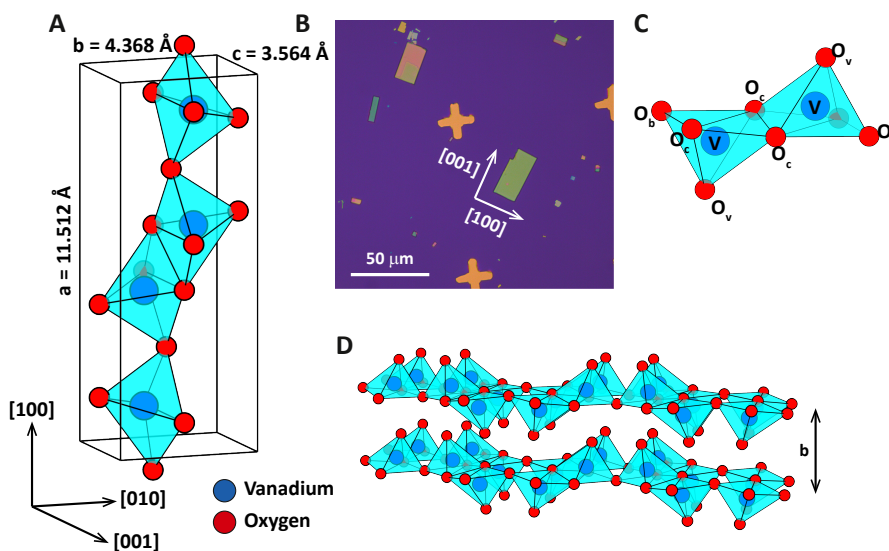
Figure 4.1: α-V_2O_5 Crystal Structure A Schematic of the α-V_2O_5 unit cell. The unit cell consists of a periodic repetition of distorted VO_5 pyramids pointing alternatively up and down. The V atom (blue circles) are located in the center of the pyramid, which is defined by the O atoms (red circles). **B** Optical image of some α-V_2O_5 flakes exfoliated on a SiO_2/Si substrate. Due to the anisotropic crystal structure of α-V_2O_5 the flakes present a rectangular shape with well-defined edges and easy-recognizable crystallographic directions (larger/shorter sides correspond to the [001]/[100] crystal directions, respectively). **C** Schematic of the VO_5 pyramids with the three non-identical oxygen atoms labeled. **D** Schematic of the layered structure of α-V_2O_5.

MIR optical properties: Far-Field Characterization by FTIR

Based on group theory, for the α-V$_2$O$_5$ $Pmmn$ space group there are 42 modes at the Γ point ($k = 0$): 3 of them correspond to translations while the other 39 are optical modes [149]:

- 15 IR active modes: $6B_{1u}+3B_{2u}+6B_{3u}$ which corresponds to vibrations along the [010], [001] and [100] crystalline directions, respectively.

- 21 Raman active modes: $7A_{1g}+3B_{1g}+7B_{2g}+4B_{3g}$

- 3 silent modes: $3A_{1u}$

The IR permittivity of α-V$_2$O$_5$ was first reported by Clauws and Vennik in 1976 [150] from FTIR polarized reflectance measurements (**Figure 4.2**), which showed three RBs (shadowed regions), each along a different crystallographic direction, as predicted in reference [149]. Specifically, the active modes that present resonances in the MIR regime and give rise to the α-V$_2$O$_5$ Reststrahlen Bands (due to the TO-LO splitting) are the following: i) the B_{1u} V-O$_v$ stretching mode along the [010] crystal direction between $\omega_{TO} = 974\,cm^{-1}$ and $\omega_{LO} = 1040\,cm^{-1}$ (hereafter RB$_1$), ii) the B_{3u} O$_c$-V-O$_b$ stretching mode along the [100] crystal direction between $\omega_{TO} = 766\,cm^{-1}$ and $\omega_{LO} = 965\,cm^{-1}$ (hereafter RB$_2$) and iii) the B_{2u} V-O$_c$ stretching mode along the [001] crystal direction between $\omega_{TO} = 506\,cm^{-1}$ and $\omega_{LO} = 844\,cm^{-1}$ (hereafter RB$_3$) [149]. Another narrow band between $\omega_{TO} = 981\,cm^{-1}$ and $\omega_{LO} = 987\,cm^{-1}$ polarized along the [100] direction is theoretically predicted [149], however, experimental reports only reveal an extremely small band between $\omega_{TO} = 980.5\,cm^{-1}$ and $\omega_{LO} = 982\,cm^{-1}$ [150]. **Table 4.1** summarizes the extracted parameters by Clauws and Vennik of the MIR permittivity function of α-V$_2$O$_5$.
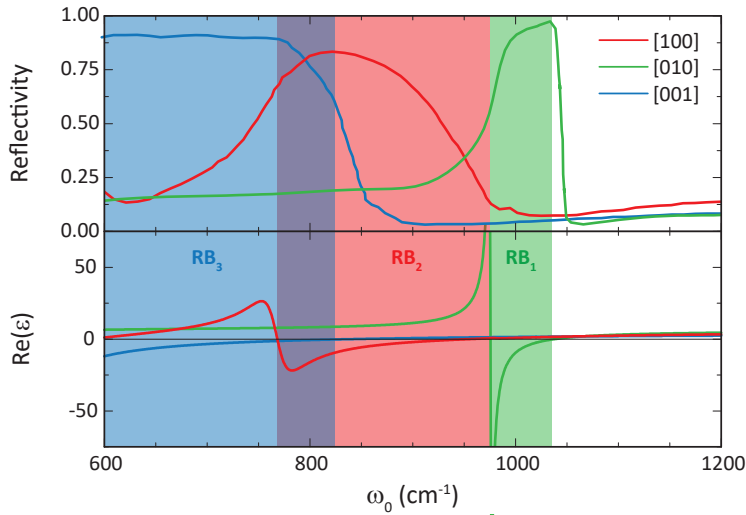
Figure 4.2: Reflectance Measurements and Extracted Permittivity of α-V$_2$O$_5$ Reflectivity (upper panel) and permittivity (lower panel) of α-V$_2$O$_5$ along the three crystallographic directions. Three reststrahlen Bands each along a different crystal direction can be observed. Adapted from reference [150]).

The α-V$_2$O$_5$ crystals studied in this thesis were synthesized via a purification method and subsequent single crystal growth by the group of Professor Kimura at University of Tokyo [151]. We first carried out polarization resolved FTIR spectroscopy on α-V$_2$O$_5$ flakes (**Figure 4.3**) placed on a BaF$_2$ substrate (transparent

Axis	$\omega_{TO}\,(cm^{-1})$	$\gamma_{TO}\,(cm^{-1})$	$\omega_{LO}\,(cm^{-1})$	$\gamma_{LO}\,(cm^{-1})$
[100]	767.5	30.0	959.0	50.0
[010]	975.5	2.5	1038.0	2.5
[001]	506.5	21.0	842.5	18.0

Table 4.1: Reported Parameters of the MIR permittivity of α-V$_2$O$_5$ α-V$_2$O$_5$ dielectric constant parameters in the MIR regime (adapted from [150]).

in the frequency range of interest). The resulting spectra, obtained for both the [100] and [001] in-plane directions of a $280\,nm$-thick α-V$_2$O$_5$ flake, show a strong peak at $\omega_0 = 773\,cm^{-1}$ and a weak peak at $\omega_0 = 982\,cm^{-1}$ when polarized along the [100] crystal direction. On the other hand, when polarized along the [001] crystallographic direction, a small peak is observed at $\omega_0 = 1038\,cm^{-1}$. These peak positions are in excellent agreement with some of the TO and LO phonon positions reported by Clauws and Vennik [150]. We stress that the FTIR reflectivity spectra shown in **Figure 4.2** were performed on relatively thick flakes or single crystals (thickness $> 1\,\mu m$), and therefore all resonances are clearly revealed. However, in our thin flake only strong resonances (phonons) can be detected, i.e., only the TO phonon positions can be extracted from these measurements. In general, excitation of LO phonons (longitudinal vibrations) is not allowed employing transverse electromagnetic waves. However, note that when dealing with longitudinal waves along the out-of-plane crystallographic direction ([010] crystallographic direction, perpendicular to the vdW layers), they manifest as transverse waves along the orthogonal directions (in-plane directions). Moreover, in our FTIR system light does not impinge perpendicularly to the sample, and consequently light is not 100% s-polarized. Indeed, there is a small p-polarization contribution which let us have access to some information about the vibrational modes along the [010] direction. In this case, the LO position of the RB$_1$ can be recognized as shown in **Figure 4.3**. Consequently, we can assign that peak positions $\omega_{TO}^1 = 773\,cm^{-1}$ and $\omega_{TO}^2 = 982\,cm^{-1}$ as TO vibrations along the [100] crystallographic direction and $\omega_{LO} = 1038\,cm^{-1}$ as a LO vibrational mode along the [010] crystalline direction. This data will serve as input to fine tune the dielectric permittivity of the material by also performing *ab initio* calculations and near-field imaging, as it will be shown in Section 4.4.
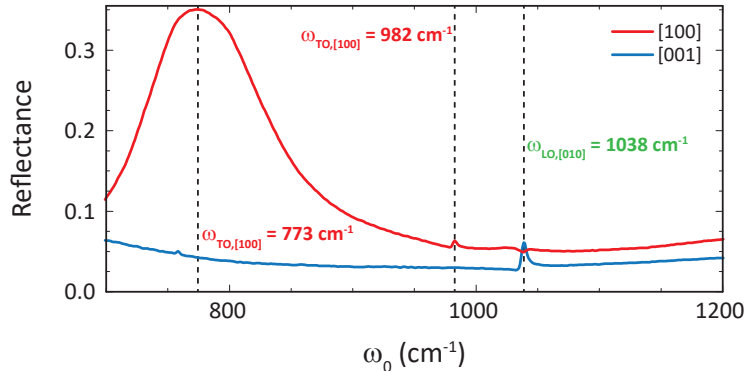
Figure 4.3: Experimental Reflectivity from an α-V$_2$O$_5$ flake FTIR in-plane polarized reflectance of a 280 nm-thick α-V$_2$O$_5$ flake.

4.2 | Near-Field optical properties of α-V$_2$O$_5$: s-SNOM characterization

To study the excitation and propagation of PhPs in different RBs of α-V$_2$O$_5$, we performed s-SNOM near-field nanoimaging at different illuminating frequencies. In particular, **Figure 4.4A, B** and **C** show the resulting near-field amplitude images taken on a $105\,nm$-thick α-V$_2$O$_5$ flake on a SiO$_2$/Si substrate at $\omega_0 = 1031$, 1026 and $1020\,cm^{-1}$, respectively. Bright fringes parallel to all flake edges are observed with different periodicities depending on the crystal direction, indicating in-plane anisotropic propagation of PhPs. This anisotropy can be further examined by extracting profiles along both the [100] and [001] in-plane directions (right panels in the figure). At $\omega_0 = 1026\,cm^{-1}$ (**Figure 4.4B**) polariton wavelengths of $\lambda_{p,[100]} = 915\,nm$ and $\lambda_{p,[001]} = 800\,nm$ are measured along the [100] and [001] crystal directions, respectively (note that, as explained in the previous chapter, PhPs excited by the tip result in near-field fringes with a $\lambda_p/2$ spacing. However, polaritons simultaneously launched by the flake edges with a periodicity equal to λ_p cannot be excluded. As such, polaritonic doublets due to both contributing effects are also expected to be observed [**103**]). Apart from revealing the anisotropic propagation of PhPs in α-V$_2$O$_5$, these near-field profiles also show a deep-subwavelength confinement of light, as the ratio $\lambda_0/\lambda_p^{[001]}$ results in values as large as 12 (for $\lambda_0 = 9.75\,\mu m$) and thus $\lambda_p \ll \lambda_0$

The polariton dispersion curves corresponding to the [100] and [001] crystal directions (**Figure 4.4D**) (extracted from s-SNOM single frequency measurements as those shown in **Figure 4.4A, B** and **C** are slightly shifted with respect to each other, clearly indicating the in-plane anisotropic propagation of PhPs in α-V$_2$O$_5$ within the RB$_1$. Remarkably, the PhPs wavelength increases with the frequency, an indication of a negative phase velocity (see Section 3.2). This is further corroborated by plotting the imaginary part of the s-SNOM signal s_3 as a function of its real part, observing a counterclockwise rotating spiral (**Figure 4.5**) [**41, 70**].

We now study the PhPs propagation at frequencies within the RB$_2$ of α-V$_2$O$_5$, i.e., at frequencies between 766 and $965\,cm^{-1}$. **Figure 4.6A** shows experimental s-SNOM images taken at $\omega_0 = 855$ and $875\,cm^{-1}$. In contrast to PhPs in RB$_1$, PhPs in RB$_2$ are only visible along the [100] crystal direction, showing a wavelength (see profiles in **Figure 4.6B**) of $\lambda_{p[100]} = 950\,nm$ at $\omega_0 = 875\,cm^{-1}$ ($\lambda_0 = 11.43\,\mu m$). Apart from revealing a strong anisotropic propagation of PhPs, these near-field profiles also show a deep-subwavelength confinement of light, as the ratio $\lambda_0/\lambda_p^{[100]}$ results in values as large as 12 (for $\lambda_0 = 11.43\,\mu m$) and thus $\lambda_p \ll \lambda_0$.

Unfortunately near-field s-SNOM nanoimaging of PhPs in RB$_3$ (from $\omega_0 = 506\,cm^{-1}$ to $844\,cm^{-1}$) of α-V$_2$O$_5$ is not possible to perform at the moment due to the lack of suitable lasers*

---

*Current quantum cascade laser (QCL) technologies do not offer high-power continuous-wave laser sources at operating frequencies around α-V$_2$O$_5$ RB$_3$ [**152**].
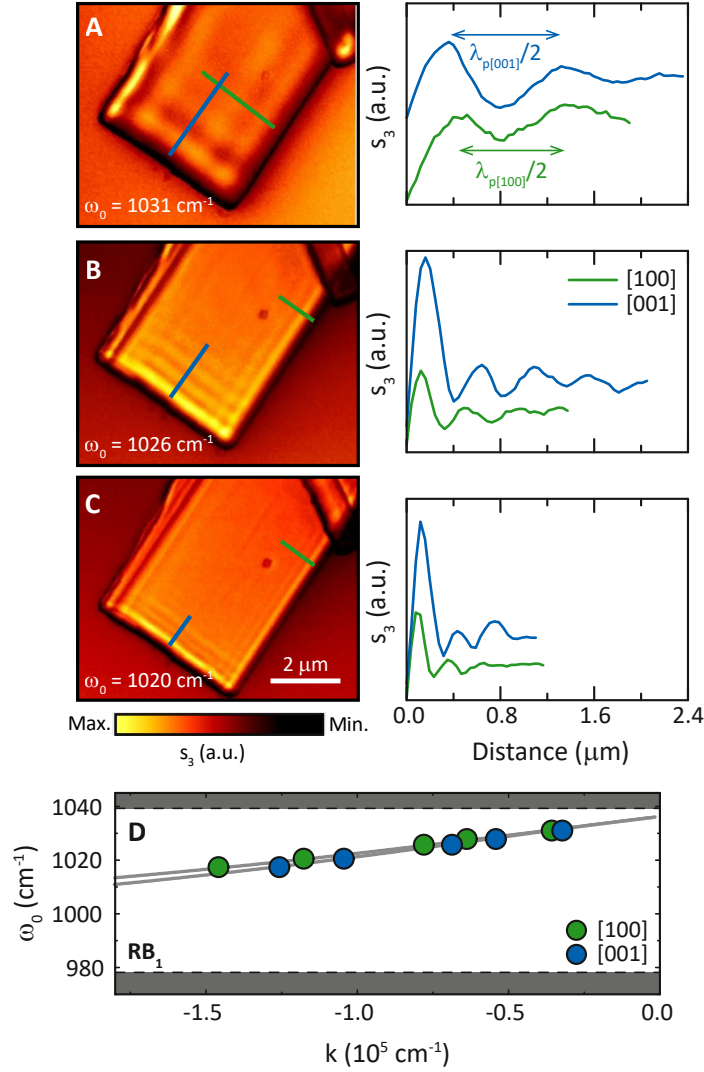
Figure 4.4: Near-Field Nanoimaging of PhPs in RB$_1$ of α-V$_2$O$_5$ A-C left panel: Experimental near-field amplitude images s_3 obtained on an α-V$_2$O$_5$ flake with thickness $d = 105\,nm$ at incident frequencies $\omega_0 = 1031$ (**A**), 1026 (**B**) and $1020\,cm^{-1}$ (**C**). Right panel: Profiles along the [100] (green lines) and [001] (blue lines) crystal directions, extracted along the profiles shown in the near-field amplitude images to the left. $\lambda_{p[100]}$ and $\lambda_{p[001]}$ are the polariton wavalengths along the [100] and [001] crystal directions, respectively. **D** Dispersions of PhPs along the [100] (green circles) and [001] (blue symbols) crystal directions. Grey lines are guides for the eye. Grey shaded areas indicate the spectral regions outside the RB$_1$.

4.3 | Intercalation with Na atoms: From α- V$_2$O$_5$ to NaV$_2$O$_5$

Doping and intercalation of the α-V$_2$O$_5$ structure has been studied in depth for the integration of this material in different technologies and applications, such as photo-catalysis, electrodes in Li-ion batteries or electrochromic devices [153]. It has been demonstrated that the α-V$_2$O$_5$ crystalline structure can be intercalated with Li, Na, Cs, Mg, Ca, K, Ag and Cu, among others [154, 155, 156, 157, 158, 159, 160], some of them even modifying the magnetic structure of the material.
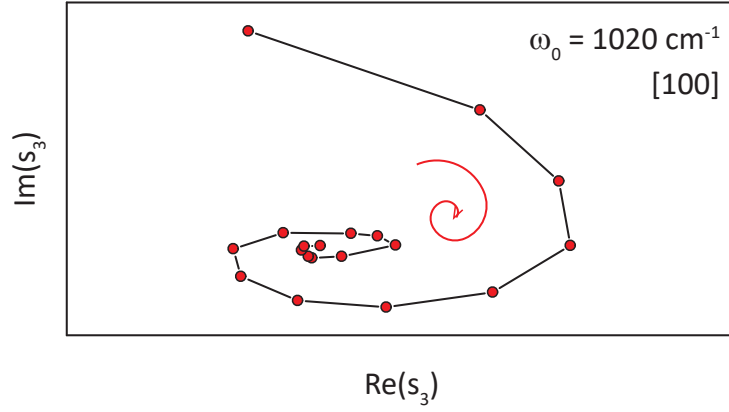
Figure 4.5: Sign of the Phase Velocity of α-V$_2$O$_5$ PhPs in RB$_1$ Plot of the imaginary part of the complex-valued s-SNOM signal s_3 (measured along the [100] direction in the upper band (RB$_1$) at a frequency of $\omega_0 = 1020\,cm^{-1}$) as a function of the real part. A counterclockwise rotating spiral is revealed indicating a negative phase velocity. The same qualitative results apply for the [001] crystal direction.
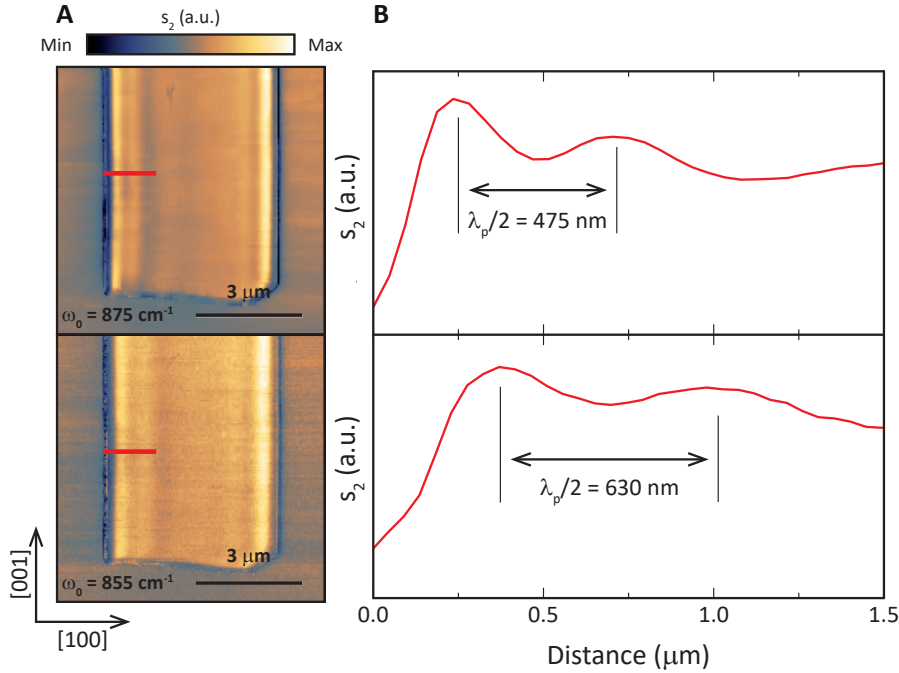
Figure 4.6: Near-Field Nanoimaging of PhPs in RB$_2$ of α-V$_2$O$_5$ **A** Near-field amplitude s-SNOM images s_2 of an α-V$_2$O$_5$ flake with thickness $d = 155\,nm$ at incident frequencies $\omega_0 = 875\,cm^{-1}$ (upper panel) and $\omega_0 = 855\,cm^{-1}$ (lower panel). **B** Near-field s_2 profiles extracted along the [100] crystal directions in the images shown in **A** (red lines).

Independent of the doping atom, multiple crystalline phases exist depending on the doping content. Intercalation is possible due to the reduction of some V^{5+} atoms into V^{4+}. Among all the intercalated materials, α'-NaV$_2$O$_5$ has certainly attracted much more attention and debate than any other due to the presence of an exotic magnetic phase transition below $T = 34\,K$ [154, 161, 162, 163, 164]. The nature of this transition is still controversial and will not be studied in this thesis. In this

Section, the intercalation of Na (from an experimental and theoretical point of view) and Ca (from a theoretical point of view) in the α-V$_2$O$_5$ structure will be studied. In both cases the *Pmmn* space group is preserved.

As a natural consequence of the crystal distortion mediated by the intercalation of foreign atoms in α-V$_2$O$_5$, a change in the vibrational resonances of the phonons in the crystal and, consequently, a change in the frequency range of the RBs can be expected. In this regard, the effect of intercalation on the polaritonic response in vdW crystals has been scarcely studied [165], and will be addressed in this section. **Figure 4.7** presents the structure of α'-NaV$_2$O$_5$ together with its unit cell and an optical image of a flake on a SiO$_2$/Si substrate. As mentioned above, α'-NaV$_2$O$_5$ maintains intact the *Pmmn* space group of α-V$_2$O$_5$: lattice parameters $a = 11.315$ Å, $b = 4.80$ Å and $c = 3.615$ Å (see **Figure 4.7A**, note the increasing of the interlayer distance, b parameter, due to the presence of the Na atoms from 4.37 Å to 4.80 Å). As a consequence of the intercalation of Na atoms, the pyramids are slightly modified. The V-O$_v$ (vanadyl oxygen) distance increases to 1.60 Å, while the V-O$_b$ (bridge oxygen) distance does not change. The V-O$_c$ (chain oxygen) bond lengths are 1.957 Å and 1.969 Å. Finally, Na-O$_b$ distance is 2.294 Å and the Na-V separation is 3.328 Å. The layer thickness also expands to 4.152 Å (without considering Na atoms), where Na atoms are preferentially located between the layers (see **Figure 4.7C**).
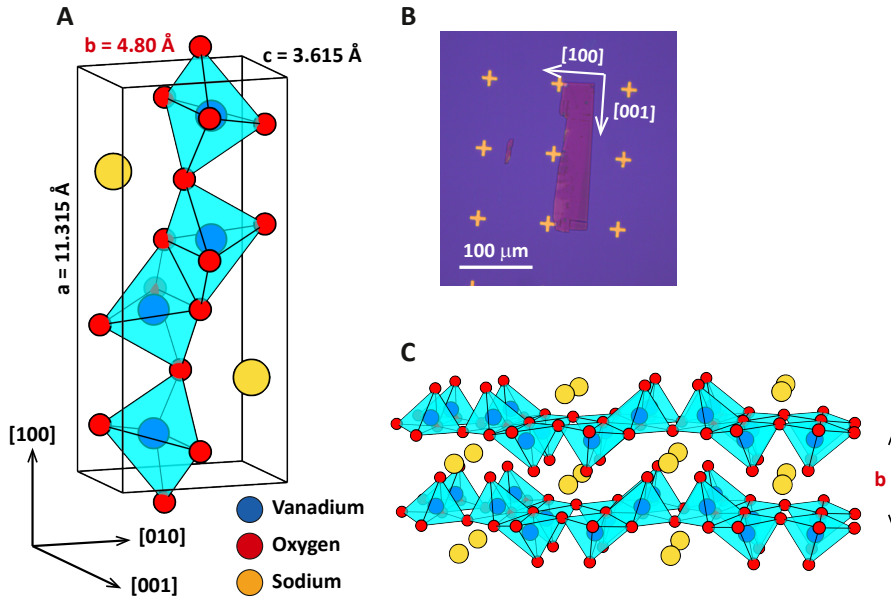
Figure 4.7: Crystal Structure of the Intercalated α'-NaV$_2$O$_5$ Crystal A Schematic of the unit cell of α'-NaV$_2$O$_5$. As in α-V$_2$O$_5$, the unit cell consists of a periodic repetition of VO$_5$ distorted pyramids pointing alternatively up and down with the V atom (blue circles) in the center of the pyramid defined by the O atoms (red circles). The sodium atoms (yellow circles) are intercalated in the layered structure. **B** Optical image of an α'-NaV$_2$O$_5$ flake on a SiO$_2$/Si substrate. **C** Schematic of the layered structure of α'-NaV$_2$O$_5$.

To study the effect of the intercalation on the propagation of PhPs, we firstly explore the spectroscopic response of α-V$_2$O$_5$ by performing nanoscale Fourier-transform infrared spectroscopic (nanoFTIR) measurements along both the [100] and [001] in-plane directions (**Figure 4.8A**) on a $245\,nm$-thick α-V$_2$O$_5$ flake on a SiO$_2$ substrate.

66

We observe three different spectral bands: from $\approx 975\,cm^{-1}$ to $\approx 1040\,cm^{-1}$ (RB$_1$); from $\approx 800\,cm^{-1}$ to $\approx 975\,cm^{-1}$ (RB$_2$), and from $\approx 750\,cm^{-1}$ (the lowest frequency reached by our nanoFTIR system) to $\approx 800\,cm^{-1}$ (RB$_3$), which agree well with RB$_1$, RB$_2$ and RB$_3$ shown in **Figure 4.2**. In RB$_1$, we find polariton fringes propagating along both in-plane directions, showing an increasing wavelength λ_p with increasing frequency (verifying the negative phase velocity of PhPs in RB$_1$, as shown in Section 4.2). The periodicities of these PhPs are slightly different along both in-plane directions, revealing their elliptic nature. In contrast, in RB$_2$ we find fringes that only propagate along the [100] direction (highlighted with a white dashed line in the figure), with no visible fringes along the [001] direction. Therefore, as expected from the results of Section 4.2, PhPs in RB$_2$ of α-V$_2$O$_5$ propagate with a strongly anisotropic dispersion (hyperbolic). Moreover, λ_p decreases with increasing frequency, indicating that PhPs in RB$_2$ have a positive phase velocity. Finally, in RB$_3$ we find fringes along the [001] direction (highlighted with white dashed lines), indicating again the existence of in-plane hyperbolic PhPs, which, however, are now in-plane orthogonal to those in RB$_2$. Taken together, these nanoFTIR results confirm the strongly anisotropic propagation of PhPs along both in-plane directions within different RBs of α-V$_2$O$_5$.

The investigation of the effects of the Na intercalation on the structure of α-V$_2$O$_5$ is presented below. **Figure 4.8B** shows nanoFTIR line scans of a $150\,nm$-thick α'-NaV$_2$O$_5$ flake along the [100] and [001] crystal directions in the frequency range from $\omega_0 = 750\,cm^{-1}$ to $\omega_0 = 1050\,cm^{-1}$. We observe a bright band that, interestingly, looks very similar to RB$_1$ in α-V$_2$O$_5$, but red-shifted. Within this band we observe amplitude fringes, indicating the existence of PhPs. They show and increasing periodicity with increasing frequency, revealing a negative phase velocity, similar to PhPs in RB$_1$ of α-V$_2$O$_5$. Apart from these PhPs we do not observe other amplitude fringes in the nanoFTIR spectra of α'-NaV$_2$O$_5$: the hyperbolic bands RB$_2$ and RB$_3$ in α-V$_2$O$_5$ seem to be suppressed or largely shifted upon Na intercalation.

To better analyze the effect of intercalation on the propagation of PhPs in RB$_1$ of α-V$_2$O$_5$, we extract the dispersion for both pristine and Na-intercalated flakes from monochromatic s-SNOM images (**Figure 4.9A**). A clear redshift of $\approx 30\,cm^{-1}$ from center to center of the RB$_1$s is found (α-V$_2$O$_5$ is represented with solid circles while α'-NaV$_2$O$_5$ is represented with open circles, black and orange colors indicate the [100] and [001] crystal directions, respectively). The values of ω_{TO} and ω_{LO} are indicated with solid and dashed lines, respectively. Grey shaded regions show the frequency areas outside of the RB$_1$s. These results unequivocally demonstrate that RB$_1$ can be largely shifted by the intercalation of Na atoms in the α-V$_2$O$_5$ crystal structure, or in other words, the dispersion of PhPs can be tuned in a broad range via the intercalation of Na atoms into the polaritonic material.

To better understand the effects of Na intercalation in the α-V$_2$O$_5$ structure and the apparent suppression of RB$_2$ and RB$_3$, we calculate the phonon dispersions of α'-NaV$_2$O$_5$ from density functional theory (DFT) (performed by Ion Errea at Donostia International Physics Center (DIPC). DFT (also known as *ab initio*, or first principles calculations) is a method for determining the atomic and molecular structure of materials, bond lengths and angles, etc., from the first principles of quantum mechanics (i.e., finding the ground state of the quantum-mechanical system) [166, 167, 168]. The theory is based on changing the frame of the the N-electron wavefunction prob-
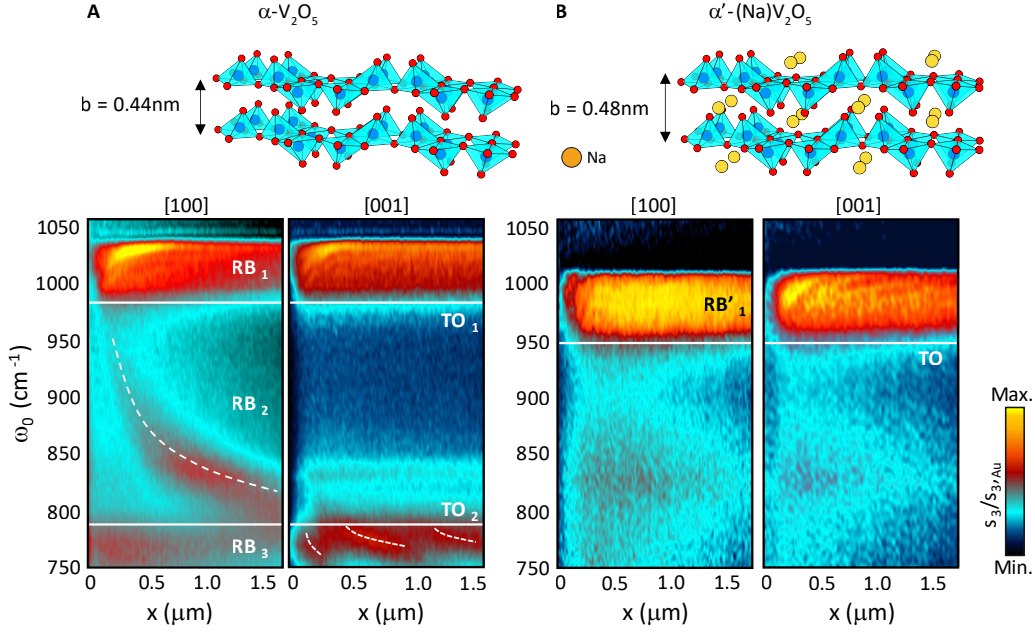
Figure 4.8: Nano-FTIR Line Scans on α-V$_2$O$_5$ and Intercalated α'-NaV$_2$O$_5$
A Upper panel: Illustration of the α-V$_2$O$_5$ lattice structure (orthorhombic). The red spheres represent oxygen atoms, the blue atoms represent vanadium atoms, and the blue pyramids show the polyhedral structure defined by the oxygen atoms. The crystal structure consists of bilayers of distorted VO$_5$ pyramids stacked along the [010] direction via vdW interactions (interlayer distance $b = 0.44\,nm$). Lower Panel: nanoFTIR spectral line scans along the [100] and [001] directions of a α-V$_2$O$_5$ flake showing $s_3/s_{3,Au}$ (near-field amplitude s_3 normalized on Au, $s_{3,Au}$) as a function of distance between the tip and the flake edge. Solid horizontal lines mark the approximate transversal optic (TO) phonon modes in α-V$_2$O$_5$ (TO$_1$, $975\,cm^{-1}$; TO$_2$, $770\,cm^{-1}$), separating RB$_{1-3}$. Dashed lines are guides for the eye of signal maxima. The flake thickness is $d = 245\,nm$. **B** Upper panel: Illustration of the α'-NaV$_2$O$_5$ lattice structure (orthorhombic). The red spheres represent oxygen atoms, the blue atoms represent vanadium atoms, the yellow atoms represent sodium atoms and the blue pyramids show the polyhedral structure defined by the oxygen atoms. The crystal structure consists of bilayers of distorted VO$_5$ pyramids with sodium atoms intercalated and stacked along the [010] direction via vdW interactions (interlayer distance $b = 0.48\,nm$). Lower panel: nanoFTIR spectral line scans along the [100] and [001] directions of a α'-NaV$_2$O$_5$ flake showing $s_3/s_{3,Au}$ (near-field amplitude s_3 normalized on Au, $s_{3,Au}$) as a function of distance between the tip and the flake edge. The solid horizontal line approximately mark the transversal optic phonon mode in α'-NaV$_2$O$_5$ (TO, $950\,cm^{-1}$), defining RB'$_1$. The flake thickness is $d = 150\,nm$.

lem of the system $\Psi(\vec{x}_1, \vec{x}_2, \vec{x}_3, \dots \vec{x}_N)$ (thus $3N$ independent variables) and all the equations involved by a simpler problem based on the charge density $\rho(\vec{r})$ which depends on only 3 variables (the spatial variables x, y and z). In our case, we have employed DFT to obtain the phonon frequencies, the polarization vectors, the effective charges, and the high-frequency limit of the dielectric function. The calculations were implemented in the open source software Quantum Espresso [42]. These calculations were performed within the Perdew, Burke, and Ernzerhof parametrization of the exchange-correlation functional [169]. Once calculated these parameters, the
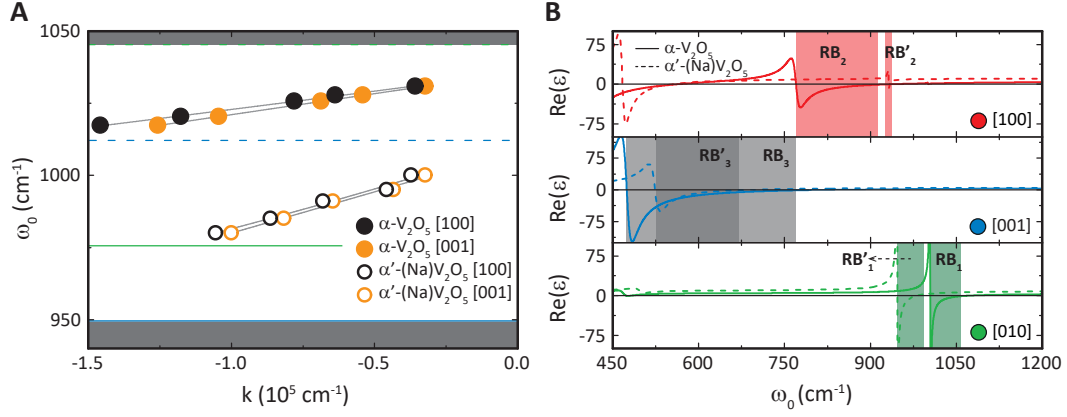
Figure 4.9: Dispersion of PhPs and Calculated Permittivity in α-V$_2$O$_5$ and Intercalated α'-NaV$_2$O$_5$ Crystals A Dispersion of PhPs along the [100] and [001] directions in an α-V$_2$O$_5$ (full symbols) flake with thickness $d = 105\,nm$ and an α'-NaV$_2$O$_5$ (empty symbols) flake with thickness $d = 190\,nm$. Dashed and continuous horizontal lines mark the approximate transverse and longitudinal optic phonon modes in α-V$_2$O$_5$ (transverse optic, $980\,cm^{-1}$; longitudinal optic, $1040\,cm^{-1}$) and α'-NaV$_2$O$_5$ (transverse optic, $945\,cm^{-1}$ and longitudinal optic, $1015\,cm^{-1}$), respectively. Grey lines are guides for the eye. Grey shaded areas indicate the spectral regions outside the RBs. **B** Real part of the permittivities for α-V$_2$O$_5$ (continuous lines) and α'-NaV$_2$O$_5$ (dashed lines) extracted from ab initio calculations along the principal [100], [010] and [001] axes (red, blue and green lines, respectively). The Reststrahlen bands RB$_{1\vee3}$, and RB'$_{1\vee3}$ for α-V$_2$O$_5$ and α'-NaV$_2$O$_5$, are indicated in bright and dark shading, respectively. Green shaded regions represent RB$_1$ and RB'$_1$; red shaded regions represent RB$_2$ and RB'$_2$ and grey shaded regions represent RB$_3$ and RB'$_3$.

dielectric tensor of α'-NaV$_2$O$_5$ was extracted within the perturbation theory [**170**].

The extracted phonon modes (along with those obtained for pristine α-V$_2$O$_5$) are then used in a 4 parameter Lorentz oscillators model (**Equation 1.7**) to retrieve the theoretical permittivities for both crystal structures (**Figure 4.9B**). **Table 4.2** lists the as-obtained ω_{TO}, ω_{LO}, ε_∞ and γ parameters of the model. The RBs in the intercalated material are referred to as RB'$_{1-3}$. Starting with α-V$_2$O$_5$, we find three RBs (RB$_{1-3}$ marked with shaded regions) within the frequency range shown (from $\omega_0 = 450\,cm^{-1}$ to $\omega_0 = 1200\,cm^{-1}$). They are directly related to each of the crystal directions (red, blue and green lines for the [100], [001] and [010] crystal directions). For α'-NaV$_2$O$_5$, we also obtained three RBs (RB´$_{1-3}$ marked with shaded regions), but they typically appear narrower and with their center shifted with respect to RB$_{1-3}$ in α-V$_2$O$_5$. For example, RB´$_1$ in α'-NaV$_2$O$_5$ (along the [010] crystal direction) is redshifted (about $50\,cm^{-1}$), RB´$_2$ (in-plane hyperbolic in α-V$_2$O$_5$) is blue-shifted ($\approx 76\,cm^{-1}$) and much narrower (narrowing from $174\,cm^{-1}$ to $2.5\,cm^{-1}$), and RB´$_3$ (in-plane hyperbolic in α-V$_2$O$_5$) is ref-shifted ($\approx 38\,cm^{-1}$) and narrower (from $341\,cm^{-1}$ to $166\,cm^{-1}$). These values explain the absence of RB´$_2$ and RB´$_3$ in our nanoFTIR experiments, as the nanoFTIR system has a limited resolution of $6.6\,cm^{-1}$, i.e. approximately the width of RB´$_2$.

Effects of intercalation of Ca atoms in α-V$_2$O$_5$: comparative studies

Following the same procedure as above, in this subsection we theoretically study the effect of intercalating Ca atoms, instead of Na, in the polaritonic activity of α-V$_2$O$_5$. As reported, the intercalated compound α'-CaV$_2$O$_5$ is isostructural with α'-NaV$_2$O$_5$ (*Pmmn* space group) [155, 157, 171, 172]. The lattice parameters are $a = 11.547$ Å, $b = 5.075$ Å and $c = 3.617$ Å (**Figure 4.10**), and the layer thickness expands to 4.389 Å. This is due to the atomic radius of Ca which is larger than the atomic radius of Na leading also to a longer distance between layers (b along the [010] crystal direction). Therefore, the Vanadium-Oxygen distances are also modified: the V-O$_v$ (vanadyl oxygen) distance increases up to 1.69 Å, the V-O$_b$ (bridge oxygen) distance (which retained the α-V$_2$O$_5$ bond length upon Na injection) increases to 1.95 Å, and the V-O$_c$ (chain oxygen) distances increase to 1.97 Å and 2.01 Å.
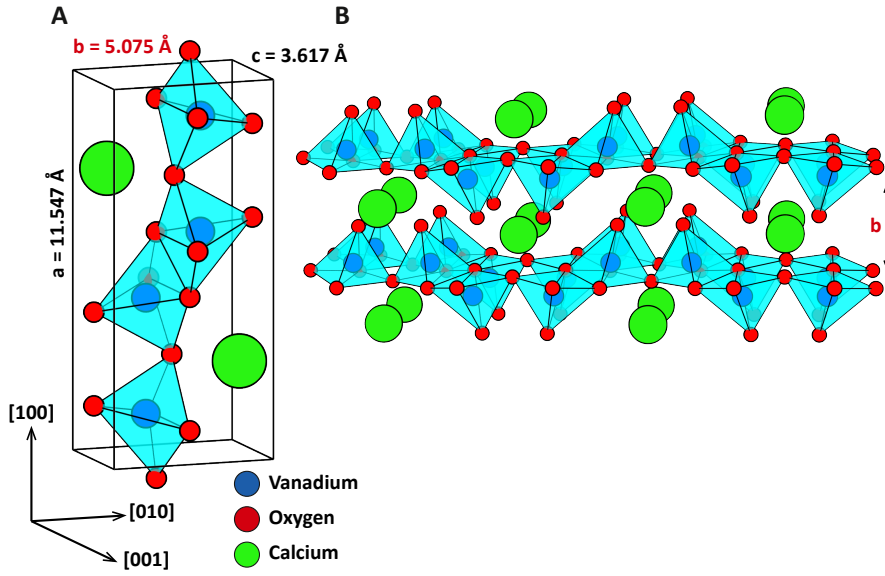
Figure 4.10: Crystal Structure of α'-CaV$_2$O$_5$ A Schematic of the α'-CaV$_2$O$_5$ unit cell. As in α-V$_2$O$_5$ and α'-NaV$_2$O$_5$, the unit cell consists of a periodic repetition of VO$_5$ distorted pyramids pointing alternatively up and down with the V atom (blue circles) in the center of the pyramid defined by the O atoms (red circles). Calcium atoms (green circles) are intercalated in the layered structure at certain positions. **B** Schematic of the layered structure of α'-CaV$_2$O$_5$.

In particular, the ω_{TO}, ω_{LO}, ε_∞ and γ parameters extracted from these calculations for the permittivity of α'-CaV$_2$O$_5$ are shown in **Table 4.2** (together with those previously extracted for α-V$_2$O$_5$ and α'-NaV$_2$O$_5$).

Figure 4.11 plots the calculated permittivity for α'-CaV$_2$O$_5$, α'-NaV$_2$O$_5$ and α-V$_2$O$_5$. Remarkably, the permittivity of α'-CaV$_2$O$_5$ also presents three RBs (referred to as RB"$_{1-3}$) each along a different crystal direction. They typically appear narrower and with their center shifted with respect to RB$_{1-3}$ in α-V$_2$O$_5$. For example, RB"$_1$ in α'-CaV$_2$O$_5$ (along the [010] crystal direction) is redshifted (about $143\,cm^{-1}$), RB"$_2$ is red-shifted ($44\,cm^{-1}$) and much narrower (from $174\,cm^{-1}$ to $15.4\,cm^{-1}$), and RB'$_3$ (in-plane hyperbolic in α-V$_2$O$_5$) is also ref-shifted ($96\,cm^{-1}$) and narrower (from $341\,cm^{-1}$ to $16.4\,cm^{-1}$). As a difference to RB"$_2$ and RB"$_3$, RB"$_1$ in α'-CaV$_2$O$_5$ resembles RB$_1$ and RB'$_1$ in α-V$_2$O$_5$ and α'-NaV$_2$O$_5$, respectively. However, in this case, RB"$_1$ is further shifted to low frequencies compared

Material	Axis	$\omega_{TO}\,(cm^{-1})$	$\omega_{LO}\,(cm^{-1})$	ε_{∞}	$\gamma\,(cm^{-1})$
α'-CaV$_2$O$_5$	[100]	805.4	820.7	40.24	0.7
	[010]	868.55	923.56	6.429	0.56
	[001]	536.2	557.2	22.54	9.6
α'-NaV$_2$O$_5$	[010]	946.82	982.1	8.969	0.56
	[001]	523.2	690.2	6.036	9.6
α-V$_2$O$_5$	[100]	770.0	944.3	6.559	8.1
	[010]	1004.4	1073.4	3.899	0.56
	[001]	474.4	815.6	6.142	9.6

Table 4.2: **Permittivity Parameters Calculated from First Principles** Parameters (for a Lorentz oscillators model) ω_{TO}, ω_{LO}, γ, and ε_{∞} for the phonon modes in α'-CaV$_2$O$_5$, α'-NaV$_2$O$_5$ and α-V$_2$O$_5$ extracted from *ab initio* calculations and perturbation theory.

to RB$_1$ and RB'$_1$, reaching a spectral distance from center to center of approximately $145\,cm^{-1}$ with respect to RB$_1$ in α-V$_2$O$_5$ and $70\,cm^{-1}$ with respect to RB'$_1$ in α'-NaV$_2$O$_5$. Note that the experimental frequency difference obtained between α-V$_2$O$_5$ and α'-NaV$_2$O$_5$ was approximately $30\,cm^{-1}$, while the theoretical difference is $\approx 55\,cm^{-1}$.

From these permittivities, we can plot the theoretical PhPs dispersions using the transfer matrix method[†] (**Figure 4.12**). We will focus our study in RB$_1$, RB'$_1$ and RB"$_1$, i.e., the RBs that emerge for the [010] crystal direction. The monotonic spectral shift of these RBs induced by the intercalation of atoms results in similar shifts of the PhPs dispersions, which are centered around $\omega_0 = 1040\,cm^{-1}$, $\omega_0 = 965\,cm^{-1}$ and $\omega_0 = 895\,cm^{-1}$ for PhPs in α-V$_2$O$_5$, α'-NaV$_2$O$_5$ and α'-CaV$_2$O$_5$, respectively. This effect clearly shows the great potential of intercalation (using different atoms) to tune the polaritonic dispersion in α-V$_2$O$_5$ over broad spectral ranges. The non-monotonic shift of the other RBs (also for the widths) along the [100] and [001] crystal axes (**Figure 4.11B**) indicate a more complex atomic interaction along these directions.

In principle, one could also consider intercalation of atoms according to atom content rather than just atom character, e.g. α'-Na$_x$V$_2$O$_5$ with $0 < x < 1$, as a way of tuning the polaritonic response of the material. However, it should be noted that different crystalline phases can be produced depending on the atom content. In fact, the symmetry of the unit cell can change dramatically giving rise to totally different space groups, even transforming the material into a non-van der Waals material [145, 154, 177, 178]. In this regard, further theoretical studies including DFT calculations will be necessary to predict the spectral positions of the IR active vibrations of the intercalated material and thus its Reststrahlen bands.

[†]The transfer matrix method is a matrix formalism that relates the incident electromagnetic field impinging on a stratified media with the reflected and transmitted field through the Fresnel reflection and transmission coefficients [173, 174, 175]. This formalism can predict the existence of polaritons since the polaritonic dispersion is contained in the poles of the reflection coefficients [21, 176].
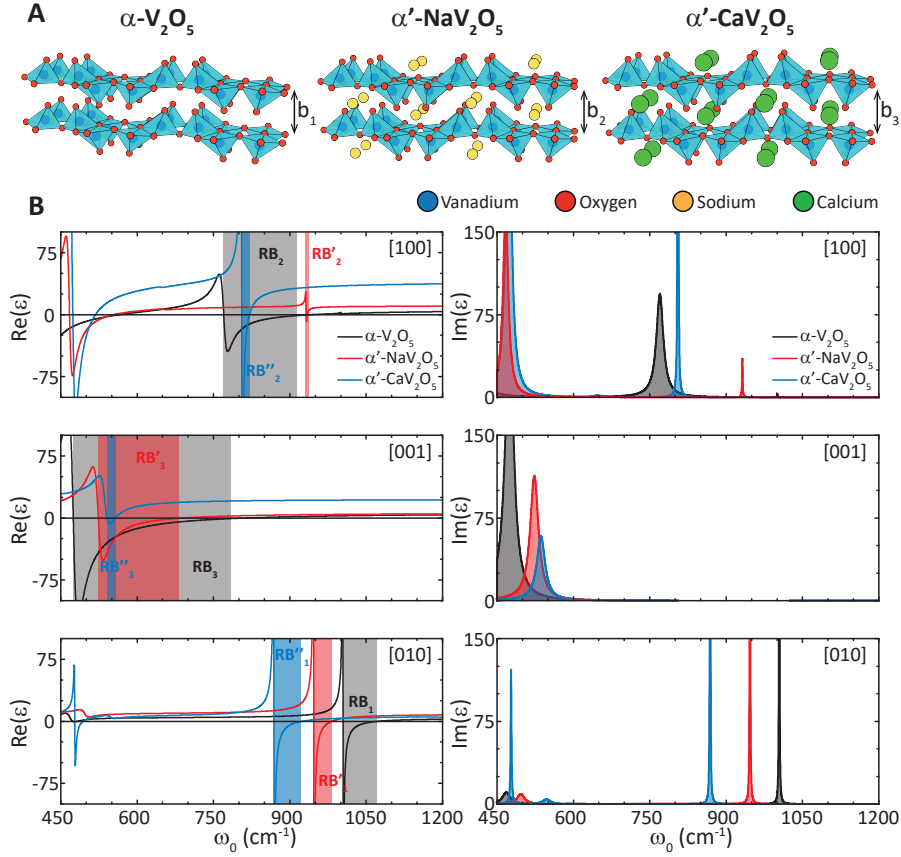
Figure 4.11: Permittivities of α-V$_2$O$_5$, α'-NaV$_2$O$_5$, and α'-CaV$_2$O$_5$ from First Principles A Illustration of the orthorhombic lattice structure of layered α-V$_2$O$_5$ (red spheres, oxygen atoms; blue spheres, vanadium atoms), α'-NaV$_2$O$_5$ (yellow spheres, sodium atoms), and α'-CaV$_2$O$_5$ (green spheres, calcium atoms). The orthorhombic structure of α-V$_2$O$_5$, α'-NaV$_2$O$_5$, and α'-CaV$_2$O$_5$ is based on bilayers of distorted VO$_5$ square pyramids stacked along the [010] direction - with interlayer distances $b_1 = 0.44\,nm$, $b_2 = 0.48\,nm$, $b_3 = 0.5\,nm$, respectively - via vdW interactions. **B** Real-part (left panels) and imaginary part (right panels) of the permittivities for α-V$_2$O$_5$ (black line), α'-NaV$_2$O$_5$ (red line), and α'-CaV$_2$O$_5$ (blue line) extracted from *ab initio* calculations along the principal [100], [010], and [001] axes (upper, middle, and lower panels, respectively). The Reststrahlen bands RB$_{1-3}$, RB'$_{1-3}$, RB"$_{1-3}$ for α-V$_2$O$_5$, α'-NaV$_2$O$_5$, and α'-CaV$_2$O$_5$ are indicated in black, red, and blue colors, respectively.

4.4 | Extracting the experimental dielectric permittivity of α-V$_2$O$_5$

To perform both numerical and analytical calculations of PhPs in α-V$_2$O$_5$, it is crucial to have an accurate dielectric function of the material. As mentioned in Section 4.1.2, the α-V$_2$O$_5$ dielectric function data available to date are presented in reference [150], which does not provide the value of ε_∞ for any crystallographic direction. Therefore, in this section a more accurate experimental dielectric function of α-V$_2$O$_5$ is extracted. For this purpose, we carry out a correlative study that combines experimentally extracted dispersions of PhPs in α-V$_2$O$_5$, DFT calculations (performed with the help of Dr. Ion Errea at Donostia International Physics Center (DIPC))
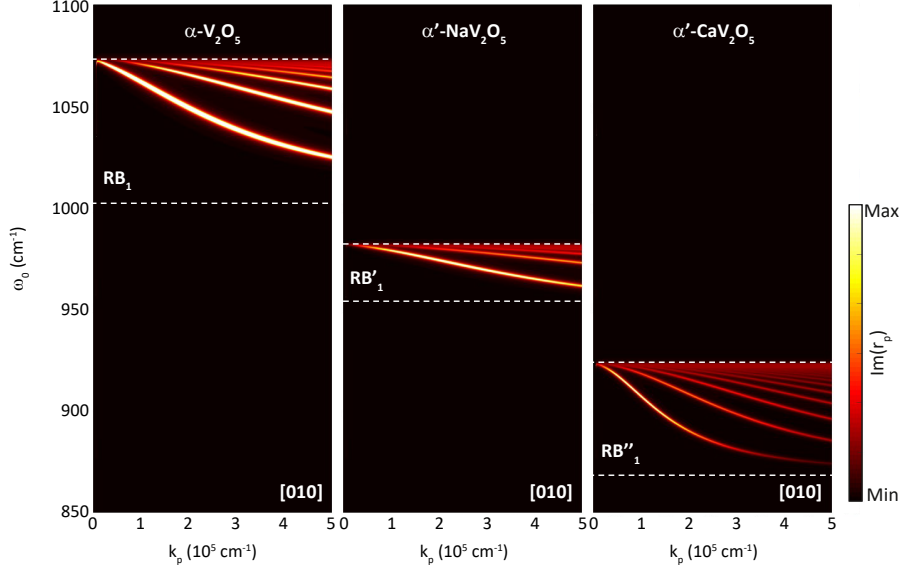
Figure 4.12: Dispersion of PhPs in α-V$_2$O$_5$, α'-NaV$_2$O$_5$, and α'-CaV$_2$O$_5$
Dispersion of PhPs along the [010] direction in RB$_1$ of α-V$_2$O$_5$, RB'$_1$ of α'-NaV$_2$O$_5$, and RB"$_1$ of α'-CaV$_2$O$_5$. Dashed lines indicate the TO an LO phonon frequencies calculated from first principles.

and transfer matrix calculations.

In particular, we extract the α-V$_2$O$_5$ dielectric function by considering the following correlative procedure: i) we use as a first guess the ε_i^∞ ($i =$[100], [010], [001]) values derived from ab initio calculations; ii) we extract the $\gamma_{TO/LO}$ parameters from the values reported in reference [150]; iii) we plot the PhPs dispersion curves employing the transfer matrix formalism using the the ω_i^{TO} and ω_i^{LO} values taken from reference [150], and iv) we fine-tune the calculated dispersions to fit the experimental points extracted from s-SNOM images (taken at discrete wavelengths along the [100] and [001] crystal directions on a $315\,nm$-thick α-V$_2$O$_5$ flake transferred on a BaF$_2$ substrate for RB$_1$, and on a $155\,nm$-thick α-V$_2$O$_5$ flake on a SiO$_2$ substrate for RB$_2$).

Figure 4.13 shows the calculated PhPs dispersion curves using the transfer matrix (color plots) [175] and analytical calculations (red lines) [142] for RB$_1$ of α-V$_2$O$_5$ (**Figure 4.13A**) along both the [100] (left panel) and [001] (right panel) crystal directions. The experimental results along both in-plane directions are superimposed in the figure (white dots) showing an excellent agreement with the theoretical calculations. Similar results are found for RB$_2$ of α-V$_2$O$_5$ (**Figure 4.13B**). The real part of the resulting dielectric function of α-V$_2$O$_5$ is presented in **Figure 4.14**, in good agreement with that in reference [150] (**Figure 4.2**). **Table 4.3** lists the extracted parameters (ω_{TO}, ω_{LO}, γ and ε_∞) of the permittivity assuming the same γ value for both TO and LO phonons.
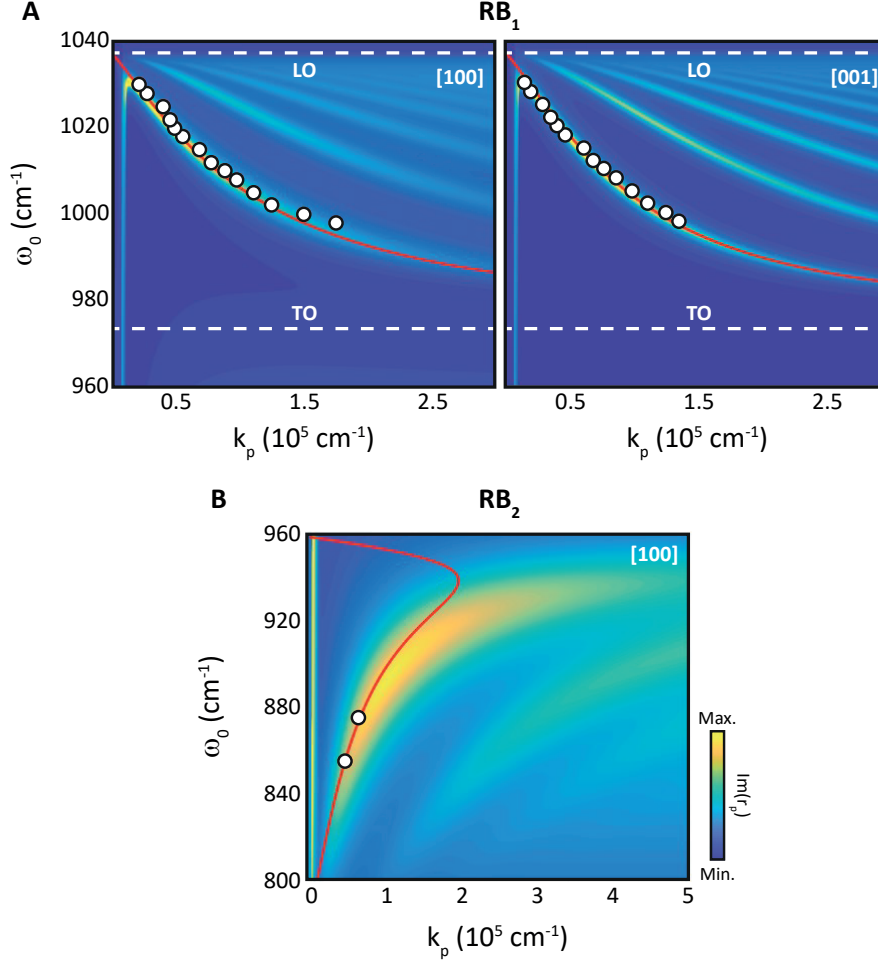
Figure 4.13: Dispersion of PhPs in α-V$_2$O$_5$ **A** Dispersion of PhPs in a $315\,nm$-thick α-V$_2$O$_5$ flake on a BaF$_2$ substrate along the [100] (left panel) and [001] (right panel) crystal directions. The false color plot represents the imaginary part of the Fresnel reflection coefficient [175],$\mathfrak{Im}(r_p(k_p, \omega_0))$. The analytically calculated dispersion curves are shown with red lines [142]. The experimental data extracted from monochromatic s-SNOM images are superimposed (white circles). **B** Dispersion of PhPs in a $155\,nm$-thick α-V$_2$O$_5$ flake on a SiO$_2$ substrate along the [100] crystal direction. The false color plot represents the imaginary part of the Fresnel reflection coefficient [175], $\mathfrak{Im}(r_p(k_p, \omega_0))$. The analytically calculated dispersion curves are shown with red lines [142]. The experimental data extracted from monochromatic s-SNOM images are superimposed (white circles).

Crystallographic Axes	$\omega_{TO}\,(cm^{-1})$	$\omega_{LO}\,(cm^{-1})$	$\gamma\,(cm^{-1})$	ε_∞
[100]	765	952	40	6.6
[010]	976	1037	2	3.9
[001]	506	842	19	6.1

Table 4.3: Extracted Parameters for the Permittivity Function of α-V$_2$O$_5$ α-V$_2$O$_5$ permittivity parameters along the [100], [010] and [001] crystal directions. The parameters are fitted by using DFT and transfer matrix calculations combined with experimentally extracted PhP dispersion curves.
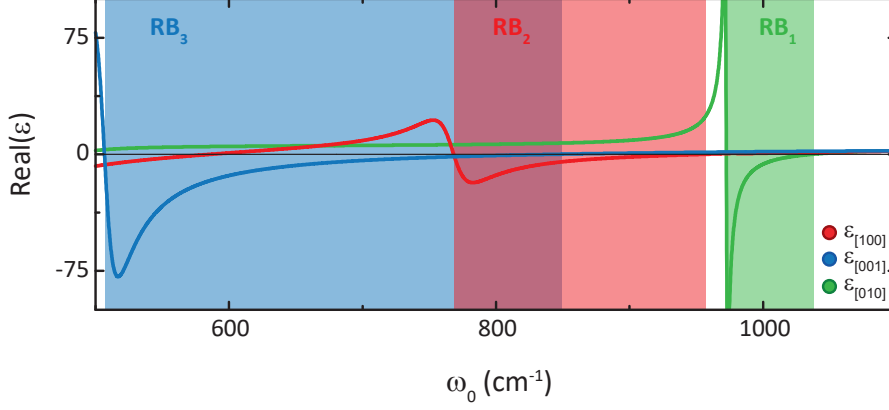
Figure 4.14: Extracted Permittivity of α-V$_2$O$_5$ Real part permittivity of α-V$_2$O$_5$ along the [100] (red curve), [010] (green curve) and [001] (blue curve) crystal directions. Colored regions indicate the frequency range for each RB.

4.5 | Lifetime and Quality Factor of PhPs in Pristine and Intercalated α-V$_2$O$_5$

Apart from extracting the dispersion of PhPs in α-V$_2$O$_5$ and intercalated α'-NaV$_2$O$_5$, we studied the PhPs lifetime in both crystals. This parameter is fundamental to validate intercalation as a suitable technological strategy to tune the spectral range of PhPs in vdW crystals. For this purpose, we fabricated gold nanoantennas (disks) on top of both crystals and performed near-field s-SNOM nanoimaging at frequencies within the RB$_1$s of each material, i.e. from $\omega_0 = 974\,cm^{-1}$ to $\omega_0 = 1040\,cm^{-1}$ in α-V$_2$O$_5$, and from $\omega_0 = 950\,cm^{-1}$ to $\omega_0 = 1012\,cm^{-1}$ for α'-NaV$_2$O$_5$. Due to its circular geometry, the Au disk acts as an efficient polaritonic launcher along all directions, enabling a direct visualization of the anisotropic propagation of PhPs. The s-SNOM images at frequencies $\omega_0 = 1010\,cm^{-1}$ in α-V$_2$O$_5$ and $\omega_0 = 973\,cm^{-1}$ in α'-NaV$_2$O$_5$ flakes (**Figure 4.15A**) reveal the propagation of PhPs along all in-plane directions leading to a nearly circular PhP wavefront. As such, these results indicate a similar in-plane elliptic propagation of PhPs in both vdW crystals. Note that the Au nanoantenna is not a good reflector for PhPs (due to their volume nature) so tip-launched PhPs can be neglected (no doublets are observed) [**103**].

To extract the PhPs lifetime, we first plot line profiles in the s-SNOM images along the [001] direction (dashed lines) and fit them (**Figure 4.15B**) with an exponentially decaying sine-wave function corrected by the geometrical spreading factor:

$$\xi(x) = \xi_0 + Ae^{-x/L_p}\sin\left(\frac{2\pi(x - x_0)}{\lambda}\right)\frac{1}{\sqrt{x}} \qquad (4.1)$$

where ξ is the s-SNOM amplitude signal, ξ_0 is a vertical offset, L_p is the polaritonic decay length, λ is the polariton wavelength and x_{c0} is an offset for the sine function. **Equation 4.1** allows us to extract the PhPs wavelength and decay length simultaneously. In contrast to **Equation 3.2** introduced in Chapter 3, **Equation 4.1** only considers polaritons launched with λ_p periodicity, i.e. only considers PhPs launched by the nanoantenna. Furthermore, since polaritons excited by a gold disk propagate as circular waves, a $1/\sqrt{x}$ geometrical factor is used instead of the $1/x$ factor typically used for edge-launched polaritons. The extracted PhPs decay lengths

are $L_p = 1.40\,\mu m$ for α-V$_2$O$_5$ at $\omega_0 = 1010\,cm^{-1}$ and $L_p = 1.15\,\mu m$ for α'-NaV$_2$O$_5$ at $\omega_0 = 973\,cm^{-1}$. On the other hand, the extracted dispersion and numerically calculated group velocities of PhPs in both materials are shown in **Figure 4.16** for a clear comparison. A group velocity $v_g = 7.3 \cdot 10^{-4}\,c$ was found for α-V$_2$O$_5$ at $\omega_0 = 1010\,cm^{-1}$ while $v_g = 6.7 \cdot 10^{-4}\,c$ was found for α'-NaV$_2$O$_5$ at $\omega_0 = 973\,cm^{-1}$, with c the speed of light. Note that these values of v_g are an order of magnitude lower than those reported for α-MoO$_3$ in Section 3.3 and two orders of magnitude lower than those reported for PhPs in h-BN. With these values, and according to $\tau = L_p/v_g$, we obtain PhPs lifetimes of $\tau_{[001]} = 6 \pm 1\,ps$ for PhPs in α-V$_2$O$_5$ at $\omega_0 = 1010\,cm^{-1}$ and $\tau_{[001]} = 4 \pm 1\,ps$ for PhPs in α'-NaV$_2$O$_5$ at $\omega_0 = 973\,cm^{-1}$ (**Figure 4.15B**). These long lifetimes (similar to PhPs in MoO$_3$, as shown in Chapter 3, and doubling the values reported for isotopically pure h-BN) reveal the low-loss nature of PhPs in α-V$_2$O$_5$, which can be attributed to the fact that both V and O natural abundances are close to be isotopic pure ($\approx 99.7\%$) [71]. More importantly, they demonstrate that apart from allowing large spectral shifts, intercalation allows preserving the crystal quality and the excitation of ultra-low-loss PhPs.
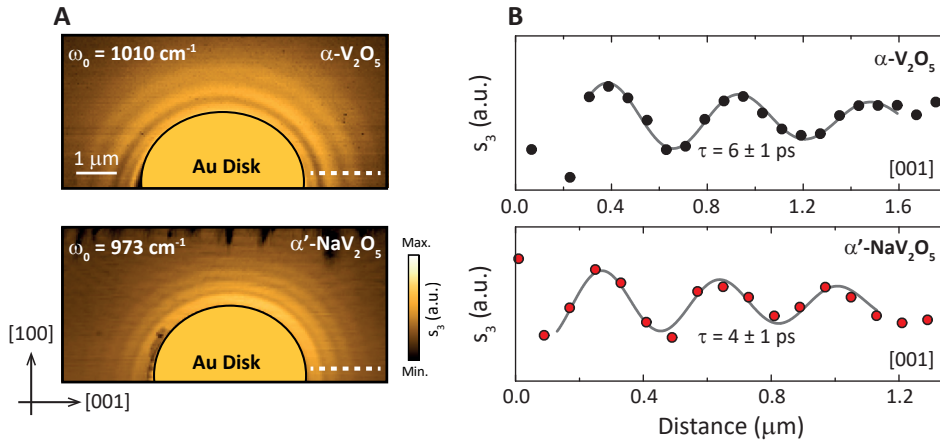
Figure 4.15: Anisotropy and Lifetimes of PhPs in α-V$_2$O$_5$ and Intercalated α'-NaV$_2$O$_5$ Flakes **A** Near-field amplitude images s_3 of α-V$_2$O$_5$ (upper panel) and α'-NaV$_2$O$_5$ (bottom panel) flakes with thicknesses $d = 130\,nm$ and $d = 107\,nm$ at illuminating frequencies $\omega_0 = 1010\,cm^{-1}$ (RB$_1$) and $\omega_0 = 973\,cm^{-1}$ (RB'$_1$). A gold disk (half of it shown in the image for convenience) is used as a nanoantenna for efficient launching of PhPs along all in-plane directions. **B** s-SNOM line traces indicated by white dashed lines in **A**. Damped sine-wave functions (black solid lines) were fitted to the data. Lifetimes of $\tau = 6 \pm 1\,ps$ and $\tau = 4 \pm 1\,ps$ are obtained for PhPs in α-V$_2$O$_5$ and α'-NaV$_2$O$_5$, respectively.

Finally, the PhP quality factor $Q = \Re\mathrm{e}(k_p)/\Im\mathrm{m}(k_p)$ (also known simply as Figure of Merit, FOM) is an adequate quantity to evaluate the polaritonic propagation properties as it indicates their number of oscillations relative to their propagation length. Specifically, they represent how many wavelengths PhPs propagate before their amplitude decays $1/e$. Consequently, high quality factors are needed for applications where polaritonic signals need to travel far away from the polaritonic launcher. Note that due to the extremely small group velocity of PhPs in the RB$_1$ of α-V$_2$O$_5$ and RB'$_1$ of α'-NaV$_2$O$_5$ the expected Q values are low. To calculate them, we Fourier transform the experimentally extracted polaritonic profiles (shown in **Figure 4.15B**) into the spatial-frequency domain and fit the resulting curves with a Lorentzian function [103]. The Lorentzian maximum frequency accounts for
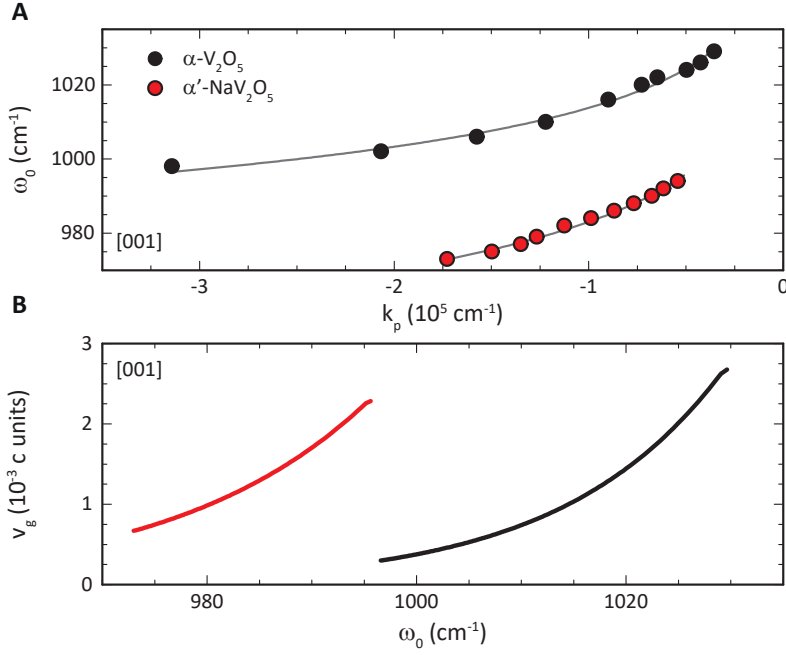
Figure 4.16: Dispersion and Group Velocity of PhPs in α-V$_2$O$_5$ and α'-NaV$_2$O$_5$ **A** PhPs dispersion curves for α-V$_2$O$_5$ (black symbols) and α'-NaV$_2$O$_5$ (red symbols) extracted from near-field line profiles along the [001] direction. Gray lines are fits using a potential function. **B** Group velocities, v_g, of PhPs along the [001] direction of α-V$_2$O$_5$ (black line) and α'-NaV$_2$O$_5$ (red line). The thicknesses of the flakes are $130\,nm$ and $107\,nm$ for α-V$_2$O$_5$ and α'-NaV$_2$O$_5$, respectively.

the real part of the polaritonic wavevector, $\mathfrak{Re}(k_p)$, while the half-width at half-maximum represents the imaginary part of the polaritonic wavevector, $\mathfrak{Im}(k_p)$. We obtain Q values of 3.5 and 2.5 for PhPs in α-V$_2$O$_5$ and α'-NaV$_2$O$_5$, respectively (**Figure 4.17**). We note that these values are much smaller than those reported for PhPs in h-BN ($Q \approx 20$) [71], which is attributed to the extremely slow group velocities of PhPs in α-V$_2$O$_5$ and α'-NaV$_2$O$_5$.

4.6 | Conclusions

In this chapter, we introduced α-V$_2$O$_5$ as a van der Waals material supporting highly-confined PhPs. Specifically, PhPs can be excited in this material within three different Reststrahlen bands (RB$_{1-3}$) in the MIR spectral range, one along each crystallographic direction. By performing s-SNOM nanoimaging we revealed the anisotropic propagation of these PhPs, with in-plane elliptic propagation in RB$_1$ (along the [010] crystal direction) and in-plane hyperbolic propagation in RB$_2$ (along the [100] crystal direction). Moreover, with the help of DFT and transfer matrix calculations, we have extracted an accurate permittivity of α-V$_2$O$_5$ that reproduces our experimental observations.

More importantly, we demonstrate that the α-V$_2$O$_5$ crystal structure can be intercalated with alkaline atoms, opening the door to tailor the physical properties of the material. In fact, by intercalating Na atoms in α-V$_2$O$_5$ crystals we observe by nanoFTIR measurements a remarkable shift of RB$_1$ (from center to center) of about $30\,cm^{-1}$. This result establishes intercalation as an effective way to tune the
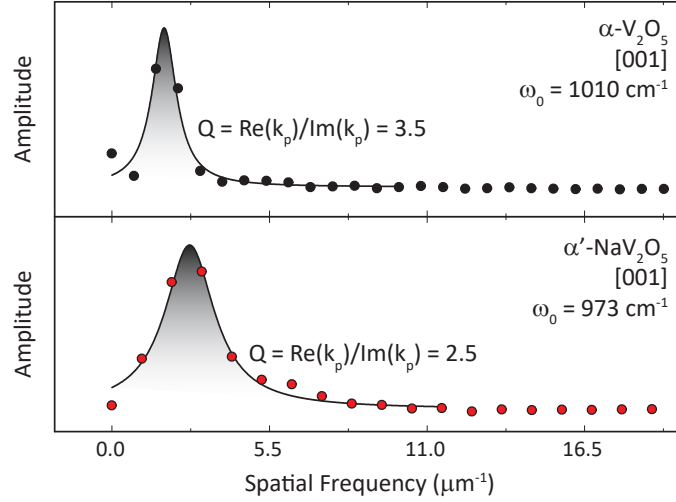
Figure 4.17: Analysis of the Propagation Damping of PhPs The symbols show the FFT of the line profiles showed in **Figure 4.15** for α-V_2O_5 (upper panel) and α'-NaV_2O_5 (bottom panel). Black lines represent fittings to a Lorentzian curve. The figure of merit $Q = \Re(k_p)/\Im(k_p)$ is calculated from the HWHM of the Lorentzian fit.

frequency range within which PhPs can be excited in a van der Walls material. Interestingly, intercalation can be achieved employing atoms of different nature, as we have shown theoretically for the case of Ca atoms in α-V_2O_5.

Finally, to fully validate intercalation as a suitable technological strategy in nanooptics, we extracted the lifetimes of PhPs in α-V_2O_5 and compared them with those in the intercalated compound α'-NaV_2O_5. Lifetimes of $\tau = 6 \pm 1\,ps$ and $\tau = 4 \pm 1\,ps$ were obtained for α-V_2O_5 and the intercalated α'-NaV_2O_5 crystal, respectively. These long lifetimes (of the same order of magnitude than the best values reported to date) corroborate that our intercalation method preserves the optical quality of the crystal and thus is an optimal strategy to spectrally manipulate PhPs in a layered crystal [**42, 179**]. Regarding the PhPs quality factors ($Q = \Re(k_p)/\Im(k_p)$), relevant for describing the propagation properties of polaritons, we obtained values of $Q = 3.5$ and $Q = 2.5$ for PhPs in α-V_2O_5 and α'-NaV_2O_5, respectively. Although these values are smaller than others reported for PhPs, they only reflect the ultra-low polaritonic group velocity in α-V_2O_5 and α'-NaV_2O_5.

5

Damping mechanisms and Fundamental Limits of Hyperbolic PhPs in α-MoO$_3$

In this chapter, the ultimate limits of the main polaritonic properties of PhPs in α-MoO$_3$ are analyzed. For this purpose, the damping mechanisms of PhPs as a function of temperature are studied both from a theoretical point of view (by ab initio calculations) and experimentally (by FTIR and s-SNOM measurements at cryogenic temperatures). As a result, polaritonic dispersions, group velocities, propagation lengths, lifetimes are calculated both experimentally and theoretically at low temperatures. Interestingly, record-high lifetimes are found.

5.1 | Introduction

During this thesis, it has been shown that hyperbolic PhPs in biaxial media, such as α-MoO$_3$ or α-V$_2$O$_5$, are very promising to squeeze and control infrared light into nanoscale volumes with ultra-low losses. However, to envision potential applications, a study on the ultimate limits of the main PhPs properties, such as their propagation length and lifetime, is of crucial importance. Typically, such properties depend on fundamental mechanisms related to dissipation, such as e.g. scattering processes, which are typically enhanced at room temperature [64, 180]. Therefore, to elucidate the role of such mechanisms, it is very useful to measure the PhPs propagation lengths and lifetimes as a function of temperature. Moreover, DFT calculations are an extremely powerful tool to predict the temperature dependence of the physical properties of a material and, in particular, to predict its vibrational resonances intimately related to the polaritonic properties. In fact, DFT calculations have recently been applied to h-BN [181], α-MoO$_3$ [131], α-V$_2$O$_5$ [42, 149] and α'-NaV$_2$O$_5$ [42, 182] to predict their phonon spectra. In this chapter, we present a fundamental study on the damping mechanisms of PhPs in α-MoO$_3$. For this purpose, we combine first principles calculations with experimental FTIR and s-SNOM measurements as a function of temperature (from room temperature to cryogenic temperatures) [183, 184, 185].

5.2 | Far-Field Characterization of α-MoO$_3$ at Low Temperatures

Since PhPs arise from the coupling between photons and phonons (see chapter 1), we start our fundamental study by exploring how the phonons spectra in α-MoO$_3$ varies with temperature. To do so, we carry out far-field reflectance measurements of a thick α-MoO$_3$ flake (thickness$> 1\,\mu m$) using an FTIR system equipped with a cryostat (a closed-cycle He cryostat capable of being cooled to $5\,K$). **Figure 5.1A** shows the resulting FTIR reflection spectra when polarizing the incident illumination along both in-plane directions ([100] and [001], top and bottom panels, respectively) at $5\,K$ (blue lines) and $300\,K$ (red curves) (all measurements are normalized to gold). The spectra show a high reflectivity band for both in-plane polarizations and temperatures, which can be assigned to the RBs along the [100] direction (from approximately $820\,cm^{-1}$ to $970\,cm^{-1}$) and the [001] direction (from approximately $545\,cm^{-1}$ to $851\,cm^{-1}$), in agreement with the FTIR measurements at RT in **Figure 3.2**. In addition, a narrow band (basically a peak) is found around $1007\,cm^{-1}$, indicating the presence of a third RB along the [010] direction (from approximately $960\,cm^{-1}$ to $1010\,cm^{-1}$). This RB can be observed due to the oblique incidence of light on the sample. Importantly, we observe that the RBs are slightly broader at $5\,K$, meaning that the TO and LO phonons are shifting spectrally with temperature.
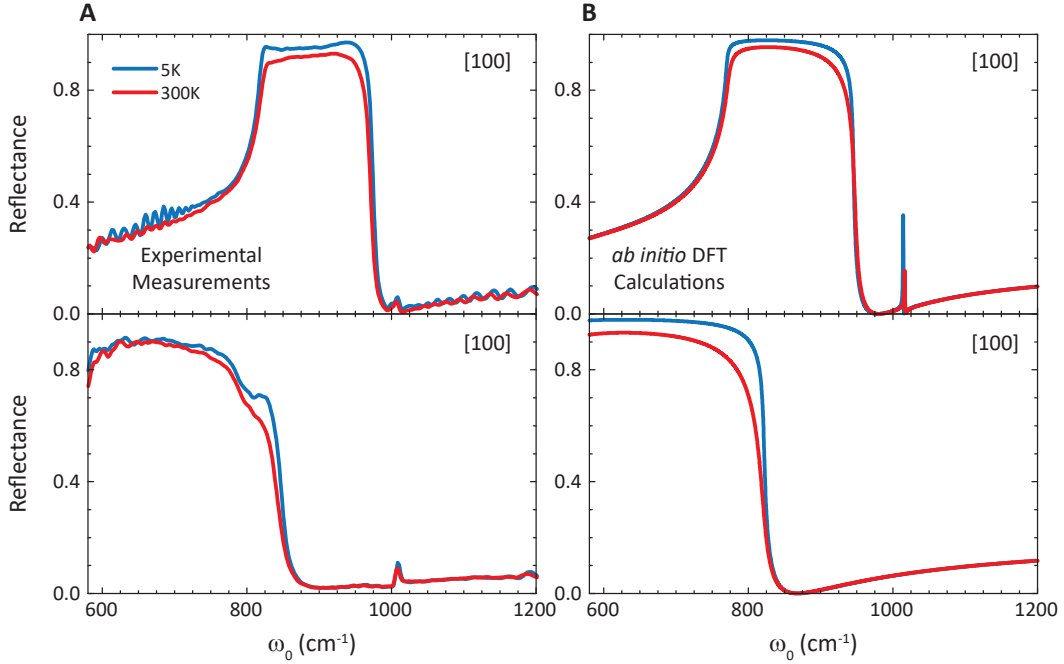
Figure 5.1: Experimental and Theoretical (ab initio) FTIR Reflectivity of α-MoO$_3$ A FTIR reflectance spectra of an α-MoO$_3$ flake along the [100] (top panel) and [001] (bottom panel) in-plane directions. **B** Reflectance spectra of α-MoO$_3$ calculated by first principles along the [100] (top panel) and [001] (bottom panel) in-plane directions.

To better understand these experimental FTIR spectra, we performed ab initio DFT calculations (in collaboration with Ion Errea at DIPC) considering semi-local exchange-correlation functionals [169]. The calculations include 6 valence electrons for O and 14 valence electrons for Mo. The experimental lattice parameters are em-

ployed with internal relaxation of the atomic positions, and the phonon frequencies, polarization vectors, effective charges and high-frequency limit of the dielectric function are calculated making use of density functional perturbation theory (DFPT). From these calculations, the dielectric function of α-MoO$_3$ is extracted as a function of temperature employing perturbation theory that considers three-phonon anharmonic interactions for the phonon lifetime (determined by the possible decay of a phonon mode into two other phonons) [186]. Once extracted the permittivity, the *ab initio* reflectivity is computed through:

$$R_i(\omega_0) = \left| \frac{\sqrt{\varepsilon_i(\omega_0)} - 1}{\sqrt{\varepsilon_i(\omega_0)} + 1} \right|^2 \; ; \; i = [100], [010], [001] \tag{5.1}$$

where $\varepsilon_i(\omega_0)$ is the permittivity along the i direction. The spectra obtained (**Figure 5.1B**) are in good agreement with the experimental FTIR measurements, correctly predicting the presence of different RBs that slightly shift with the temperature. A slight spectral displacement of the calculated RBs with respect to the experiment is also observed. However, this shift is within the assumed range of agreement for the phonon frequencies when using semilocal approximations of the exchange and correlation in oxides [131]. It should be noted that, for these first principles calculations, only those terms have been considered which have a contribution to the phonon lifetime (or equivalently, to the phonon resonance linewidth) at the lowest order in perturbation theory. As such, thermal expansion of the unit cell and effects related to the interaction of four or more phonons are discarded. In other words, only three-phonon interactions (two-phonon collision to form another phonon or the annihilation of a phonon to form two phonons) are considered. Other effects such as electron-phonon interactions are also ignored as its contribution is not dominant in high bandgap semiconductor such as α-MoO$_3$ ($\approx 3\,eV$) [127]. The effect of these discarded contributions is only related to corrections to the phonon shifts, which can explain the displacement of RBs observed between theory and experiment. Another consequence of these approximations taken in our calculations is that the only temperature-dependent parameter considered is the thermal occupation of the phonon modes (see below).

To quantify the spectral shift of the α-MoO$_3$ TO phonon with temperature observed in the reflectance spectra in **Figure 5.1A**, we model the α-MoO$_3$ permittivity tensor, $\hat{\varepsilon} = \text{diag}(\varepsilon_x, \varepsilon_y, \varepsilon_z)$, using a three parameter Drude-Lorentz oscillator function:

$$\varepsilon_i(\omega) = \sum_{k=1}^{N} \frac{\omega_{p,k,i}^2}{\omega_{TO,k,i}^2 - \omega^2 - i\gamma_{k,i}\omega} \tag{5.2}$$

where $\varepsilon_i(\omega)$ indicates the frequency-dependent i-th component of the permittivity, ε_∞ the high-frequency permittivity, $\omega_{p,k,i}$ and $\omega_{TO,k,i}$ the 'plasma' and TO phonon frequencies along the direction i, respectively, $\gamma_{k,i}$ the scattering rate along the direction i, and k the number of oscillators used for each crystal direction (in this case, 1). From this first permittivity function (setting seed parameters), we extract the reflectance spectrum (see Section 2.2) and compare it with the experimental one. Following this procedure iteratively until the two reflectance spectra match, we can extract an accurate permittivity function. **Figure 5.2** shows the resulting phonon parameters following the procedure explained above (red symbols). The experimental values obtained using light polarized along the [100] direction are also plotted

81

(black symbols). Although spectral shifts between experiment and theory are not directly comparable (because of the contributions not considered in our DFT calculations, as commented above), the increase/decrease ratio (i.e. the slope) of the different phonon parameters with temperature can be compared. In particular, ω_{TO} shows the same trend/slope: an increase of temperature from $5\,K$ to $300\,K$ yields about $3\,cm^{-1}$ hardening in ω_{TO} in both cases (**Figure 5.2A**). This result supports the validity of our theoretical calculations.

The extracted temperature dependence of the phonon scattering rate, γ, and the phonon lifetime, τ, are also shown in **Figure 5.2B** and **Figure 5.2C**, respectively. Although the experimental points present some fluctuations, especially at low temperatures due to the technical difficulties to precisely control the temperature in the cryostat, the trend observed for γ and τ is again the same in both experimental and theory, with a difference between the values at $300\,K$ of only $1.5\,cm^{-1}$ and $1.3\,ps$ for γ and τ, respectively. These differences can be explained by the fact that only anharmonic phonon processes are considered (impurities are discarded as a possible scattering channel) in the DFT calculations, which leads to a decrease of the theoretical losses, i.e. to an increase of the theoretical lifetimes. On the other hand, the relatively good agreement between experimental and theoretical calculations reveals that the observed increase in phonon lifetime at lower temperatures can be explained by considering only anharmonic processes.
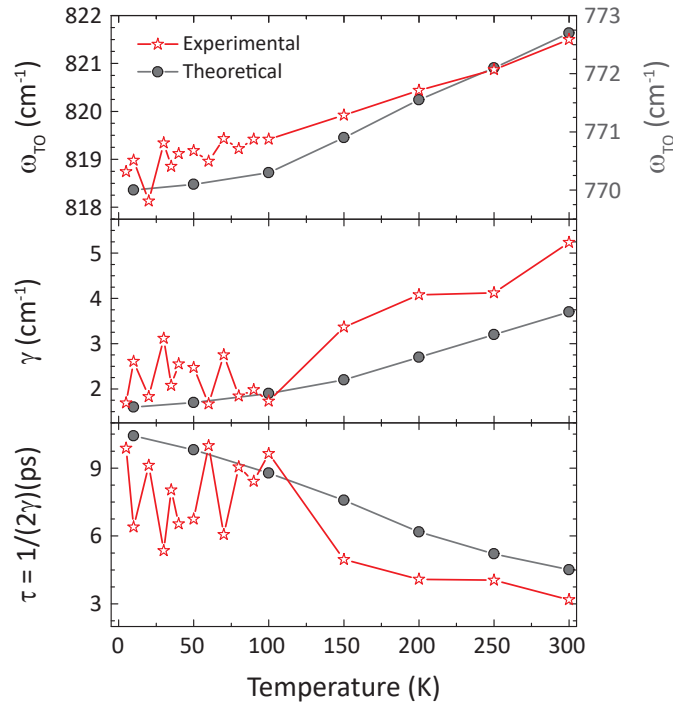
Figure 5.2: Comparison Between Experimental and Theoretical Phonon Parameters in α-MoO$_3$ **A** Experimental and theoretical ω_{TO} values. Both experimental and theoretical values follow the same trend. **B** Comparison between the experimentally extracted and theoretically calculated α-MoO$_3$ phonon linewidth, γ, for the phonon resonance along the [100] direction. **C** Comparison between the experimentally extracted and theoretically calculated α-MoO$_3$ phonon lifetime, $\tau = 1/(2\gamma)$, for the phonon along the [100] direction.

It is worth mentioning, that as previously noted, the only temperature dependence in the ab initio calculations stems from the thermal occupation of the phonon modes, which affects the possible decay of the TO phonon into lower energy modes. Hence, the reduction of the scattering rate of the TO mode can be attributed to a lower occupation of low energy modes, in line with the phenomenological results reported in reference [**187**].

5.3 | Near-Field Characterization of PhPs in α-MoO$_3$ at Low Temperatures

To further study the damping mechanisms of PhPs in α-MoO$_3$, we measure the propagation of PhPs in α-MoO$_3$ as a function of temperature using a cryo s-SNOM system (Neaspec GmbH). The principle of operation of this system is analogous to the one presented in Section 2.3, although the architecture of the setup is completely different. In particular, the main difference is that the tip and the sample are isolated in a vacuum chamber where the temperature can be cooled down to approximately $8\,K$. The resulting s-SNOM images taken on a $104\,nm$-thick α-MoO$_3$ flake exfoliated on SiO$_2$ at an illuminating frequency of $880\,cm^{-1}$, i.e. within the hyperbolic RB (L-RB), and for temperatures ranging from $225\,K$ to $10\,K$ are shown in **Figure 5.3A**. We observe typical oscillating fringes that are parallel to only one of the flake edges, revealing the propagation of PhPs along the [100] crystal direction. By extracting a line profile along the [100] crystal direction in these images (**Figure 5.3B** corresponding to the profile indicated by white dashed lines in **Figure 5.3A**), we clearly observe the existence of two polaritonic contributions (giving rise to signal doublets) showing different periodicities. As mentioned in Section 3.2, tip-excited and edge-launched PhPs can coexist in α-MoO$_3$ giving rise to fringe oscillations with $\lambda_p/2$ and λ_p periodicities. Such polaritonic profile can be well modeled using the following equation:

$$y(x) = y_0 + A_1 e^{-x/L_p} \sin\left(\frac{2\pi(x-x_1)}{\lambda}\right)\frac{1}{x} + A_2 e^{-2x/L_p}\sin\left(\frac{4\pi(x-x_2)}{\lambda}\right)\frac{1}{\sqrt{x}} \quad (5.3)$$

where y is the near-field overall intensity, y_0 a vertical offset, A_1 is the amplitude of the edge-launched wave, A_2 is the amplitude of the tip-launched wave, L_p is the polariton propagation length, λ_p is the polariton wavelength, and x_1 and x_2 are phase offsets, respectively. The geometrical terms $1/x$ and $1/\sqrt{x}$ account for the plane-wave nature of edge-launched polaritons and the circular-wave nature of the tip-excited polaritons, respectively.

Figure 5.4 shows the experimentally extracted PhPs wavelength, λ_p, and group velocity, $\vec{v}_g = \nabla_{\vec{k}}\omega_0(\vec{k}_p)$, as a function of incident frequency and temperature ($225\,K$, (red curve), $150\,K$ (orange curve), $90\,K$ (green curve) and $10\,K$ (blue curve)) for both RBs (U-RB and L-RB). λ_p was directly obtained by fitting the near-field profiles (as those shown in **Figure 5.3B**) with **Eq. 5.3**. On the other hand, v_g was calculated by fitting the PhPs dispersion to a potential function and performing its numerical derivative.

With respect to λ_p, we observe an increase/decrease as a function of frequency for the elliptic/hyperbolic RB, indicating a negative/positive phase velocity, as previously shown in Section 3.2 In terms of temperature dependence, we observe a
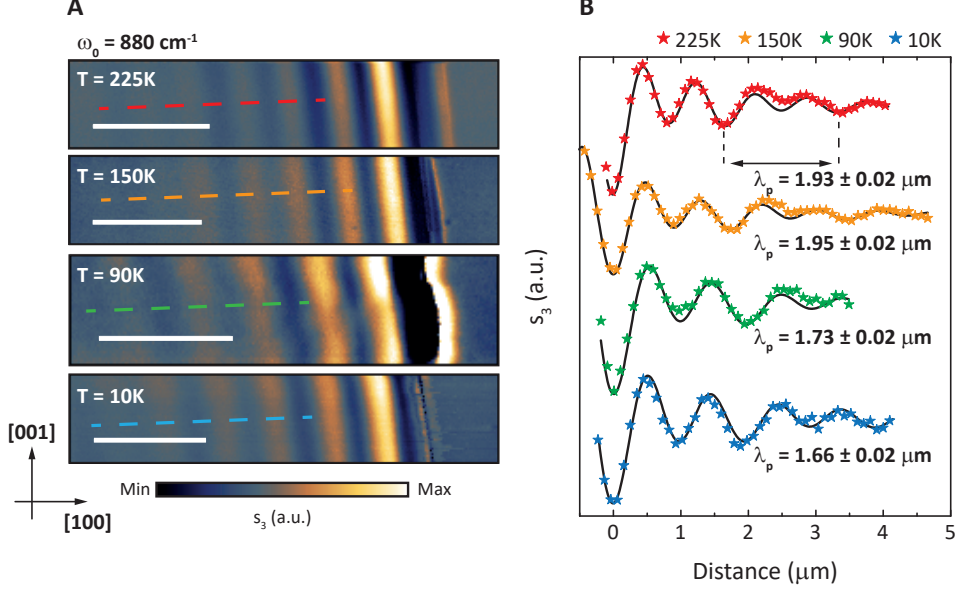
Figure 5.3: Experimental s-SNOM Measurements of PhPs in α-MoO$_3$ at Cryogenic Temperatures **A** s-SNOM images taken in a $102\,nm$-thick α-MoO$_3$ flake at an illuminating frequency of $880\,cm^{-1)}$ and temperatures $225\,K$, $150\,K$, $90\,K$ and $10\,K$. The α-MoO$_3$ crystal directions are shown at the bottom left. The scale bar is $2\,\mu m$ in all images. **B** Near-field amplitude profiles extracted along the colored dashed lines in **A**. Fittings using **Eq. 5.3** are shown as black curves.

different behavior in the two RBs, while a modest increase (around 15% in average) is observed in the hyperbolic regime when decreasing the temperature from $225\,K$ to $10\,K$ (**Figure 5.4A**), no discernible changes are appreciated in the elliptic regime (**Figure 5.4B**). With respect to v_g, we observe extremely small values at all temperatures in both RBs (**Figure 5.4C** for the L-RB and **Figure 5.4D** for the U-RB), in consistency with the results shown in Section 3.3.2. For example, in the L-RB we calculate a group velocity of $v_g = 1.9 \cdot 10^6\,m/s$, corresponding to $6.5 \cdot 10^{-3}\,c$ with c the speed of light, at $\omega_0 = 895\,cm^{-1}$ and $T = 10K$. In the U-RB, we obtain values of $2.5 \cdot 10^5\,m/s = 8.6 \cdot 10^{-4}\,c$ at $\omega_0 = 988\,cm^{-1}$ and $10\,K$. Due to the differences in the polariton wavelengths in the hyperbolic band (L-RB) as a function of temperature (**Figure 5.4A**), the group velocities in this RB are also different, with higher values for lower temperatures (**Figure 5.4C**). The group velocities in the elliptic regime are almost the same as a function of temperature (**Figure 5.4D**).

Theoretically, PhPs wavelengths and group velocities can be calculated using the theoretical dispersion relation for electromagnetic modes in biaxial slabs embedded between two isotropic media [142]:

$$k_p = \frac{\rho}{d}\left[\arctan\left(\frac{\varepsilon_1\rho}{\varepsilon_z}\right) + \arctan\left(\frac{\varepsilon_3\rho}{\varepsilon_z}\right) + \pi l\right]; l = \in \mathbb{R} \tag{5.4}$$

where k_p is the in-plane PhPs wavenumber, d is the α-MoO$_3$ flake thickness, ε_1 and ε_3 are the permittivities of the superstrate (air) and substrate (SiO$_2$), respectively, $\rho = i\sqrt{\varepsilon_z/(\varepsilon_x \cos^2\beta + \varepsilon_y \sin^2\beta)}$ with ε_x, ε_y and ε_z the material permittivity and β the angle between the [100] axis and the in-plane component of the wavevector. In particular, the PhPs wavelength is calculated as $\lambda_p = 2\pi/\mathfrak{Re}(k_p)$ while the
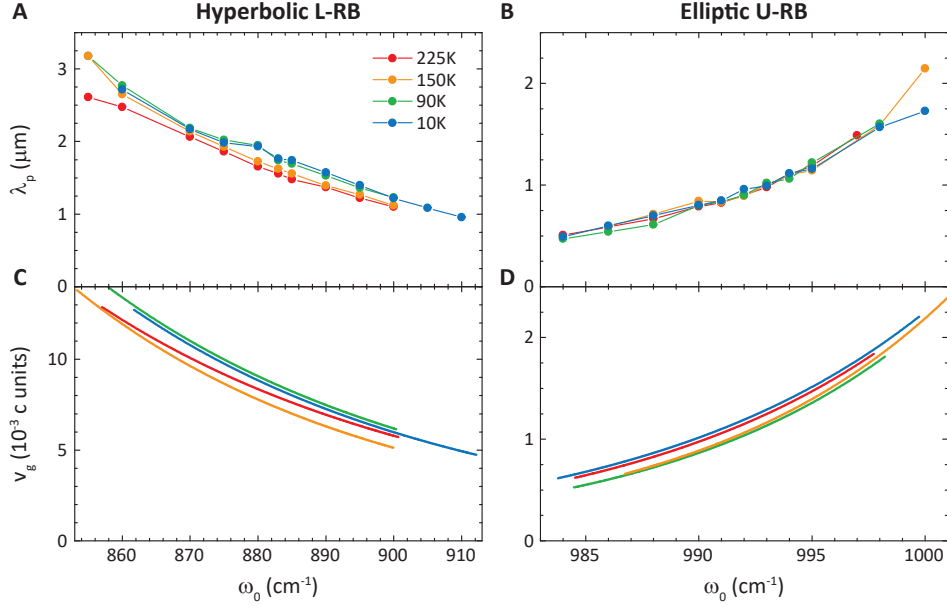
Figure 5.4: Experimental Temperature Dependence of the Wavelength and Group Velocity of PhPs in α-MoO$_3$ **A, B** PhPs wavelength in α-MoO$_3$ as a function of the incident frequency for temperatures from 10 to 225 K within the hyperbolic (**A**) and elliptic (**B**) RBs. **C, D** PhPs group velocity in α-MoO$_3$ as a function of the illuminating frequency for the hyperbolic (**C**) and elliptic (**D**) RBs for temperatures from 10 to 225 K.

group velocity is extracted by performing the numerical derivative of $\omega_0(k_p)$. The as-calculated λ_p and v_g are shown in **Figure 5.5** for temperatures ranging from 300 K (red curve) to 10 K (blue curve). They show a good qualitative agreement with the experimental results shown in **Figure 5.4**. We note that in analogy to the results shown in Section 5.2, the theoretical values of λ_p and v_g (as a difference to their trends/slopes) are not directly comparable to the experimental results due to the intrinsic frequency shifts obtained in DFT calculations.

We will focus now on the PhPs propagation length as a function of temperature as the information about the damping mechanisms is encoded into it. The experimental propagation lengths are extracted by fitting s-SNOM near-field profiles (see **Figure 5.3B**) with **Equation 5.3**. The theoretical values are obtained by taking the inverse of the imaginary part of the PhPs wavenumber $(1/\mathfrak{Im}(k_p))$ given by **Equation 5.4**. **Figure 5.6** plots both the experimental (**Figure 5.6A** for the L-RB and **Figure 5.6B** for the U-RB) and theoretical (**Figure 5.6C** for the L-RB and **Figure 5.6D** for the U-RB) results obtained. In all cases we observe the longest propagation length for the lowest temperature. However, in terms of frequency dependence, the longest propagation lengths are obtained in the proximities of ω_{TO} for the hyperbolic regime and in the proximities of ω_{LO} for the elliptic regime (due to its negative phase velocity). Both, experimentally and theoretically, we find an average enhancement in the PhPs propagation length when decreasing the temperature. In the experiment this enhancement is of about 30% in the L-RB and of about 50% in the U-RB when decreasing the temperature from 225 K to 10 K. **Table 5.1** shows a detailed comparison of the enhancement of the propagation length when decreasing the temperature from 225 K to 10 K ($\Delta L_p(\%) = 100 \cdot [L_p(10\,K) - L_p(225\,K)]/L_p(225\,K)$) for two
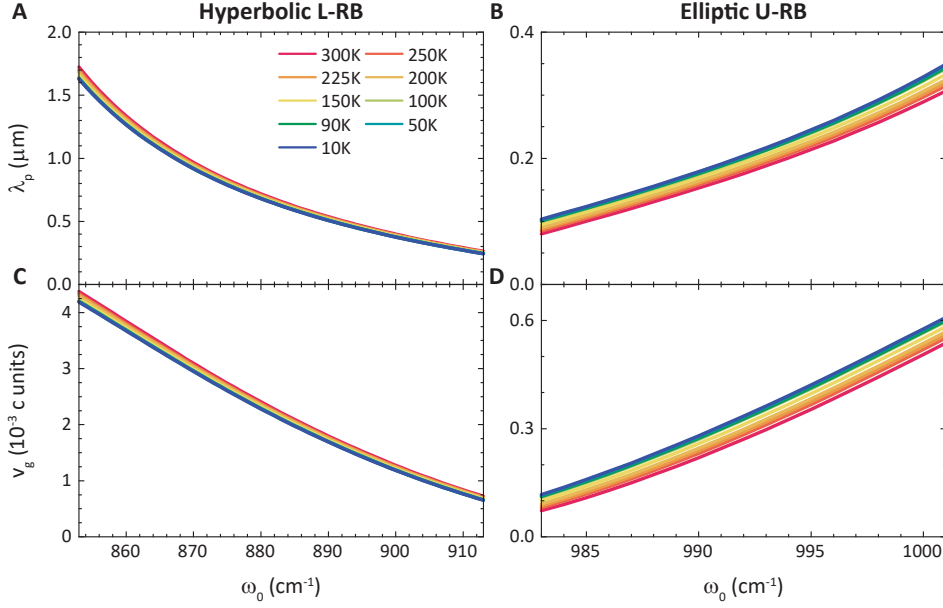
Figure 5.5: Theoretical Temperature Dependence of the Wavelength and Group Velocity of PhPs in α-MoO$_3$ **A, B** PhPs wavelength in α-MoO$_3$ as a function of the incident frequency for temperatures ranging from 10 to 300 K for the hyperbolic (**A**) and elliptic (**B**) RBs. **C, D** PhPs group velocity in α-MoO$_3$ as a function of the the incident frequency for temperatures ranging from 10 to 300 K for the hyperbolic (**C**) and elliptic (**D**) RBs. Ultra-slow group velocities are found in both regimes.

selected frequencies in each RB. The same general trend is theoretically obtained, finding enhancement values of the PhPs propagation length that even coincide with the experimental ones at $\omega_0 = 900\,cm^{-1}$ and $\omega_0 = 995\,cm^{-1}$ (at $\omega_0 = 995\,cm^{-1}$ there is a more significant difference). Taken together, these results are clear indications of an effective decrease of the PhPs damping channels by lowering the temperature of the material.

$\omega_0\,(cm^{-1})$	$\Delta L_{p,Exp}(\%)$	$\Delta L_{p,Theo}(\%)$
880	41	30
900	36	37
986	96	60
995	44	44

Table 5.1: Increase of the Propagation Lengths of PhPs in α-MoO$_3$ at Low Temperatures Increase of the propagation length as a function of temperature, defined as: $\Delta L_p(\%) = 100 \cdot [L_p(10\,K) - L_p(225\,K)]/L_p(225\,K)$, for some selected frequencies in each RB.

5.4 | Study of the Lifetimes of PhPs in α-MoO$_3$ at Low Temperatures

In this section, we carry out an analysis of the temperature-dependent PhPs lifetime using the relation $\tau = L_p/v_g$. Note that, as a difference to other polaritonic, such as
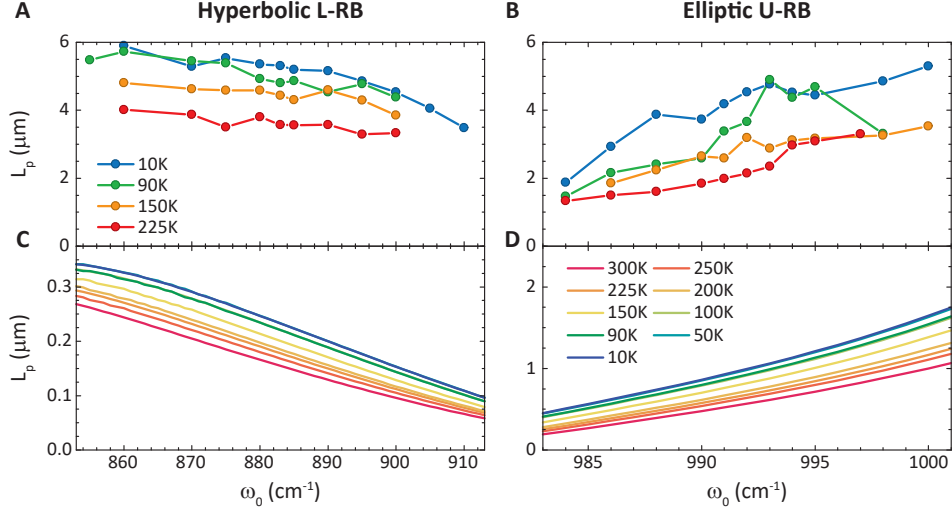
Figure 5.6: Temperature Dependence of the Propagation Length of PhPs in α-MoO$_3$ PhPs propagation length in α-MoO$_3$ as a function of incident frequency for temperatures ranging from $10\,K$ to $300\,K$ for the L-RB (**A, C**) and U-RB (**B, D**). **A** and **B** present the experimental values while **C** and **D** show the theoretically calculated results. The experimental values are obtained by fitting s-SNOM profiles (see **Figure 5.3B**) with **Eq. 5.3** while theoretical values are calculated by taking the inverse of the imaginary part of the polariton wavenumber given by **Eq. 5.4**. In all cases, the propagation length increases for lower temperatures.

the wavelength, that cannot be directly compared between experiment and theory at a fixed frequency due to the presence of frequency shifts of the DFT calculations, lifetime is a figure of merit that is almost frequency-independent (its value is almost constant within the RB excepting at its extremities, i.e., at ω_{TO} and ω_{LO}). As an example, **Figure 5.7** shows the theoretically calculated lifetime (employing the permittivity of α-MoO$_3$ extracted by *ab initio* calculations) for the fundamental PhPs mode in a $104\,nm$-thick α-MoO$_3$ flake at a temperature of $300\,K$. We can observe that the lifetime slightly increases in the spectral range from $850\,cm^{-1}$ to $920\,cm^{-1}$.
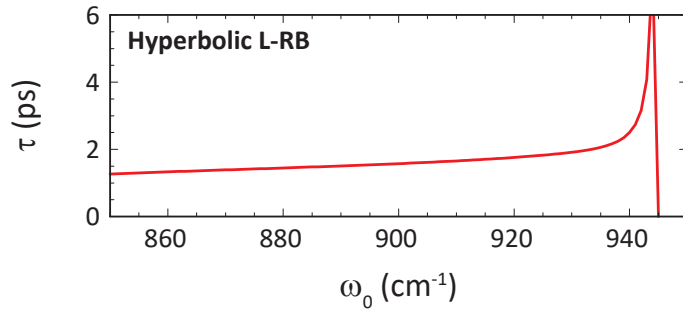
Figure 5.7: Frequency Dependence of the PhPs Lifetimes in α-MoO$_3$ PhPs lifetime in the hyperbolic L-RB calculated using the permittivity of α-MoO$_3$ extracted from ab initio calculations.

PhPs Lifetimes in α-MoO$_3$

The resulting experimental and theoretical PhPs lifetimes are shown in **Figure 5.8** for both RBs (**Figure 5.8B** and **Figure 5.8B** for the hyperbolic and elliptic RB,

respectively). A good agreement between experiment (star symbols) and theory (circles) is observed. As an example, the theoretical lifetimes at the lowest temperature $(10\,K)$ reach values of $1.86\,ps$, $2.59\,ps$, $10.8\,ps$ and $9.7\,ps$ for $\omega_0 = 860, 895, 988$ and $994\,cm^{-1}$, respectively, while the experimentally extracted values are $1.3 \pm 0.3\,ps$, $2.5 \pm 0.5\,ps$, $15 \pm 8\,ps$ and $10 \pm 3\,ps$, respectively (note that due to the inverted trend in frequency of the group velocities in the U- and L-RB, the longest lifetimes are found in the vicinity of ω_{TO} for the elliptic regime and in the vicinity of ω_{LO} for the hyperbolic regime).
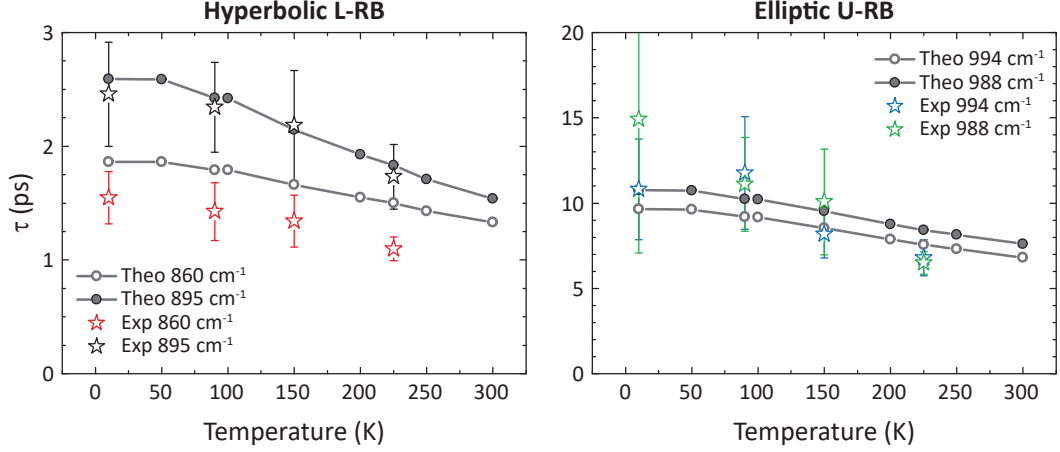
Figure 5.8: Temperature Dependence of the PhPs Lifetimes in α-MoO$_3$
Theoretical (star symbols) and experimental (circles) PhPs lifetimes for a $104\,nm$-thick α-MoO$_3$ flake as a function of temperature for (**A**) the hyperbolic RB ($\omega_0 = 860\,cm^{-1}$ and $\omega_0 = 895\,cm^{-1}$) and (**B**) the elliptic RB ($\omega_0 = 988\,cm^{-1}$ and $\omega_0 = 994\,cm^{-1}$). Grey lines are guides to the eye.

Regarding the good agreement between theory and experiment, note that as mentioned in Section 5.2, the *ab initio* calculations were performed considering only three-phonon anharmonic interactions for the phonon lifetime (two-phonon collision to form another phonon or a phonon annihilation to form two phonons), without any empirical parameter or any other type of phonon scattering mechanism (such as electron-phonon scattering or the presence of impurities), accurately reproducing the experimental changes of ω_{TO} with temperature. Thus, the only temperature-dependent parameter in our calculations is the thermal occupancy of the phonon modes, with the lower occupancy of the modes at low temperatures reducing the phonon scattering rate. This carries over to the properties of the PhPs, in particular to the PhPs lifetimes, which agree well with the experimental results, thus revealing that the damping mechanisms in the material are indeed entirely dominated by third-order anharmonic effects[*].

5.5 | Conclusions

The existence of PhPs in van der Waals polar materials are intimately related to phonon resonances whose properties in terms of linewidth and spectral position strongly depend on the temperature. In this chapter, we have studied the effect

---

[*]A detailed study of these results is currently under investigation at the time of writing this thesis.

of thermally induced phonon scattering processes on the propagation properties of PhPs in α-MoO$_3$ crystals.

In particular, by FTIR measurements and DFT calculations we reveal a good agreement on the spectral shift of ω_{TO} along the [100] and [001] crystal directions (leading to an overall broadening of the FTIR reflectance spectra) with temperature. More importantly, our DFT calculations reproduce the phonon scattering rate γ and phonon lifetime τ, showing that anharmonicity (the decay of a phonon mode into low-energy phonon modes) can well explain the increase of the phonon lifetime at low temperatures.

In addition, we extracted the PhPs propagation length, group velocity and wavelength as a function of temperature by s-SNOM nanoimaging. The obtained results show good qualitative agreement with first principles calculations, particularly for the α-MoO$_3$ PhPs lifetime, which reach record-high values of $\tau = 11 \pm 3\,ps$ at $\omega_0 = 994\,cm^{-1}$ and $T = 10\,K$. Taken together, these results reveal that anharmonic phonon scattering processes alone explain the damping mechanisms of PhPs in α-MoO$_3$.

Bibliography

[1] N. Bohr, "Lxxiii. on the constitution of atoms and molecules," *The London, Edinburgh, and Dublin Philosophical Magazine and Journal of Science*, vol. 26, no. 155, pp. 857–875, 1913.

[2] N. G. Basov, "Semiconductor lasers," *Science*, vol. 149, no. 3686, pp. 821–827, 1965.

[3] J. Faist, F. Capasso, D. L. Sivco, C. Sirtori, A. L. Hutchinson, and A. Y. Cho, "Quantum cascade laser," *Science*, vol. 264, no. 5158, pp. 553–556, 1994.

[4] A. Ashkin, J. M. Dziedzic, J. E. Bjorkholm, and S. Chu, "Observation of a single-beam gradient force optical trap for dielectric particles," *Optics Letters*, vol. 11, no. 5, pp. 288–290, 1986.

[5] M. Born and E. Wolf, *Principles of optics: electromagnetic theory of propagation, interference and diffraction of light.* Elsevier, 2013.

[6] P. Li, I. Dolado, F. J. Alfaro-Mozaz, R. Esteban, A. Atxabal, F. Casanova, L. E. Hueso, P. Alonso-González, J. Aizpurua, A. Y. Nikitin, *et al.*, "Boron nitride nanoresonators for phonon-enhanced molecular vibrational spectroscopy at the strong coupling limit," *Light: Science & Applications*, vol. 7, no. 4, pp. 17172–17172, 2018.

[7] T. Low, A. Chaves, J. D. Caldwell, A. Kumar, N. X. Fang, P. Avouris, T. F. Heinz, F. Guinea, L. Martin-Moreno, and F. Koppens, "Polaritons in layered two-dimensional materials," *Nature Materials*, vol. 16, no. 2, pp. 182–194, 2017.

[8] D. Basov, M. Fogler, and F. García de Abajo, "Polaritons in van der Waals materials," *Science*, vol. 354, no. 6309, p. aag1992, 2016.

[9] W. L. Barnes, A. Dereux, and T. W. Ebbesen, "Surface plasmon subwavelength optics," *Nature*, vol. 424, no. 6950, pp. 824–830, 2003.

[10] A. Bylinkin, M. Schnell, F. Calavalle, P. Li, J. Taboada-Gutièrrez, S. Liu, J. H. Edgar, F. Casanova, L. E. Hueso, P. Alonso-Gonzalez, *et al.*, "Real-space observation of vibrational strong coupling between propagating phonon polaritons and organic molecules," *Nature Photonics*, vol. 15, no. 3, pp. 197–202, 2021.

[11] R. F. Ribeiro, L. A. Martínez-Martínez, M. Du, J. Campos-Gonzalez-Angulo, and J. Yuen-Zhou, "Polariton chemistry: controlling molecular dynamics with optical cavities," *Chemical Science*, vol. 9, no. 30, pp. 6325–6339, 2018.

[12] W. Ahn, D. C. Ratchford, P. E. Pehrsson, and B. S. Simpkins, "Surface plasmon polariton-induced hot carrier generation for photocatalysis," *Nanoscale*, vol. 9, no. 9, pp. 3010–3022, 2017.

[13] P. Van Zwol, K. Joulain, P. Ben-Abdallah, and J. Chevrier, "Phonon polaritons enhance near-field thermal transfer across the phase transition of VO_2," *Physical Review B*, vol. 84, no. 16, p. 161413, 2011.

[14] J.-J. Greffet, R. Carminati, K. Joulain, J.-P. Mulet, S. Mainguy, and Y. Chen, "Coherent emission of light by thermal sources," *Nature*, vol. 416, no. 6876, pp. 61–64, 2002.

[15] A. Huber, B. Deutsch, L. Novotny, and R. Hillenbrand, "Focusing of surface phonon polaritons," *Applied Physics Letters*, vol. 92, no. 20, p. 203104, 2008.

[16] D. Basov, A. Asenjo-Garcia, P. J. Schuck, X. Zhu, and A. Rubio, "Polariton panorama," *Nanophotonics*, vol. 10, no. 1, pp. 549–577, 2021.

[17] R. H. Ritchie, "Plasma losses by fast electrons in thin films," *Physical Review*, vol. 106, no. 5, p. 874, 1957.

[18] S. A. Maier and H. A. Atwater, "Plasmonics: Localization and guiding of electromagnetic energy in metal/dielectric structures," *Journal of Applied Physics*, vol. 98, no. 1, p. 10, 2005.

[19] L. Novotny and B. Hecht, *Principles of nano-optics*. Cambridge University Press, 2012.

[20] S. Kawata, M. Ohtsu, and M. Irie, *Near-field optics and surface plasmon polaritons*, vol. 81. Springer Science & Business Media, 2001.

[21] H. Raether, "Surface plasmons on smooth surfaces," in *Surface plasmons on smooth and rough surfaces and on gratings*, pp. 4–39, Springer, 1988.

[22] M. Fleischmann, P. J. Hendra, and A. J. McQuillan, "Raman spectra of pyridine adsorbed at a silver electrode," *Chemical Physics Letters*, vol. 26, no. 2, pp. 163–166, 1974.

[23] J. Tsang, J. Kirtley, and J. Bradley, "Surface-enhanced Raman spectroscopy and surface plasmons," *Physical Review Letters*, vol. 43, no. 11, p. 772, 1979.

[24] M. Fox, "Optical properties of solids," 2002.

[25] V. M. Agranovich, *Surface polaritons*. Elsevier, 2012.

[26] A. D. Boardman, *Electromagnetic surface modes*. John Wiley & Sons, 1982.

[27] T. J. Derrien, J. Krüger, and J. Bonse, "Properties of surface plasmon polaritons on lossy materials: Lifetimes, periods and excitation conditions," *Journal of Optics*, vol. 18, no. 11, p. 115007, 2016.

[28] J. B. Khurgin, "Relative merits of phononics vs. plasmonics: the energy balance approach," *Nanophotonics*, vol. 7, no. 1, pp. 305–316, 2018.

[29]   R. Hillenbrand, T. Taubner, and F. Keilmann, "Phonon-enhanced light–matter interaction at the nanometer scale," *Nature*, vol. 418, no. 6894, pp. 159–162, 2002.

[30]   K. S. Novoselov, A. K. Geim, S. V. Morozov, D.-e. Jiang, Y. Zhang, S. V. Dubonos, I. V. Grigorieva, and A. A. Firsov, "Electric field effect in atomically thin carbon films," *Science*, vol. 306, no. 5696, pp. 666–669, 2004.

[31]   K. S. Novoselov, A. K. Geim, S. V. Morozov, D. Jiang, M. I. Katsnelson, I. Grigorieva, S. Dubonos, and a. Firsov, "Two-dimensional gas of massless dirac fermions in graphene," *Nature*, vol. 438, no. 7065, pp. 197–200, 2005.

[32]   A. C. Neto, F. Guinea, N. M. Peres, K. S. Novoselov, and A. K. Geim, "The electronic properties of graphene," *Reviews of Modern Physics*, vol. 81, no. 1, p. 109, 2009.

[33]   A. K. Geim, "Graphene: status and prospects," *Science*, vol. 324, no. 5934, pp. 1530–1534, 2009.

[34]   P. Blake, P. D. Brimicombe, R. R. Nair, T. J. Booth, D. Jiang, F. Schedin, L. A. Ponomarenko, S. V. Morozov, H. F. Gleeson, E. W. Hill, *et al.*, "Graphene-based liquid crystal device," *Nano Letters*, vol. 8, no. 6, pp. 1704–1708, 2008.

[35]   R. Nair, H. Wu, P. Jayaram, I. Grigorieva, and A. Geim, "Unimpeded permeation of water through helium-leak–tight graphene-based membranes," *Science*, vol. 335, no. 6067, pp. 442–444, 2012.

[36]   K. F. Mak, C. Lee, J. Hone, J. Shan, and T. F. Heinz, "Atomically thin mos$_2$: a new direct-gap semiconductor," *Physical Review Letters*, vol. 105, no. 13, p. 136805, 2010.

[37]   C. R. Dean, A. F. Young, I. Meric, C. Lee, L. Wang, S. Sorgenfrei, K. Watanabe, T. Taniguchi, P. Kim, K. L. Shepard, *et al.*, "Boron nitride substrates for high-quality graphene electronics," *Nature Nanotechnology*, vol. 5, no. 10, pp. 722–726, 2010.

[38]   J. Chen, M. Badioli, P. Alonso-González, S. Thongrattanasiri, F. Huth, J. Osmond, M. Spasenović, A. Centeno, A. Pesquera, P. Godignon, *et al.*, "Optical nano-imaging of gate-tunable graphene plasmons," *Nature*, vol. 487, no. 7405, pp. 77–81, 2012.

[39]   Z. Fei, A. Rodin, G. O. Andreev, W. Bao, A. McLeod, M. Wagner, L. Zhang, Z. Zhao, M. Thiemens, G. Dominguez, *et al.*, "Gate-tuning of graphene plasmons revealed by infrared nano-imaging," *Nature*, vol. 487, no. 7405, pp. 82–85, 2012.

[40]   S. Dai, Z. Fei, Q. Ma, A. Rodin, M. Wagner, A. McLeod, M. Liu, W. Gannett, W. Regan, K. Watanabe, *et al.*, "Tunable phonon polaritons in atomically thin van der Waals crystals of boron nitride," *Science*, vol. 343, no. 6175, pp. 1125–1129, 2014.

[41]   W. Ma, P. Alonso-González, S. Li, A. Y. Nikitin, J. Yuan, J. Martín-Sánchez, J. Taboada-Gutiérrez, I. Amenabar, P. Li, S. Vélez, *et al.*, "In-plane anisotropic and ultra-low-loss polaritons in a natural van der Waals crystal," *Nature*, vol. 562, no. 7728, pp. 557–562, 2018.

[42] J. Taboada-Gutiérrez, G. Álvarez-Pérez, J. Duan, W. Ma, K. Crowley, I. Prieto, A. Bylinkin, H. Volkova, K. Kimura, T. Kimura, *et al.*, "Broad spectral tuning of ultra-low-loss polaritons in a van der Waals crystal by intercalation," *Nature Materials*, vol. 19, no. 9, pp. 964–968, 2020.

[43] F. Hu, Y. Luan, M. Scott, J. Yan, D. Mandrus, X. Xu, and Z. Fei, "Imaging exciton–polariton transport in $MoSe_2$ waveguides," *Nature Photonics*, vol. 11, no. 6, pp. 356–360, 2017.

[44] A. Sternbach, S. Chae, S. Latini, A. Rikhter, Y. Shao, B. Li, D. Rhodes, B. Kim, P. J. Schuck, X. Xu, *et al.*, "Programmable hyperbolic polaritons in van der Waals semiconductors," *Science*, vol. 371, no. 6529, pp. 617–620, 2021.

[45] I.-H. Lee, M. He, X. Zhang, Y. Luo, S. Liu, J. H. Edgar, K. Wang, P. Avouris, T. Low, J. D. Caldwell, *et al.*, "Image polaritons in boron nitride for extreme polariton confinement with low losses," *Nature Communications*, vol. 11, no. 1, pp. 1–8, 2020.

[46] T. V. de Oliveira, T. Nörenberg, G. Álvarez-Pérez, L. Wehmeier, J. Taboada-Gutiérrez, M. Obst, F. Hempel, E. J. Lee, J. M. Klopf, I. Errea, *et al.*, "Nanoscale-confined terahertz polaritons in a van der Waals crystal," *Advanced Materials*, vol. 33, no. 2, p. 2005777, 2021.

[47] P. Li, I. Dolado, F. J. Alfaro-Mozaz, F. Casanova, L. E. Hueso, S. Liu, J. H. Edgar, A. Y. Nikitin, S. Vélez, and R. Hillenbrand, "Infrared hyperbolic metasurface based on nanostructured van der Waals materials," *Science*, vol. 359, no. 6378, pp. 892–896, 2018.

[48] A. K. Geim and I. V. Grigorieva, "Van der Waals heterostructures," *Nature*, vol. 499, no. 7459, pp. 419–425, 2013.

[49] A. Castellanos-Gomez, M. Buscema, R. Molenaar, V. Singh, L. Janssen, H. S. Van Der Zant, and G. A. Steele, "Deterministic transfer of two-dimensional materials by all-dry viscoelastic stamping," *2D Materials*, vol. 1, no. 1, p. 011002, 2014.

[50] R. Frisenda, E. Navarro-Moratalla, P. Gant, D. P. De Lara, P. Jarillo-Herrero, R. V. Gorbachev, and A. Castellanos-Gomez, "Recent progress in the assembly of nanodevices and van der Waals heterostructures by deterministic placement of 2D materials," *Chemical Society Reviews*, vol. 47, no. 1, pp. 53–68, 2018.

[51] S. Dai, Q. Ma, M. Liu, T. Andersen, Z. Fei, M. Goldflam, M. Wagner, K. Watanabe, T. Taniguchi, M. Thiemens, *et al.*, "Graphene on hexagonal boron nitride as a tunable hyperbolic metamaterial," *Nature Nanotechnology*, vol. 10, no. 8, pp. 682–686, 2015.

[52] A. Woessner, M. B. Lundeberg, Y. Gao, A. Principi, P. Alonso-González, M. Carrega, K. Watanabe, T. Taniguchi, G. Vignale, M. Polini, *et al.*, "Highly confined low-loss plasmons in graphene–boron nitride heterostructures," *Nature Materials*, vol. 14, no. 4, pp. 421–425, 2015.

[53] G. Ni, H. Wang, J. Wu, Z. Fei, M. Goldflam, F. Keilmann, B. Özyilmaz, A. Castro Neto, X. Xie, M. Fogler, *et al.*, "Plasmons in graphene Moiré superlattices," *Nature Materials*, vol. 14, no. 12, pp. 1217–1222, 2015.

[54] S. Sunku, G. Ni, B.-Y. Jiang, H. Yoo, A. Sternbach, A. McLeod, T. Stauber, L. Xiong, T. Taniguchi, K. Watanabe, *et al.*, "Photonic crystals for nano-light in Moiré graphene superlattices," *Science*, vol. 362, no. 6419, pp. 1153–1156, 2018.

[55] H. Herzig Sheinfux and F. H. Koppens, "The rise of twist-optics," *Nano Letters*, vol. 20, no. 10, pp. 6935–6936, 2020.

[56] J. Duan, N. Capote-Robayna, J. Taboada-Gutiérrez, G. Álvarez-Pérez, I. Prieto, J. Martín-Sánchez, A. Y. Nikitin, and P. Alonso-González, "Twisted nano-optics: manipulating light at the nanoscale with twisted phonon polaritonic slabs," *Nano Letters*, vol. 20, no. 7, pp. 5323–5329, 2020.

[57] G. Hu, Q. Ou, G. Si, Y. Wu, J. Wu, Z. Dai, A. Krasnok, Y. Mazor, Q. Zhang, Q. Bao, *et al.*, "Topological polaritons and photonic magic angles in twisted α-MoO$_3$ bilayers," *Nature*, vol. 582, no. 7811, pp. 209–213, 2020.

[58] Z. Zheng, F. Sun, W. Huang, J. Jiang, R. Zhan, Y. Ke, H. Chen, and S. Deng, "Phonon polaritons in twisted double-layers of hyperbolic van der Waals crystals," *Nano Letters*, vol. 20, no. 7, pp. 5301–5308, 2020.

[59] M. Chen, X. Lin, T. H. Dinh, Z. Zheng, J. Shen, Q. Ma, H. Chen, P. Jarillo-Herrero, and S. Dai, "Configurable phonon polaritons in twisted α-MoO$_3$," *Nature Materials*, vol. 19, no. 12, pp. 1307–1311, 2020.

[60] P. A. D. Gonçalves and N. M. Peres, *An introduction to graphene plasmonics*. World Scientific, 2016.

[61] A. Y. Nikitin, F. Guinea, F. García-Vidal, and L. Martín-Moreno, "Edge and waveguide terahertz surface plasmon modes in graphene microribbons," *Physical Review B*, vol. 84, no. 16, p. 161407, 2011.

[62] M. Jablan, H. Buljan, and M. Soljačić, "Plasmonics in graphene at infrared frequencies," *Physical Review B*, vol. 80, no. 24, p. 245435, 2009.

[63] F. H. Koppens, D. E. Chang, and F. J. Garcia de Abajo, "Graphene plasmonics: a platform for strong light–matter interactions," *Nano Letters*, vol. 11, no. 8, pp. 3370–3377, 2011.

[64] G. Ni, d. A. McLeod, Z. Sun, L. Wang, L. Xiong, K. Post, S. Sunku, B.-Y. Jiang, J. Hone, C. R. Dean, *et al.*, "Fundamental limits to graphene plasmonics," *Nature*, vol. 557, no. 7706, pp. 530–533, 2018.

[65] J. Aizpurua, *World Scientific Handbook of Metamaterials and Plasmonics*. World Scientific, 2017.

[66] P. Alonso-González, A. Y. Nikitin, F. Golmar, A. Centeno, A. Pesquera, S. Vélez, J. Chen, G. Navickaite, F. Koppens, A. Zurutuza, *et al.*, "Controlling graphene plasmons with resonant metal antennas and spatial conductivity patterns," *Science*, vol. 344, no. 6190, pp. 1369–1373, 2014.

[67] L. Wang, I. Meric, P. Huang, Q. Gao, Y. Gao, H. Tran, T. Taniguchi, K. Watanabe, L. Campos, D. Muller, *et al.*, "One-dimensional electrical contact to a two-dimensional material," *Science*, vol. 342, no. 6158, pp. 614–617, 2013.

[68] J. D. Caldwell, A. V. Kretinin, Y. Chen, V. Giannini, M. M. Fogler, Y. Francescato, C. T. Ellis, J. G. Tischler, C. R. Woods, A. J. Giles, *et al.*, "Sub-diffractional volume-confined polaritons in the natural hyperbolic material hexagonal boron nitride," *Nature Communications*, vol. 5, no. 1, pp. 1–9, 2014.

[69] G. Bhimanapati, N. Glavin, and J. A. Robinson, "2D boron nitride: synthesis and applications," in *Semiconductors and Semimetals*, vol. 95, pp. 101–147, Elsevier, 2016.

[70] E. Yoxall, M. Schnell, A. Y. Nikitin, O. Txoperena, A. Woessner, M. B. Lundeberg, F. Casanova, L. E. Hueso, F. H. Koppens, and R. Hillenbrand, "Direct observation of ultraslow hyperbolic polariton propagation with negative phase velocity," *Nature Photonics*, vol. 9, no. 10, pp. 674–678, 2015.

[71] A. J. Giles, S. Dai, I. Vurgaftman, T. Hoffman, S. Liu, L. Lindsay, C. T. Ellis, N. Assefa, I. Chatzakis, T. L. Reinecke, *et al.*, "Ultralow-loss polaritons in isotopically pure boron nitride," *Nature Materials*, vol. 17, no. 2, pp. 134–139, 2018.

[72] S. Dai, W. Fang, N. Rivera, Y. Stehle, B.-Y. Jiang, J. Shen, R. Y. Tay, C. J. Ciccarino, Q. Ma, D. Rodan-Legrain, *et al.*, "Phonon polaritons in monolayers of hexagonal boron nitride," *Advanced Materials*, vol. 31, no. 37, p. 1806603, 2019.

[73] A. Kumar, T. Low, K. H. Fung, P. Avouris, and N. X. Fang, "Tunable light–matter interaction and the role of hyperbolicity in graphene-h-BN system," *Nano Letters*, vol. 15, no. 5, pp. 3172–3180, 2015.

[74] M. Autore, I. Dolado, P. Li, R. Esteban, F. J. Alfaro-Mozaz, A. Atxabal, S. Liu, J. H. Edgar, S. Vélez, F. Casanova, *et al.*, "Enhanced light–matter interaction in 10b monoisotopic boron nitride infrared nanoresonators," *Advanced Optical Materials*, vol. 9, no. 5, p. 2001958, 2021.

[75] F. J. Alfaro-Mozaz, S. G. Rodrigo, P. Alonso-González, S. Vélez, I. Dolado, F. Casanova, L. E. Hueso, L. Martín-Moreno, R. Hillenbrand, and A. Y. Nikitin, "Deeply subwavelength phonon-polaritonic crystal made of a van der Waals material," *Nature Communications*, vol. 10, no. 1, pp. 1–7, 2019.

[76] P. Li, X. Yang, T. W. Maß, J. Hanss, M. Lewin, A.-K. U. Michel, M. Wuttig, and T. Taubner, "Reversible optical switching of highly confined phonon–polaritons with an ultrathin phase-change material," *Nature Materials*, vol. 15, no. 8, pp. 870–875, 2016.

[77] K. Chaudhary, M. Tamagnone, X. Yin, C. M. Spägele, S. L. Oscurato, J. Li, C. Persch, R. Li, N. A. Rubin, L. A. Jauregui, *et al.*, "Polariton nanophotonics using phase-change materials," *Nature Communications*, vol. 10, no. 1, pp. 1–6, 2019.

[78] L. Ferrari, C. Wu, D. Lepage, X. Zhang, and Z. Liu, "Hyperbolic metamaterials and their applications," *Progress in Quantum Electronics*, vol. 40, pp. 1–40, 2015.

[79] D. Smith and D. Schurig, "Electromagnetic wave propagation in media with indefinite permittivity and permeability tensors," *Physical Review Letters*, vol. 90, no. 7, p. 077405, 2003.

[80] G. Hu, J. Shen, C.-W. Qiu, A. Alù, and S. Dai, "Phonon polaritons and hyperbolic response in van der Waals materials," *Advanced Optical Materials*, vol. 8, no. 5, p. 1901393, 2020.

[81] A. Poddubny, I. Iorsh, P. Belov, and Y. Kivshar, "Hyperbolic metamaterials," *Nature Photonics*, vol. 7, no. 12, pp. 948–957, 2013.

[82] A. A. High, R. C. Devlin, A. Dibos, M. Polking, D. S. Wild, J. Perczel, N. P. De Leon, M. D. Lukin, and H. Park, "Visible-frequency hyperbolic metasurface," *Nature*, vol. 522, no. 7555, pp. 192–196, 2015.

[83] A. S. Potemkin, A. N. Poddubny, P. A. Belov, and Y. S. Kivshar, "Green function for hyperbolic media," *Physical Review A*, vol. 86, no. 2, p. 023848, 2012.

[84] S. Dai, Q. Ma, T. Andersen, A. Mcleod, Z. Fei, M. Liu, M. Wagner, K. Watanabe, T. Taniguchi, M. Thiemens, *et al.*, "Subdiffractional focusing and guiding of polaritonic rays in a natural hyperbolic material," *Nature Communications*, vol. 6, no. 1, pp. 1–7, 2015.

[85] P. Li, M. Lewin, A. V. Kretinin, J. D. Caldwell, K. S. Novoselov, T. Taniguchi, K. Watanabe, F. Gaussmann, and T. Taubner, "Hyperbolic phonon-polaritons in boron nitride for near-field optical imaging and focusing," *Nature Communications*, vol. 6, no. 1, pp. 1–9, 2015.

[86] A. Y. Nikitin, E. Yoxall, M. Schnell, S. Velez, I. Dolado, P. Alonso-Gonzalez, F. Casanova, L. E. Hueso, and R. Hillenbrand, "Nanofocusing of hyperbolic phonon polaritons in a tapered boron nitride slab," *ACS Photonics*, vol. 3, no. 6, pp. 924–929, 2016.

[87] A. V. Kildishev, A. Boltasseva, and V. M. Shalaev, "Planar photonics with metasurfaces," *Science*, vol. 339, no. 6125, p. 1232009, 2013.

[88] R. Hillenbrand and F. Keilmann, "Complex optical constants on a subwavelength scale," *Physical Review Letters*, vol. 85, no. 14, p. 3029, 2000.

[89] F. Zenhausern, Y. Martin, and H. Wickramasinghe, "Scanning interferometric apertureless microscopy: optical imaging at 10 angstrom resolution," *Science*, vol. 269, no. 5227, pp. 1083–1085, 1995.

[90] R. Hillenbrand, "Towards phonon photonics: scattering-type near-field optical microscopy reveals phonon-enhanced near-field interaction," *Ultramicroscopy*, vol. 100, no. 3-4, pp. 421–427, 2004.

[91] N. Ocelic, A. Huber, and R. Hillenbrand, "Pseudoheterodyne detection for background-free near-field spectroscopy," *Applied Physics Letters*, vol. 89, no. 10, p. 101124, 2006.

[92] X. Chen, D. Hu, R. Mescall, G. You, D. Basov, Q. Dai, and M. Liu, "Modern scattering-type scanning near-field optical microscopy for advanced material research," *Advanced Materials*, vol. 31, no. 24, p. 1804774, 2019.

[93] N. Ocelic, *Quantitative near-field phonon-polariton spectroscopy.* PhD thesis, Technische Universität München, 2007.

[94] M. D. Sonntag, E. A. Pozzi, N. Jiang, M. C. Hersam, and R. P. Van Duyne, "Recent advances in tip-enhanced Raman spectroscopy," *The Journal of Physical Chemistry Letters*, vol. 5, no. 18, pp. 3125–3130, 2014.

[95] M. S. Anderson, "Locally enhanced Raman spectroscopy with an atomic force microscope," *Applied Physics Letters*, vol. 76, no. 21, pp. 3130–3132, 2000.

[96] A. Huber, A. Ziegler, T. Köck, and R. Hillenbrand, "Infrared nanoscopy of strained semiconductors," *Nature Nanotechnology*, vol. 4, no. 3, pp. 153–157, 2009.

[97] F. Huth, M. Schnell, J. Wittborn, N. Ocelic, and R. Hillenbrand, "Infrared-spectroscopic nanoimaging with a thermal source," *Nature Materials*, vol. 10, no. 5, pp. 352–356, 2011.

[98] J. M. Gerton, L. A. Wade, G. A. Lessard, Z. Ma, and S. R. Quake, "Tip-enhanced fluorescence microscopy at 10 nanometer resolution," *Physical Review Letters*, vol. 93, no. 18, p. 180801, 2004.

[99] F. L. Ruta, A. J. Sternbach, A. B. Dieng, A. S. McLeod, and D. Basov, "Quantitative nanoinfrared spectroscopy of anisotropic van der Waals materials," *Nano Letters*, vol. 20, no. 11, pp. 7933–7940, 2020.

[100] A. V. Zayats and D. Richards, *Nano-optics and near-field optical microscopy.* Artech House, 2009.

[101] B. Knoll and F. Keilmann, "Near-field probing of vibrational absorption for chemical microscopy," *Nature*, vol. 399, no. 6732, pp. 134–137, 1999.

[102] A. Cvitkovic, N. Ocelic, and R. Hillenbrand, "Analytical model for quantitative prediction of material contrasts in scattering-type near-field optical microscopy," *Optics Express*, vol. 15, no. 14, pp. 8550–8565, 2007.

[103] S. Dai, Q. Ma, Y. Yang, J. Rosenfeld, M. D. Goldflam, A. McLeod, Z. Sun, T. I. Andersen, Z. Fei, M. Liu, *et al.*, "Efficiency of launching highly confined polaritons by infrared light incident on a hyperbolic material," *Nano Letters*, vol. 17, no. 9, pp. 5285–5290, 2017.

[104] J. Martín-Sánchez, J. Duan, J. Taboada-Gutiérrez, G. Álvarez-Pérez, K. V. Voronin, I. Prieto, W. Ma, Q. Bao, V. S. Volkov, R. Hillenbrand, *et al.*, "Focusing of in-plane hyperbolic polaritons in van der Waals crystals with tailored infrared nanoantennas," *Science Advances*, vol. 7, no. 41, p. eabj0127, 2021.

[105] J. Duan, G. Álvarez-Pérez, A. I. Tresguerres-Mata, J. Taboada-Gutiérrez, K. V. Voronin, A. Bylinkin, B. Chang, S. Xiao, S. Liu, J. H. Edgar, *et al.*, "Planar refraction and lensing of highly confined polaritons in anisotropic media," *Nature Communications*, vol. 12, no. 1, pp. 1–8, 2021.

[106] A. Heßler, S. Wahl, T. Leuteritz, A. Antonopoulos, C. Stergianou, C.-F. Schön, L. Naumann, N. Eicker, M. Lewin, T. W. Maß, *et al.*, "In$_3$SbTe$_2$ as a programmable nanophotonics material platform for the infrared," *Nature Communications*, vol. 12, no. 1, pp. 1–10, 2021.

[107] M. Wuttig, H. Bhaskaran, and T. Taubner, "Phase-change materials for nonvolatile photonic applications," *Nature Photonics*, vol. 11, no. 8, pp. 465–476, 2017.

[108] T. Taubner, D. Korobkin, Y. Urzhumov, G. Shvets, and R. Hillenbrand, "Near-field microscopy through a SiC superlens," *Science*, vol. 313, no. 5793, pp. 1595–1595, 2006.

[109] P. Alonso-González, A. Y. Nikitin, Y. Gao, A. Woessner, M. B. Lundeberg, A. Principi, N. Forcellini, W. Yan, S. Vélez, A. J. Huber, *et al.*, "Acoustic terahertz graphene plasmons revealed by photocurrent nanoscopy," *Nature Nanotechnology*, vol. 12, no. 1, pp. 31–35, 2017.

[110] T. Cocker, V. Jelic, R. Hillenbrand, and F. Hegmann, "Nanoscale terahertz scanning probe microscopy," *Nature Photonics*, vol. 15, no. 8, pp. 558–569, 2021.

[111] K. Novoselov, o. A. Mishchenko, o. A. Carvalho, and A. Castro Neto, "2D materials and van der Waals heterostructures," *Science*, vol. 353, no. 6298, p. aac9439, 2016.

[112] S. Das, J. A. Robinson, M. Dubey, H. Terrones, and M. Terrones, "Beyond graphene: progress in novel two-dimensional materials and van der Waals solids," *Annual Review of Materials Research*, vol. 45, pp. 1–27, 2015.

[113] R. V. Gorbachev, I. Riaz, R. R. Nair, R. Jalil, L. Britnell, B. D. Belle, E. W. Hill, K. S. Novoselov, K. Watanabe, T. Taniguchi, *et al.*, "Hunting for monolayer boron nitride: optical and Raman signatures," *Small*, vol. 7, no. 4, pp. 465–468, 2011.

[114] M. Yi and Z. Shen, "A review on mechanical exfoliation for the scalable production of graphene," *Materials Chemistry A*, vol. 3, pp. 11700–11715, 2015.

[115] M. Benameur, B. Radisavljevic, J. Héron, S. Sahoo, H. Berger, and A. Kis, "Visibility of dichalcogenide nanolayers," *Nanotechnology*, vol. 22, no. 12, p. 125706, 2011.

[116] S. Puebla, A. Mariscal-Jiménez, R. S. Galán, C. Munuera, and A. Castellanos-Gomez, "Optical-based thickness measurement of MoO_3 nanosheets," *Nanomaterials*, vol. 10, no. 7, p. 1272, 2020.

[117] D. Golla, K. Chattrakun, K. Watanabe, T. Taniguchi, B. J. LeRoy, and A. Sandhu, "Optical thickness determination of hexagonal boron nitride flakes," *Applied Physics Letters*, vol. 102, no. 16, p. 161906, 2013.

[118] W. Chew, *Waves and fields in inhomogeneous media.* Springer, 1990.

[119] G. R. Fowles, *Introduction to modern optics.* Courier Corporation, 1989.

[120] P. R. Griffiths and J. A. De Haseth, *Fourier transform infrared spectrometry.* John Wiley & Sons, 2007.

[121] T. Taubner, R. Hillenbrand, and F. Keilmann, "Performance of visible and mid-infrared scattering-type near-field optical microscopes," *Journal of Microscopy*, vol. 210, no. 3, pp. 311–314, 2003.

[122] F. Keilmann and R. Hillenbrand, "Near-field microscopy by elastic light scattering from a tip," *Philosophical Transactions of the Royal Society of London. Series A: Mathematical, Physical and Engineering Sciences*, vol. 362, no. 1817, pp. 787–805, 2004.

[123] F. Huth, *Nano-FTIR-Nanoscale Infrared Near-Field Spectroscopy*. PhD thesis, UPV/EHU, 2015.

[124] I. Amenabar Altuna, *Infrared nanospectroscopy and hyperspectral nanoimaging of organic matter*. PhD thesis, UPV/EHU, 2017.

[125] https://www.comsol.com.

[126] I. A. De Castro, R. S. Datta, J. Z. Ou, A. Castellanos-Gomez, S. Sriram, T. Daeneke, and K. Kalantar-zadeh, "Molybdenum oxides–from fundamentals to functionality," *Advanced Materials*, vol. 29, no. 40, p. 1701619, 2017.

[127] S. Balendhran, S. Walia, H. Nili, J. Z. Ou, S. Zhuiykov, R. B. Kaner, S. Sriram, M. Bhaskaran, and K. Kalantar-zadeh, "Two-dimensional molybdenum trioxide and dichalcogenides," *Advanced Functional Materials*, vol. 23, no. 32, pp. 3952–3970, 2013.

[128] T. Anh Tran, K. Krishnamoorthy, Y. W. Song, S. K. Cho, and S. J. Kim, "Toxicity of nano molybdenum trioxide toward invasive breast cancer cells," *ACS Applied Materials & Interfaces*, vol. 6, no. 4, pp. 2980–2986, 2014.

[129] J. Wang, Q. Zhou, S. Peng, L. Xu, and W. Zeng, "Volatile organic compounds gas sensors based on molybdenum oxides: a mini review," *Frontiers in chemistry*, vol. 8, p. 339, 2020.

[130] L. Seguin, M. Figlarz, R. Cavagnat, and J.-C. Lassègues, "Infrared and Raman spectra of MoO_3 molybdenum trioxides and $MoO_3 \cdot xH_2O$ molybdenum trioxide hydrates," *Spectrochimica Acta Part A: Molecular and Biomolecular Spectroscopy*, vol. 51, no. 8, pp. 1323–1344, 1995.

[131] H. Ding, K. G. Ray, V. Ozolins, and M. Asta, "Structural and vibrational properties of α-MoO_3 from van der Waals corrected density functional theory calculations," *Phys. Rev. B*, vol. 85, p. 012104, Jan 2012.

[132] G. Álvarez-Pérez, T. G. Folland, I. Errea, J. Taboada-Gutiérrez, J. Duan, J. Martín-Sánchez, A. I. Tresguerres-Mata, J. R. Matson, A. Bylinkin, M. He, *et al.*, "Infrared permittivity of the biaxial van der Waals semiconductor α-MoO_3 from near-and far-field correlative studies," *Advanced Materials*, vol. 32, no. 29, p. 1908176, 2020.

[133] P. Bharadwaj, B. Deutsch, and L. Novotny, "Optical antennas," *Advances in Optics and Photonics*, vol. 1, no. 3, pp. 438–483, 2009.

[134] L. Novotny and N. Van Hulst, "Antennas for light," *Nature Photonics*, vol. 5, no. 2, pp. 83–90, 2011.

[135] R. L. Olmon, P. M. Krenz, A. C. Jones, G. D. Boreman, and M. B. Raschke, "Near-field imaging of optical antenna modes in the mid-infrared," *Optics Express*, vol. 16, no. 25, pp. 20295–20305, 2008.

[136] D. Weber, P. Albella, P. Alonso-González, F. Neubrech, H. Gui, T. Nagao, R. Hillenbrand, J. Aizpurua, and A. Pucci, "Longitudinal and transverse coupling in infrared gold nanoantenna arrays: long range versus short range interaction regimes," *Optics Express*, vol. 19, no. 16, pp. 15047–15061, 2011.

[137] F. J. Alfaro Mozaz, *Mid-infrared nanophotonics with hyperbolic phonon polaritons.* PhD thesis, UPV/EHU, 2020.

[138] P. Christopher, H. Xin, and S. Linic, "Visible-light-enhanced catalytic oxidation reactions on plasmonic silver nanostructures," *Nature Chemistry*, vol. 3, no. 6, pp. 467–472, 2011.

[139] D. Rodrigo, O. Limaj, D. Janner, D. Etezadi, F. J. García de Abajo, V. Pruneri, and H. Altug, "Mid-infrared plasmonic biosensing with graphene," *Science*, vol. 349, no. 6244, pp. 165–168, 2015.

[140] S. Kim, S. G. Menabde, V. W. Brar, and M. S. Jang, "Functional mid-infrared polaritonics in van der Waals crystals," *Advanced Optical Materials*, vol. 8, no. 5, p. 1901194, 2020.

[141] P. Li, I. Dolado, F. Alfaro-Mozaz, A. Y. Nikitin, F. Casanova, L. Hueso, S. Vélez, and R. Hillenbrand, "Optical nanoimaging of hyperbolic surface polaritons at the edges of van der Waals materials," *Nano Letters*, vol. 17, no. 1, pp. 228–235, 2017.

[142] G. Álvarez-Pérez, K. V. Voronin, V. S. Volkov, P. Alonso-González, and A. Y. Nikitin, "Analytical approximations for the dispersion of electromagnetic modes in slabs of biaxial crystals," *Physical Review B*, vol. 100, no. 23, p. 235408, 2019.

[143] R. Saravanan, V. Gupta, E. Mosquera, and F. Gracia, "Preparation and characterization of V_2O_5/ZnO nanocomposite system for photocatalytic application," *Journal of Molecular Liquids*, vol. 198, pp. 409–412, 2014.

[144] L. R. De Jesus, G. A. Horrocks, Y. Liang, A. Parija, C. Jaye, L. Wangoh, J. Wang, D. A. Fischer, L. F. Piper, D. Prendergast, *et al.*, "Mapping polaronic states and lithiation gradients in individual V_2O_5 nanowires," *Nature Communications*, vol. 7, no. 1, pp. 1–9, 2016.

[145] Y. Yuan and L. Hong, "Micro and nano structured vanadium pentoxide (V_2O_5) for electrodes of lithium ion batteries," *Advanced Energy Materials*, vol. 7, p. 1602545, 2017.

[146] K. Schneider, M. Lubecka, and A. Czapla, "V_2O_5 thin films for gas sensor applications," *Sensors and Actuators B: Chemical*, vol. 236, pp. 970–977, 2016.

[147] D. O. Scanlon, A. Walsh, B. J. Morgan, and G. W. Watson, "An ab initio study of reduction of V_2O_5 through the formation of oxygen vacancies and Li intercalation," *The Journal of Physical Chemistry C*, vol. 112, no. 26, pp. 9903–9911, 2008.

[148] C. Bhandari, W. R. Lambrecht, and M. Van Schilfgaarde, "Quasiparticle self-consistent GW calculations of the electronic band structure of bulk and monolayer V_2O_5," *Physical Review B*, vol. 91, no. 12, p. 125116, 2015.

[149] C. Bhandari and W. R. Lambrecht, "Phonons and related spectra in bulk and monolayer V_2O_5," *Physical Review B*, vol. 89, no. 4, p. 045109, 2014.

[150] P. Clauws and J. Vennik, "Lattice vibrations of V_2O_5. determination of TO and LO frequencies from infrared reflection and transmission," *Physica Status Solidi (b)*, vol. 76, no. 2, pp. 707–713, 1976.

[151] S. Sucharitakul, G. Ye, W. R. Lambrecht, C. Bhandari, A. Gross, R. He, H. Poelman, and X. P. Gao, "V_2O_5: A 2D van der Waals oxide with strong in-plane electrical and optical anisotropy," *ACS applied materials & interfaces*, vol. 9, no. 28, pp. 23949–23956, 2017.

[152] M. S. Vitiello, G. Scalari, B. Williams, and P. De Natale, "Quantum cascade lasers: 20 years of challenges," *Optics Express*, vol. 23, no. 4, pp. 5167–5182, 2015.

[153] C. Bhandari and W. R. Lambrecht, "Electronic and magnetic properties of electron-doped V_2O_5 and NaV_2O_5," *Physical Review B*, vol. 92, no. 12, p. 125133, 2015.

[154] M. Isobe and Y. Ueda, "Magnetic susceptibility of quasi-one-dimensional compound α'-NaV_2O_5 -possible spin-peierls compound with high critical temperature of 34 K-," *Journal of the Physical Society of Japan*, vol. 65, no. 5, pp. 1178–1181, 1996.

[155] H. Iwase, M. Isobe, Y. Ueda, and H. Yasuoka, "Observation of spin gap in CaV_2O_5 by nmr," *Journal of the Physical Society of Japan*, vol. 65, no. 8, pp. 2397–2400, 1996.

[156] Y. Ueda and M. Isobe, "Magnetic properties of AV_2O_5 (A= Li, Na, Cs, Ca and Mg)," *Journal of Magnetism and Magnetic Materials*, vol. 177, pp. 741–742, 1998.

[157] T. Ohama, M. Isobe, and Y. Ueda, "Spin excitations in the two-leg ladder antiferromagnet CaV_2O_5," *Journal of the Physical Society of Japan*, vol. 70, no. 6, pp. 1801–1807, 2001.

[158] Y. Kanke, K. Kato, E. Takayama-Muromachi, M. Isobe, and K. Kosuda, "Structure of $K_{0.5}V_2O_5$," *Acta Crystallographica Section C: Crystal Structure Communications*, vol. 46, no. 9, pp. 1590–1592, 1990.

[159] A. Casalot, D. Lavaud, J. Galy, and P. Hagenmuller, "Les bronzes oxygénés de vanadium de formule $Cu_xV_2O_5$: Ii—mécanisme de conduction et degré d'oxydation du cuivre," *Journal of Solid State Chemistry*, vol. 2, no. 4, pp. 544–548, 1970.

[160] S. Anderson, "The crystal structure of a new silver vanadium oxide bronze, $Ag_{1-x}V_2O_5$ (x approximately 0.32)," *Acta Chem. Scand*, vol. 19, no. 6, 1965.

[161] H. Smolinski, C. Gros, W. Weber, U. Peuchert, G. Roth, M. Weiden, and C. Geibel, "NaV_2O_5 as a quarter-filled ladder compound," *Physical Review Letters*, vol. 80, no. 23, p. 5164, 1998.

[162] A. Damascelli, *Optical spectroscopy of quantum spin systems*. PhD thesis, University of Groningen, 1999.

[163] P. Thalmeier and P. Fulde, "Charge ordering and spin-Peierls transition in α-NaV$_2$O$_5$," *Europhysics Letters*, vol. 44, no. 2, p. 242, 1998.

[164] M. Mostovoy and D. Khomskii, "Charge ordering and opening of spin gap in NaV$_2$O$_5$," *Solid state communications*, vol. 113, no. 3, pp. 159–163, 1999.

[165] Z. Zheng, J. Chen, Y. Wang, X. Wang, X. Chen, P. Liu, J. Xu, W. Xie, H. Chen, S. Deng, *et al.*, "Highly confined and tunable hyperbolic phonon polaritons in van der Waals semiconducting transition metal oxides," *Advanced Materials*, vol. 30, no. 13, p. 1705318, 2018.

[166] R. G. Parr, "Density functional theory of atoms and molecules," in *Horizons of quantum chemistry*, pp. 5–15, Springer, 1980.

[167] E. K. Gross and R. M. Dreizler, *Density functional theory*, vol. 337. Springer Science & Business Media, 2013.

[168] S. Baroni, S. De Gironcoli, A. Dal Corso, and P. Giannozzi, "Phonons and related crystal properties from density-functional perturbation theory," *Reviews of Modern Physics*, vol. 73, no. 2, p. 515, 2001.

[169] J. P. Perdew, K. Burke, and M. Ernzerhof, "Generalized gradient approximation made simple," *Physical Review Letters*, vol. 77, no. 18, p. 3865, 1996.

[170] R. Cowley, "The lattice dynamics of an anharmonic crystal," *Advances in Physics*, vol. 12, no. 48, pp. 421–480, 1963.

[171] X. Ming, X.-L. Wang, J.-W. Yin, C.-Z. Wang, Z.-F. Huang, and G. Chen, "Electronic structure and magnetic coupling in CaV$_2$O$_5$: spin dimer versus spin ladder," *The European Physical Journal B*, vol. 75, no. 2, pp. 179–185, 2010.

[172] X. Sheng, Z. Li, and Y. Cheng, "Electronic and thermoelectric properties of V$_2$O$_5$, MgV$_2$O$_5$, and CaV$_2$O$_5$," *Coatings*, vol. 10, no. 5, 2020.

[173] P. Yeh, A. Yariv, and C.-S. Hong, "Electromagnetic propagation in periodic stratified media. i. general theory," *JOSA*, vol. 67, no. 4, pp. 423–438, 1977.

[174] P. Yeh, "Electromagnetic propagation in birefringent layered media," *JOSA*, vol. 69, no. 5, pp. 742–756, 1979.

[175] N. C. Passler and A. Paarmann, "Generalized 4× 4 matrix formalism for light propagation in anisotropic stratified media: study of surface phonon polaritons in polar dielectric heterostructures," *JOSA B*, vol. 34, no. 10, pp. 2128–2139, 2017.

[176] T. Zhan, X. Shi, Y. Dai, X. Liu, and J. Zi, "Transfer matrix method for optics in graphene layers," *Journal of Physics: Condensed Matter*, vol. 25, no. 21, p. 215301, 2013.

[177] Z. Popović, M. Konstantinović, R. Gajić, V. Popov, M. Isobe, Y. Ueda, and V. Moshchalkov, "Phonon dynamics in A-V$_2$O$_5$ (A= Na, Ca, Mg, Cs) oxides," *Physical Review B*, vol. 65, no. 18, p. 184303, 2002.

[178] G. Sai Gautam, P. Canepa, A. Abdellahi, A. Urban, R. Malik, and G. Ceder, "The intercalation phase diagram of Mg in V$_2$O$_5$ from first-principles," *Chemistry of Materials*, vol. 27, no. 10, pp. 3733–3742, 2015.

[179] A. D. Dunkelberger, C. T. Ellis, D. C. Ratchford, A. J. Giles, M. Kim, C. S. Kim, B. T. Spann, I. Vurgaftman, J. G. Tischler, J. P. Long, *et al.*, "Active tuning of surface phonon polariton resonances via carrier photoinjection," *Nature Photonics*, vol. 12, no. 1, pp. 50–56, 2018.

[180] W. Luo, M. Boselli, J.-M. Poumirol, I. Ardizzone, J. Teyssier, D. van Der Marel, S. Gariglio, J.-M. Triscone, and A. B. Kuzmenko, "High sensitivity variable-temperature infrared nanoscopy of conducting oxide interfaces," *Nature Communications*, vol. 10, no. 1, pp. 1–8, 2019.

[181] R. Cuscó, L. Artús, J. H. Edgar, S. Liu, G. Cassabois, and B. Gil, "Isotopic effects on phonon anharmonicity in layered van der Waals crystals: Isotopically pure hexagonal boron nitride," *Phys. Rev. B*, vol. 97, p. 155435, Apr 2018.

[182] J. Spitaler, E. Y. Sherman, and C. Ambrosch-Draxl, "Raman scattering of vanadium ladder compounds from first principles," *Physica Status Solidi (c)*, vol. 1, no. 11, pp. 3146–3149, 2004.

[183] H. U. Yang, E. Hebestreit, E. E. Josberger, and M. B. Raschke, "A cryogenic scattering-type scanning near-field optical microscope," *Review of Scientific Instruments*, vol. 84, no. 2, p. 023701, 2013.

[184] A. McLeod, E. Van Heumen, J. Ramirez, S. Wang, T. Saerbeck, S. Guenon, M. Goldflam, L. Anderegg, P. Kelly, A. Mueller, *et al.*, "Nanotextured phase coexistence in the correlated insulator V_2O_3," *Nature Physics*, vol. 13, no. 1, pp. 80–86, 2017.

[185] D. Lang, J. Döring, T. Nörenberg, Á. Butykai, I. Kézsmárki, H. Schneider, S. Winnerl, M. Helm, S. C. Kehr, and L. M. Eng, "Infrared nanoscopy down to liquid helium temperatures," *Review of Scientific Instruments*, vol. 89, no. 3, p. 033702, 2018.

[186] M. T. Dove and M. T. Dove, *Structure and dynamics: an atomic view of materials*, vol. 1. Oxford University Press, 2003.

[187] G. Ni, A. S. McLeod, Z. Sun, J. R. Matson, C. F. B. Lo, D. A. Rhodes, F. L. Ruta, S. L. Moore, R. A. Vitalone, R. Cusco, *et al.*, "Long-lived phonon polaritons in hyperbolic materials," *Nano Letters*, vol. 21, no. 13, pp. 5767–5773, 2021.